UNIVERSITÀ
DI TORINO

Doctoral School

PhD program in Molecular Medicine

XXXVI cycle

Standard therapy boosts glioblastoma stem-like cell resistance to apoptosis and confers sensitivity to BH3 mimetics

A dissertation submitted by

Marta Prelli

Supervised by

Professor Carla Boccaccio

2024

TABLE OF CONTENTS

ABSTRACT

Glioblastoma (GBM) is a lethal brain tumor that almost invariably recurs within 15 months after a standard treatment, which includes surgery, chemotherapy with temozolomide (TMZ), and radiotherapy (IR). GBM is thought to arise from stem-like cells (GSCs) that inherently resist therapies and can evolve under therapeutic pressure, ultimately driving tumor recurrence. Notably, in individual treatment-naïve GBMs, multiple GSC subpopulations can coexist, displaying different genetic and phenotypic profiles, potentially conferring varying levels of intrinsic treatment resistance. These traits may be selected or modulated by treatments, contributing to the therapeutic refractoriness observed in relapsing GBM. Investigating the mechanisms behind GSC resistance is essential to uncovering vulnerabilities that could be targeted in treating recurrences.

Due to the rarity of surgically removed recurrent GBMs and their limited availability for study, we developed an original *ex vivo* protocol to select GSCs that are resistant to conventional therapies, ideally representing the GSC subclones driving recurrence. Leveraging treatment-naïve GBMs removed with conventional or ultrasonic aspiration, we collected *bona fide* whole tumor cell populations. These were then subjected to chemo- or radio- therapies simulating patient treatment, while maintained in culture conditions that preserve GSC subclonal heterogeneity.

From each GBM, we established multiple long-term GSC-enriched cultures (neurospheres, NS), referred to as “res-GSC families”. Each family included at least one member selected by TMZ or IR (TMZ-NS and IR-NS respectively) alongside an untreated control (CTRL-NS).

Genetic and functional analysis revealed that resistant GSC family members exhibited properties mechanistically associated with the emergence of secondary therapeutic resistance. Secondary resistance to TMZ was linked to the onset of genetic alterations in mismatch repair genes such as MSH6 and MSH2, while secondary resistance to IR involved adaptive mechanisms sustaining DNA double-strand break repair by homologous recombination, including increased RAD51 expression. Overall, therapy-selected

GSCs displayed cytogenetic changes, increased stem cell frequency and tumor-initiating ability, and altered growth factor receptor expression, including increased EGFR and MET activity, two receptors known to support GSC survival and therapeutic resistance. Notably, secondary resistant GSCs exhibited an imbalance in BH3 family protein expression, favoring prosurvival proteins, partly driven by EGFR activity. Pharmacological inhibition of the prosurvival protein BCL-xL using BH3 mimetics restored this balance, effectively inducing apoptosis in resistant GSCs. This evidence paves the way for further investigations with a view toward clinical translation.

INTRODUCTION

Glioblastoma (GBM): definition and clinical challenges

Glioblastoma (GBM) is the most common malignant tumor of the central nervous system and, according to 2021 WHO Classification of Tumors of the Central Nervous, it is classified as a grade IV astrocytoma, characterized by absence of mutations in either IDH1 or IDH2 genes (IDH-wildtype) [1, 2]. Major GBM distinctive features are the presence of histologically defined areas of necrosis or microvascular proliferation, and genetic alterations such as TERT promoter mutation, EGFR amplification or combined gain of chromosome +7 and loss of chromosome 10 [1, 2].

Standard treatment for GBM, established in 2005, consists of maximal safe surgical resection, radiotherapy, and chemotherapy with a single agent, temozolomide (TMZ) [3]. Unfortunately, chemotherapy is ineffective in about half of patients due to the expression of the dealkylating enzyme Methylguanine-DNA methyltransferase (MGMT) in their tumors [2]. MGMT effectively repairs the DNA-adduct O(6)methylguanine (O(6)MeG), induced by TMZ, thereby preventing cytotoxicity and ultimately apoptosis of GBM cells [4]. In normal tissues, MGMT is broadly expressed, counteracting TMZ effects in non-tumoral cells and rendering TMZ a relatively safe drug. Conversely, in a fraction of GBMs MGMT is not expressed, mainly due to the methylation of its promoter, rendering them sensitive to TMZ [5, 6].

GBM almost invariably relapses (median progression free survival <10 months), rapidly leading to death (median overall survival <15 months, 5-year survival rate <5%) and thus remaining one of the deadliest of all tumors [7, 8]. Multiple factors contribute to treatment failure and hinder therapeutic progress. These include topological challenges, such as the locally infiltrative nature of the tumor and its proximity with vital areas, which prevent complete surgical resection and exhaustive irradiation. Additionally, the presence of the blood-brain barrier (BBB) limits drug penetration. Immunotherapeutic strategies have also lagged behind, as the GBM microenvironment is poorly accessible to adaptive immunity [9, 10].

Despite extensive characterization of GBM genetic, epigenetic and biological features, efforts to identify and assess innovative therapeutic strategies targeting frequently altered signaling pathways - such as PIK3K/Akt/mTOR, EGFR and retinoblastoma (Rb) pathways - have been disappointing [11-15].

GBM heterogeneity: a major obstacle to therapeutic progress

A critical challenge for conventional target identification in GBM is its remarkable genetic and functional heterogeneity, both intertumoral and intratumoral.

Intertumoral heterogeneity has been observed at both genetic and epigenetic level. Different GBMs harbor distinct genetic alterations converging on the MAPK/PIK3K pathway (PIK3CA, PIK3R1, PTEN, EGFR, PDGFRA and NF1), the Rb tumor-suppressive pathway (CDK4, CDK6, CDKN2A/B and RB1), and the p53 axis (MDM2, MDM4 and TP53) [16, 17]. In addition, GBMs can also be classified according to their DNA methylation profiles [18-20]. Intertumoral heterogeneity is further reflected at transcriptional level, where GBM are classified into three subtypes: classical, proneural and mesenchymal, which display preferential expression of different Receptor Tyrosine Kinases (RTKs) and are associated respectively with EGFR, PDGFRA and NF1 genetic alterations [16, 21].

Regarding GBM intratumoral genetic heterogeneity, i.e., the co-existence of multiple, genetically distinct but phylogenetically related subclones, it is known that cells with heterogeneous gene copy number variations, or with mutually exclusive amplification of different Receptor Tyrosine Kinases (RTKs), can coexist in the same tumor [22-24]. Single-cell studies have also demonstrated that intratumoral heterogeneity occurs at transcriptional level, indicating that GBM cells reside on continuous cellular states mostly linked to neurodevelopmental cell types (NPC-like, OPC-like, AC-like, and MES-like) [25, 26], but they can also be subdivided into metabolic subtypes according to their mitochondrial dependency [27]. Additionally, GBMs exhibit intratumoral heterogeneity in MGMT promoter methylation [28], and in the genetic alterations of DNA damage repair-associated genes [29], leading to a varying degree of sensitivity to the conventional therapies [30, 31], which in turn fosters therapeutic resistance.

The heterogeneous composition of individual GBMs lays the foundation for primary resistance to targeted treatments, i.e., the upfront resistance manifested by cells that do not harbor the drug target. Furthermore, this heterogeneity sets the stage for genetic evolution from primary to recurrent GBM, resulting in the positive selection of pre-existing (minor) resistant subclones or the emergence of resistant cell populations characterized by novel genetic alterations or adaptive features induced by genotoxic therapies (secondary resistance) [32-39].

GBM stem-like cells (GSCs): tumorigenicity and therapeutic resistance

A promising avenue for identifying a GBM Achilles' heel in both primary and recurrent tumors emerged from research on GBM cancer stem cells (GSCs), a subpopulation with tumor-initiating ability that is believed to sit at the apex of the GBM cell hierarchy [40, 41]. Although GSCs were recognized two decades ago [42, 43], the identity of their putative cell of origin, and thus the source of GBM itself, remains debated. Studies in human patients and engineered mouse models suggest neural stem cells (NSCs) as the most likely GBM cell of origin [44, 45]. However, experimental models indicate that also astrocyte and oligodendrocyte progenitors cells (OPCs), and even differentiated neurons, can transform into GSCs [46-50].

In GBM, as well as in leukemia and solid tumors, the presence of cancer stem cells has been identified and quantified through the use of functional assays. The gold-standard test is the clonogenic limiting-dilution assay (LDA), performed *in vitro* and *in vivo* through serial transplantation [51]. Long-term propagating cultures known as neurospheres, which can be derived with high efficiency from each patient's GBM, are highly enriched in cells that retain both functional stem cell properties *in vitro* and *in vivo*, and the genetic and molecular features of the original tumor, making them reliable GSC models

[43, 52, 53]. In addition, GSCs can be prospectively isolated from original tumors with surface markers such as CD133 [54], CD15 [55], CD44 [56] and CD49f [57]. However, the significant inter -sample variability of these markers has limited their use for consistently enriching GSCs from GBM tissues [51]. Notably, alongside their long-term self-renewal capabilities, GSCs have been shown to harbor molecular determinants of inherent resistance to genotoxic treatments compared to non-stem GBM cells, including constitutively prompted DNA repair mechanisms [35, 58], which can, in turn, be modulated by EGFR [59] and MET [60]. In addition, GSCs can enter a quiescent or slow-cycling state, providing a mechanism to evade therapies that target rapidly dividing cells [61]. Altogether, resistance to genotoxic treatments and the ability to enter a quiescent state enable GSCs to endure therapeutic pressures and emerge as a resistant population, contributing to tumor recurrence [35, 58, 61].

GSCs: heterogeneity and plasticity

The GSC concept is constantly refined, leading to the recent definition of GSCs as “cells endowed with long-term self-renewal that can produce a progeny with a variety of cells states” [51], referring to progeny cells that exhibit varying degrees of self-renewal capability, pseudo-differentiative potential, and interchangeable transcriptional phenotypes. Converging evidence suggests that stemness is not a fixed but rather a plastic state, allowing GBM cells to shift between stem-like and more differentiated states. The notion of hierarchical plasticity of GSCs is challenging to prove in experimental models but is convincingly supported by the evidence that GBM epigenetic and transcriptional plasticity occurs at single-cell level. Such evidence has been provided by different research groups each generating unique yet largely consistent classification systems. According to these systems, GBM cells can exist: i) in four main interconnected cellular states reminiscent of neurodevelopment (oligodendrocyte-progenitor-like or OPC-like, neural-progenitor-like or NPC-like, astrocyte-like or AC-like, and mesenchymal-like or MES-like state [26, 62]; ii) along a single axis of transcriptional variation spanning proneural and mesenchymal states [63]; iii) along a single axis referred to as neurodevelopment-injury response [64]; and iv) within an axis including progenitors and pseudodifferentiated glial, neuronal and mesenchymal cell types [65].

Notably, GSC plasticity has been recognized as crucial for therapeutic resistance and GBM recurrence, as it enables the modulation of the transcriptional and metabolic profiles efficiently and flexibly in response to therapy [66] and creates a range of cellular states with varying sensitivity to treatments. In this context, a subpopulation of cells known as drug-tolerant persisters can survive treatment through plastic and reversible phenotypic changes, which can either revert upon a "drug holiday" period or can be fixed and become permanent, resulting in drug resistant cells [67, 68].

GSC plasticity does not undermine the notion that the dangerous 'stem state' relies on molecular features that could be profitably targeted; rather, it emphasizes that GSCs are not only a relatively tiny, but also a mobile target. However, despite this plasticity, the number of cellular states encoded by the GSC epigenetic landscape remains relatively limited, paving the way to a therapeutic approach aimed at "State Selective Lethality" [69].

Isolation of heterogeneous GSCs

In this challenging scenario, consensus holds that cellular and mouse models representing GBM intratumoral complexity are essential for the functional validation of therapeutic targets [51, 70]. However, the most refined available models - based on genetically engineered mice, patient-derived xenografts or long-term propagating GSC cultures (neurospheres, NS) - often capture only fragments of the overall tumor architecture and rarely represent the entire cell population subjected to therapeutic pressures [41, 71]. NS, in particular, are usually derived from surgical samples of limited size, which seldom represent the whole tumor's variegated landscape. Previous analyses performed in our lab on more than 100 NS, conventionally derived from as many tumors, indicate that, although NS generally capture intertumoral genetic heterogeneity, each NS culture is often monophyletic [72]. Accordingly, each NS harbors, in a mutually exclusive fashion, some driving genetic lesions, such as EGFR^{amp} or PTEN^{loss}, which coexist in tissues [72]. Despite limitations, isolating GSCs as 'neurospheres' remains the most reliable methodology to obtain long-term self-propagating cell clones that faithfully retain the genetic-make up of tumor (sub)clones, with clear advantages over genetically-drifted conventional cell lines [71]. Moreover, genetically and functionally distinct GSCs can be derived from different areas of the same tumor [73].

To address limitations of deriving NS from GBM tissue fragments, our lab recently developed a protocol based on the recovery of the entire GBM mass removed by ultrasonic aspiration [74, 75]. Starting from this material, we derived NS by applying in parallel different selective culture media represented by various growth factor cocktails. These factors (EGF, FGF2, PDGF and HGF) were chosen for being highly expressed in normal brain and even more so in the GBM microenvironment, and for being able to activate RTKs that are often heterogeneously expressed and amplified in GBM. The growth factors were supplied alone, or combined as in the standard GSC standard medium (EGF and FGF2 at 20 ng/mL each: EF), or all together, at a standard concentration (20 ng/mL each: EFPH20) or at a lower concentration (2 ng/mL each: EFPH2).

This approach allowed us to isolate distinct GSC populations (NS) representative of different subclones coexisting in the same tumor, revealing genetic and phenotypic differences among GSCs, and reconstructing their genealogical relationship [74]. Notably, GSCs could segregate different RTKs amplifications across both chromosomal and extrachromosomal DNA, offering insights into intratumoral heterogeneity arising from non-Mendelian segregation of gene amplifications and its associated plasticity. Additionally, the richest growth factor medium (EFPH20) yielded NS cultures at frequencies comparable to the standard GSC medium while also supporting the concurrent activation of multiple

RTKs, thereby promoting the activation of multiple survival pathways involved in therapeutic resistance [74].

GBM longitudinal evolution and recurrence

Given that GBM patients often succumb to increasingly resistant tumor recurrences post-treatment, recent efforts have focused on investigating the tumor evolution from primary to recurrent stages. Initial genomic studies revealed that recurrent tumors frequently bear the hallmarks of the temozolomide mutagenic effect, such an enrichment in C>T transitions, associated with MMR gene mutations and hypermutation [33, 76]. GBM evolves through both linear and branched genetic pathways, with primary tumor subclones often emerging at recurrence [32, 33, 37, 76]. Recurrent GBMs also frequently switch toward a mesenchymal transcriptional subtype [33].

The Glioma Longitudinal Analysis Consortium (GLASS) was recently established, aiming to systematically collect matched primary and recurrent specimens from over a thousand glioma patients [77]. A landmark study from GLASS have validated the emergence of a hypermutator phenotype following temozolomide therapy, tied to MMR loss, and showed that key GBM driver mutations identified at the initial diagnosis - such as IDH1, TP53, TERT promoter, and EGFR alterations - are often preserved in recurrences, highlighting their role in sustaining tumor growth [36]. This study noted that despite a general rise in aneuploidy, GBM clonal architecture tends to remain stable over time. Therapeutic pressures including both temozolomide and irradiation do not strongly preferentially select for specific mutations, making recurrence-associated subclone emergence largely stochastic [36].

Further studies from GLASS and other groups emphasized phenotypic shifts in recurrent GBMs, notably in response to microenvironmental interactions [78, 79]. These shifts include upregulation of neuronal signaling, potentially driven by interaction with neurons, and a mesenchymal transcriptional profile likely promoted by tumor-associated myeloid cells [78, 79]. Single-cell analyses of recurrent tumors have corroborated the mesenchymal shift and identified AP1 transcription as central to sustaining this phenotype [80]. The importance of AP1-driven programs has been underscored by an ample study aiming at characterizing GBM heterogeneity and evolution in a 3D whole tumor perspective [81]. In this study, a detailed map of complex spatial variations in the tumor microenvironment, subclonal composition and distribution of RTK amplification and driver gene deletions has been provided [81]. Finally, proteogenomic studies have begun to unravel the importance of specific signaling pathways such as Wnt, BRAF and PTPN1 in supporting features characteristic of recurrent GBMs [82, 83].

Together, these extensive longitudinal analyses of tumor tissues have highlighted the complexity and heterogeneity of recurrent GBMs while pointing toward microenvironmental interactions, transcriptional adaptation and cell signaling as potential therapeutic vulnerabilities.

Models of recurrent GSCs

Longitudinal multi-omic analyses of archival GBM tissues collected over past decades have provided invaluable insight into mechanisms driving GBM evolution under therapeutic pressure. However, experimental models of recurrent GBMs based on GSCs, which are amenable to manipulation for validating findings from fixed tissues and preclinical testing of novel therapeutic strategies, remain limited. The most promising model should encompass collections of GSCs derived from matched primary, treatment-naïve and recurrent GBMs. Our group previously characterized five neurosphere pairs derived from matched primary and recurrent GBMs, observing genetic evolution in MGMT-deficient, temozolomide-sensitive neurospheres. In these cases, consistent with longitudinal GBM tissue studies, neurospheres exhibited linear or branched genetic evolution, emergence of minor primary tumor subclones, temozolomide-associated mutations and hypermutation linked to MMR gene mutations [34]. However, prospectively isolating neurospheres from primary and recurrent GBM pairs is challenging to scale-up, as recurrent GBMs rarely undergo surgical resection.

Alternatively, an initial attempt to model *in vitro* GBM evolution under conventional treatment was performed using established cultures from primary GBMs [84]. This protocol involved treatment with clinically relevant doses of TMZ and radiations followed by phenotype evaluation shortly (one week) post-treatment. This short-term evaluation was insufficient to observe the biological effects and genetic adaptations that drive resistance, leaving critical questions unanswered. Additionally, established GBM cultures may lack the intratumoral heterogeneity of the original tumor, biasing therapeutic selection. Thus, innovative recurrent GSC models that capture both intrinsic and acquired therapeutic resistance are urgently needed to improve functional assessment of novel therapeutic targets.

AIM OF THE WORK

The aim of this PhD project was to identify genetic and molecular features associated with GSCs from recurrent tumors and their therapeutic resistance, with the ultimate goal of leveraging these features for therapeutic targeting in preclinical intervention and prevention trials.

A crucial step for this project was to develop a preclinical model of recurrent GSCs suitable for experimental manipulation. To this end, we designed an *ex vivo* treatment protocol allowing for a rigorous comparison between human GSCs emerging after therapeutic pressures and those from the original tumors.

RESULTS

GSCs coexisting in single GBMs display different sensitivity to conventional therapies

We previously showed that individual GBMs contain genetically and phenotypically heterogeneous glioblastoma stem-like cells (GSCs), which can be propagated in culture as neurospheres (NS) [74, 75]. In this study, we investigated whether distinct GSCs coexisting in the same tumor exhibit varying sensitivity to conventional therapies, potentially leading to differential selection by treatment.

To this end, we evaluated the response to standard therapeutic treatments of a representative "GSC family", GBM17, described in our recent study ([74]; see Introduction). Briefly, this GSC family includes five neurospheres that were derived from a single GBM, by subjecting the entire cell population (surgically removed with an ultrasonic aspirator) to parallel selective culture media containing different growth factors or growth factor combinations. The GBM17 GSC family encompasses five members, each named after the growth factor(s) in which it was selected (E: EGF, F: FGF, EF: EGF and FGF, EFPH20: EGF, FGF, PDGF and HGF at high concentration; and EFPH2: EGF, FGF, PDGF and HGF at low concentration). This GSC family is characterized by genetic and phenotypic heterogeneity, represented by differences in MYC amplification and transcriptional profiles (according to Wang et al. [21]) (Figure 1A). All five members displayed MGMT promoter methylation and did not express MGMT protein. Consistently, they were all sensitive to temozolomide (TMZ) treatment in dose-response experiments, using clinically relevant doses [85] and measuring cell viability 9 days after treatment (Figure 1B). However, at the highest dose of 50 µM, EFPH20 and EFPH2 retained a degree of resistance, while E, F and EF were mostly vulnerable (Figure 1B). The varying TMZ resistance among GSC family members was paralleled by different sensitivity to clinically relevant doses of ionizing radiation (IR, Figure 1C) [3]. Thus, although GBM17 could generally be classified as a chemosensitive and radioresistant tumor (as most GSCs displayed a surviving fraction >0.5), it comprised GSCs displaying heterogeneous therapeutic responses, which could lead to differential selection by therapies and confer different potential to drive tumor recurrence.

Interestingly, we observed that the EFPH20 member, selected by the richest growth factor cocktail, and characterized by a mesenchymal profile featuring high levels of receptor tyrosine-kinase (RTK) expression, displayed the highest resistance to both TMZ and IR (Figures 1B and 1C). This supports the hypothesis that activation of the main survival pathways via increased RTK expression and activity, which was also observed in all EFPH20 members of previously characterized GSC families [74], could sustain mechanism(s) of resistance to therapies.

Generation of models representing matched GSCs from *de novo* and recurrent GBMs

Based on the above observations, we developed a protocol to *ex-vivo* select GSCs representing those that emerge after *in vivo* treatment and drive tumor recurrence (Figure 1D). To this end, we obtained whole GBM cell populations, surgically removed by using a dedicated aspirator (ultrasonic or conventional). After processing into single-cell suspensions, GBMs were placed in the GSC selection medium named EFPH20, containing EGF, FGF2, PDGF and HGF at 20 ng/mL [74, 75]. After a short recovery period, single-cell cultures derived from single GBMs were treated in parallel with selective therapeutic pressures, using TMZ at 50 μM every three days for three times, or IR at a 2 Gy dose for five consecutive days. A third culture remained untreated in order to represent treatment-naïve GSCs (Figure 1D).

Treatments doses and schedules used can be considered as clinically relevant, because: i) they mimic those administered to patients [3, 85] , and ii) they were able to distinguish *in vitro* between inherently resistant (primary resistant) and sensitive GSCs, as measured in an independent panel of previously derived GSC cultures (grown as NS) in dose-dependent and time-course experiments (Figure 1E and 1F). During the derivation phase, the treatment effects on cells in culture could be appreciated by microscopy, with cells sensitive to the therapeutic agent (either TMZ or IR) decreasing in number and displaying apoptotic features, while untreated cells appeared healthy (Figures 1G and 1H).

Cells (ideally GSCs) surviving these treatments gave rise to long-term propagating NS. From each GBM, we defined the ensemble of established NS cultures including at least one culture selected by therapy as a “res-GSC family”, and each NS culture as a “res-GSC family member”. Specifically, NS cultures were named as CTRL-NS (those treatment-naïve), TMZ-NS (those emerging after TMZ treatment), or IR-NS (those emerging after IR treatment). In addition, blood and GBM tissue samples from patient, and fresh DNA and RNA from the processed whole GBM cell population were collected for further comparative analysis (Figure 1D).

In summary, we established an innovative protocol that allows to generate *ex vivo* models of GSCs resistant to standard treatments. The protocol relies on the concomitant application of the following factors to GBM whole cell populations: (i) clinically relevant therapeutic pressures; (ii) culture conditions selecting for GSCs; and (iii) a brain-mimicking culture environment enriched in growth factors, fostering cell survival. These models represent recurrent (TMZ-NS and/or IR-NS) GSCs matched with treatment-naïve (primary) GSCs (CTRL-NS).

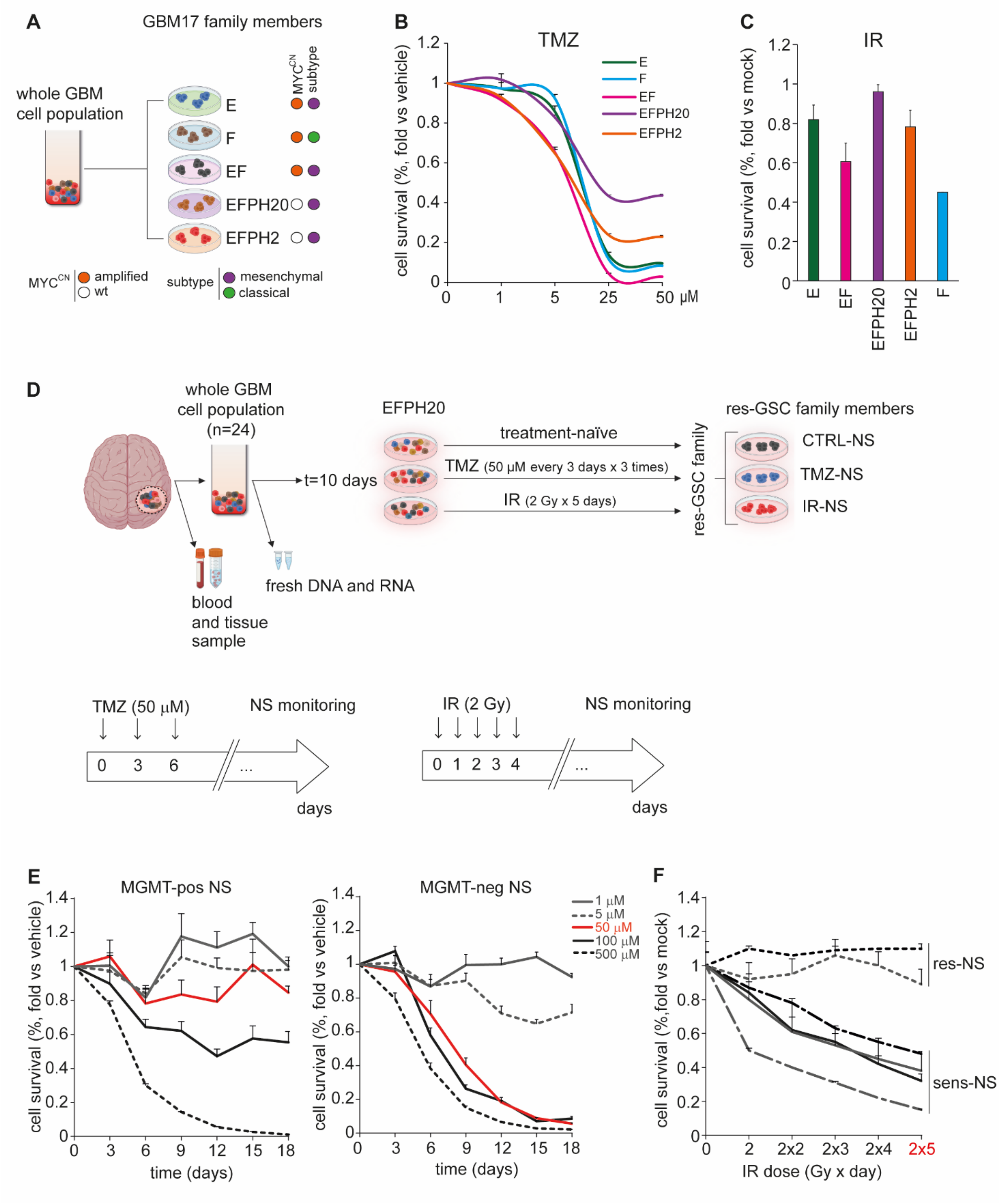
A
GBM17 family members
whole GBM cell population
MYC^CN
subtype
E
F
EF
EFPH20
EFPH2
MYC^CN amplified
wt
subtype mesenchymal
classical
B
TMZ
cell survival (%, fold vs vehicle)
1.2
1
0.8
0.6
0.4
0.2
0
0 1 5 25 50 μM
E
F
EF
EFPH20
EFPH2
C
IR
cell survival (%, fold vs mock)
1.2
1
0.8
0.6
0.4
0.2
0
E
EF
EFPH20
EFPH2
F
D
whole GBM cell population (n=24)
t=10 days
blood and tissue sample
fresh DNA and RNA
EFPH20
treatment-naïve
TMZ (50 μM every 3 days x 3 times)
IR (2 Gy x 5 days)
res-GSC family
res-GSC family members
CTRL-NS
TMZ-NS
IR-NS
TMZ (50 μM)
0 3 6 ...
NS monitoring
days
IR (2 Gy)
0 1 2 3 4 ...
NS monitoring
days
E
MGMT-pos NS
cell survival (%, fold vs vehicle)
1.4
1.2
1
0.8
0.6
0.4
0.2
0
0 3 6 9 12 15 18
time (days)
MGMT-neg NS
cell survival (%, fold vs vehicle)
1 μM
5 μM
50 μM
100 μM
500 μM
0 3 6 9 12 15 18
time (days)
F
cell survival (%,fold vs mock)
1.4
1.2
1
0.8
0.6
0.4
0.2
0
0 2 2x2 2x3 2x4 2x5
IR dose (Gy x day)
res-NS
sens-NS

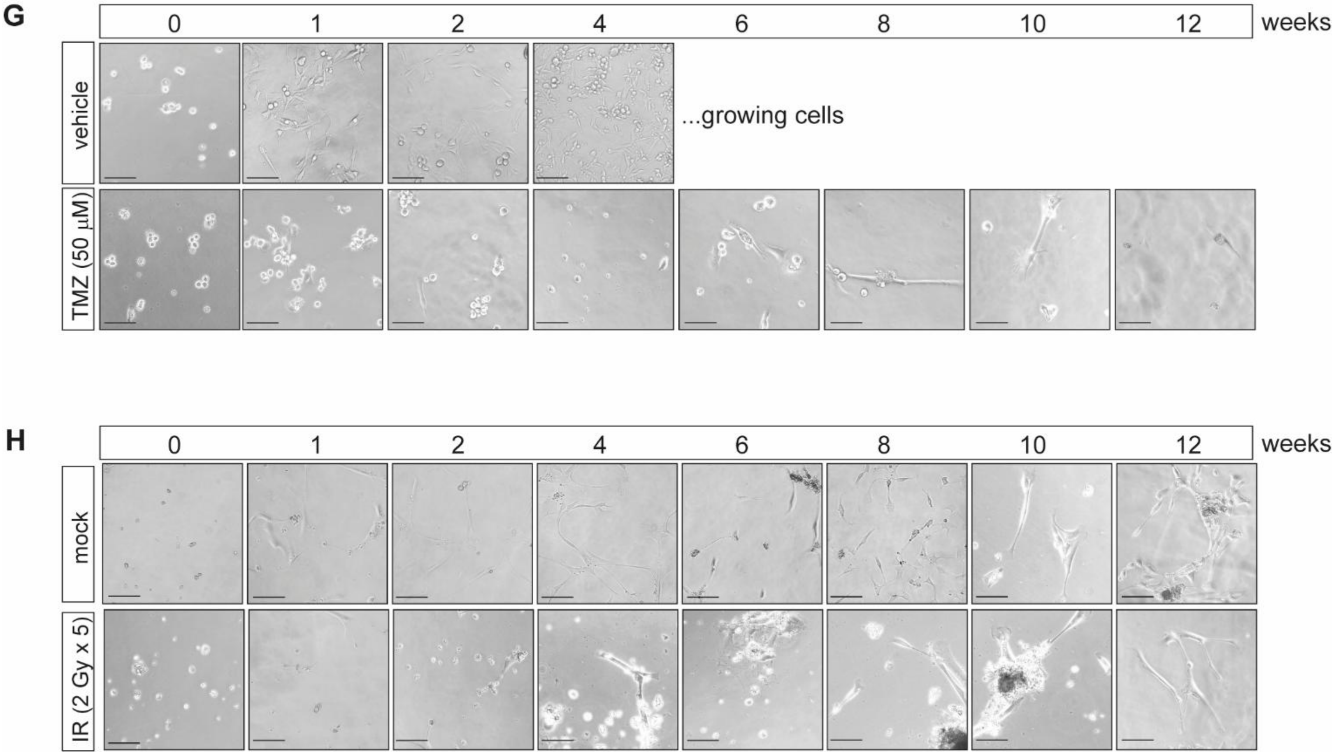

Figure 1. Generation of models representing matched GSCs from *de novo* and recurrent GBMs

(A) Schematic representation of GBM17 GSC family. MYC copy number was evaluated by Real Time PCR. GBM subtype classification was performed according to Wang.et al. [21]. Scheme created with BioRender.com
(B) Cell survival (fold vs. vehicle) of the indicated members of GBM17 family, measured 9 days after the beginning of the treatment with increasing doses of temozolomide (TMZ, 1-50 µM). Data are shown as mean ± SEM of a representative experiment. Vehicle: cells treated with DMSO.
(C) Cell survival (fold vs. mock) of the indicated GBM17 family members, measured 48 h after the last treatment with ionizing radiations (IR, 2 Gy x 3 days) Data are shown as mean ± SEM of a representative experiment. Mock: no IR.
(D) *Ex-vivo* treatment of whole GBM cell populations with chemo or radiotherapy and generation of res-GSC families.
Top panel: Res-GSC families (n=8) are selected from whole GBM cell suspensions, by supplying a medium supplemented with EGF, FGF, PDGF and HGF 20 ng/mL and applying therapeutic pressures (TMZ or IR). Cultured enriched in GBM stem cells (defined as neurospheres, NS) that manage to reach passage 10 are considered established.
Bottom panel: detailed *ex vivo* temozolomide and irradiation treatment schedule in res-GSC families derivation protocol.
(E) Time course and dose response to TMZ measured as cell survival (fold vs. vehicle) in MGMT-pos (left panel) and MGMT-neg (right panel) representative NS. Data are shown as mean ± SEM of a representative experiment. Vehicle: cells treated with DMSO.
(F) Time course and dose response to IR measured as cell survival (fold vs. mock) in representative NS. Data are shown as mean ± SEM of a representative experiment. Mock: no IR.
(G) Cell morphology of a representative MGMT-neg GBM population *treated ex-vivo* with temozolomide at 50 µM or vehicle. Scale bar, 100 µm.
(H) Cell morphology of a representative radiosensitive GBM population treated *ex-vivo* with IR 2 Gy for 5 consecutive days or mock. Scale bar, 100 µm

Generation of res-GSC families correlates with specific patients’ genetic features and poor overall survival

The *ex vivo* derivation protocol was applied to 24 GBMs, i.e. grade 4 gliomas with IDH1/2 wild-type genes, as defined by histopathological diagnosis according to WHO 2021 CNS tumor classification (Table 1;[1]). Eight res-GSC families were derived , six of which included all three members, and two included only CTRL- and TMZ or IR-NS (Figure 2A and Table 1). Regarding the remaining 16 GBMs, in 2 cases (GBM112 and GBM144) only the CTRL-NS was established, while in 14 cases no NS could be derived (Figure 2A and Table 1). Considering all the cases (n=10) where at least the CTRL-NS was established, we were able to generate neurospheres with a derivation efficiency of 42%, which was lower than that observed in analogue culture conditions in a former study [74] (derivation efficiency of 61 %). This discrepancy could be explained by the fact that, in the previous study, almost all GBMs were surgically removed using an ultrasonic aspirator, whereas, in the generation of res-GSC families, several GBMs were removed with a conventional (not ultrasonic) aspirator potentially impairing cell viability, and, consequently, the neurosphere derivation.

By the analysis of the original GBM tumors (i.e. in samples of the whole GBM populations) we found that MGMT promoter methylation, a prognostic factor for GBM patients’ response to TMZ, was detectable in 42% of cases (Figure 2B), without correlation with the possibility to derive res-GSC families (Fisher’s exact test, p=0.65).

NGS analysis of the original GBM tumors (again performed on samples of the whole GBM populations), executed through a targeted panel exploring 75 GBM driver genes, and genes involved in DNA damage repair, hence defined GBM-target panel, confirmed lack of IDH1/2 gene alterations (Figure 2B). Consistent with TCGA data, TERT promoter mutations were very frequent (88%) (Figure 2B). Given its prevalence, we also used TERT variant allele frequency (VAF, shown in Table 2) to estimate the fraction of GBM cells in the original cell suspension, observing a wide range of tumor cell content (0.12 to

32.44%, Table 2). However, we ruled out any correlation between a high percentage of GBM cells in the original sample (>10%) and the possibility to derive res-GSC families (Fisher's exact test, p=0.39).

In our cohort, the frequencies of other driver gene alterations were comparable to those reported by TCGA [17] and the GLASS consortium [36], except for CDKN2A-B deletion (Figure 2B), whose underrepresentation could be caused by the low percentage of GBM cells in the original samples, limiting the evaluation of gene copy loss (as previously reported in [74]) (Figure 2B and Table 2). Altogether, the result of genetic analysis supported the representativeness of the collected GBM cohort, reinforcing the relevance of data described in this study.

We evaluated the possible correlation between genetic alterations in the original GBMs and the probability to generate res-GSC families, observing that GBMs harboring TP53 mutations had a significantly increased probability to do so (Fisher exact test, p=0.001) (Figure 2C), as previously reported in the generation of GSC families without therapeutic pressure but in the presence of different growth factor cocktails [74]. *Vice versa*, the presence of EGFR alterations tended to be anti-correlated with res-GSC families derivation, again consistently with the above study [74] and with previous evidence that high EGF concentration in the GSC selection medium counterselects EGFR amplification [86]. These data suggest that TP53 alterations and EGFR amplification respectively favor or counteract GSC derivation *per se*, rather than GSC derivation under therapeutic pressure.

In addition, GBMs yielding res-GSC families showed a tendency (p=0.06) to correlate with an increase in PTEN loss (i.e. biallelic inactivation). This alteration has not been correlated with GSC derivation *per se*, i.e., in the absence of therapeutic pressures, in our previous study [74]. Given the PTEN role in promoting cell apoptosis when proficient, its inactivation could be relevant in sustaining cells survival under therapeutic treatment, thus favoring derivation of res-GSC families [87-90].

No other genetic alterations, including those affecting DNA repair pathways (p=0.62), were significantly correlated to the generation of res-GSC families; however, considering the low number of samples recruited in the cohort and the low percentage of GBM cells in the cell-suspension, we cannot exclude that other subclonal alterations below NGS sensitivity were present and significant in promoting res-GSC derivation.

Interestingly, by investigating correlations between patients' clinical features and res-GSC family generation (Table 1 and Figure 2D), we observed that patients from whom res-GSC families were derived displayed a significantly decreased overall survival (OS) as compared to patients from whom res-GSC families could not be derived (Figure 2D and E). This observation supports the hypothesis that patients with poorer prognosis harbor GSCs subpopulations amenable to *in vitro* isolation and intrinsically resistant to standard treatments. On the contrary, patients with a better outcome could harbor GSCs less amenable to *in vitro* derivation, either in the presence or in the absence of a therapeutic pressure. A deeper characterization of the molecular features of the original GBM tissues could allow to develop new selection protocols (e.g. new growth factor combinations) able to favor GSC selection from these more favorable cases as well.

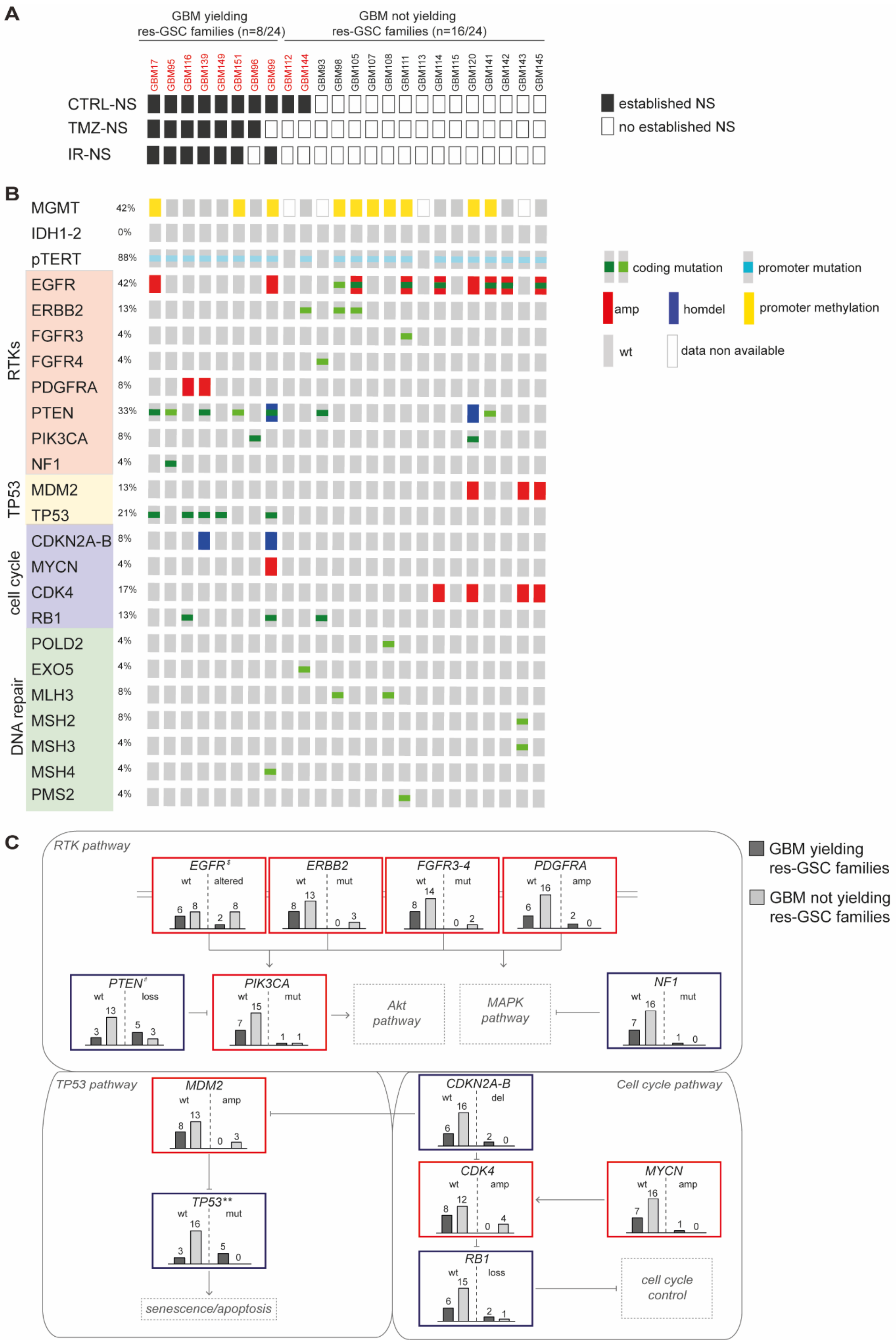
A
GBM yielding res-GSC families (n=8/24)
GBM not yielding res-GSC families (n=16/24)
GBM17 GBM95 GBM116 GBM139 GBM149 GBM151 GBM96 GBM99 GBM112 GBM144 GBM93 GBM98 GBM105 GBM107 GBM108 GBM111 GBM113 GBM114 GBM115 GBM120 GBM141 GBM142 GBM143 GBM145
CTRL-NS
TMZ-NS
IR-NS
established NS
no established NS
B
MGMT 42%
IDH1-2 0%
pTERT 88%
RTKs
EGFR 42%
ERBB2 13%
FGFR3 4%
FGFR4 4%
PDGFRA 8%
PTEN 33%
PIK3CA 8%
NF1 4%
TP53
MDM2 13%
TP53 21%
cell cycle
CDKN2A-B 8%
MYCN 4%
CDK4 17%
RB1 13%
DNA repair
POLD2 4%
EXO5 4%
MLH3 8%
MSH2 8%
MSH3 4%
MSH4 4%
PMS2 4%
coding mutation
promoter mutation
amp
homdel
promoter methylation
wt
data non available
C
RTK pathway
EGFR$ wt altered 6 8 2 8
ERBB2 wt mut 8 13 0 3
FGFR3-4 wt mut 8 14 0 2
PDGFRA wt amp 6 16 2 0
PTEN# wt loss 3 13 5 3
PIK3CA wt mut 7 15 1 1
Akt pathway
MAPK pathway
NF1 wt mut 7 16 1 0
TP53 pathway
MDM2 wt amp 8 13 0 3
TP53** wt mut 3 16 5 0
senescence/apoptosis
Cell cycle pathway
CDKN2A-B wt del 6 16 2 0
CDK4 wt amp 8 12 0 4
MYCN wt amp 7 16 1 0
RB1 wt loss 6 15 2 1
cell cycle control
GBM yielding res-GSC families
GBM not yielding res-GSC families

D

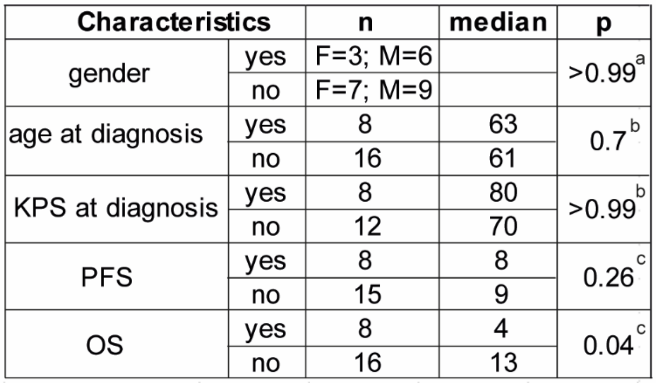

Characteristics		n	median	p
gender	yes	F=3; M=6		>0.99[a]
	no	F=7; M=9		
age at diagnosis	yes	8	63	0.7[b]
	no	16	61	
KPS at diagnosis	yes	8	80	>0.99[b]
	no	12	70	
PFS	yes	8	8	0.26[c]
	no	15	9	
OS	yes	8	4	0.04[c]
	no	16	13	

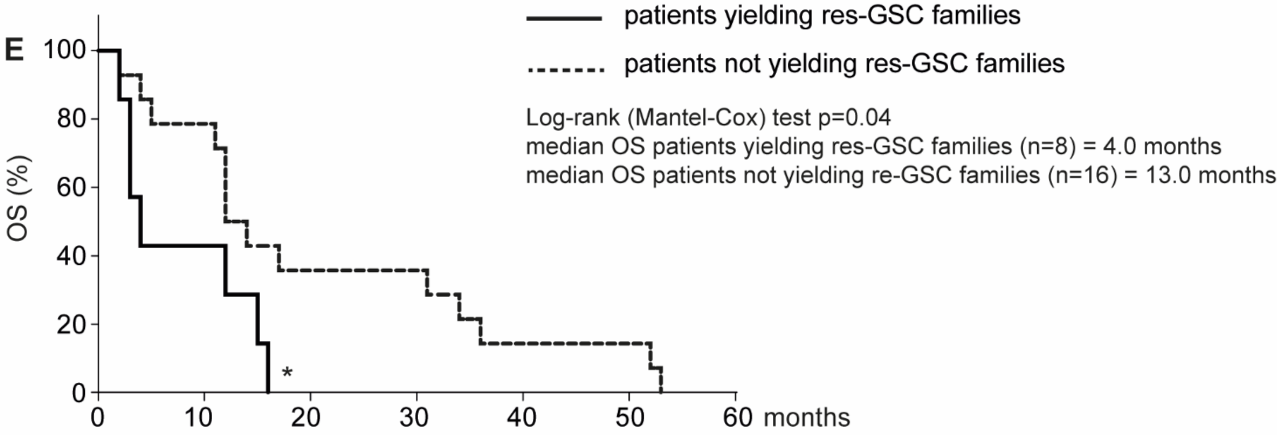

Figure 2. Generation of res-GSC families correlates with specific patients' genetic features and poor overall survival

(A) Res-GSC families derivation from whole GBM cell populations (n=24). Rows: res-GBM families members derived in each family. Columns: processed GBM grouped by the capacity to yield res-GSC families (n=8) or not (n=16).

(B) Genetic alteration frequencies in the res-GSC families cohort. GBMs are ordered as in (A). Genetic alterations were evaluated by a target NGS panel except for pTERT mutation, evaluated by ddPCR. MGMT promoter methylation was evaluated by ddPCR.

(C) Correlations between the genetic alterations of original GBMs and the generation of res-GSC families. Bars indicate the number of GBMs, either wild-type or alternated in each gene that yielded res-GSC families (dark grey bars) or not (light grey bars). $Tendency to anti-correlation between EGFR alterations and res-GSC families generation (p=0.39); #tendency to correlation between PTEN loss and res-GSC families generation (p=0.06); **correlation between TP53 mutations and res-GSC families generation (p=0.001) (Fisher's exact test).

(D) Correlations between patient clinical features and generation of res-GSC families. For each feature, patients are grouped according to their ability to generate res-GSC families (yes) or not (no). Statistical significance of gender was evaluated using [a] Fisher's exact test; [b] Student's t test; [c] Long-rank Mantel-Cox test. OS: overall survival. PSF: progression- free survival.

(E) Overall survival (OS) curves of patients yielding res-GSC families (n=8) or not (n=16), showing a significant decrease in OS in patients yielding res-GSC families (p=0.04) as evaluated by Log-rank Mantel-Cox test.

Table 1. clinical characteristics of GBM patients

SAMPLE ID	res-GSC family*	CLINICAL DATA						
		GENDER	AGE	LOCALIZATION	KPS	TREATMENT	PFS	OS
GBM17	yes	F	62	Temporal right	90	exeresis + RT + CT	4	12
GBM93	no	M	34	Parietal right	90	exeresis + RT + CT	4	12
GBM95	yes	M	63	Tempo-parietal right	40	exeresis	0	3
GBM96	yes	M	74	Parieto-occipital right	80	exeresis + RT + CT	8	15
GBM98	no	F	81	Frontal right	80	exeresis + RT + CT	43	52
GBM99	yes	M	65	Parieto-occipital right	80	exeresis + RT + CT	9	living
GBM105	no	F	52	Parieto-occipital right	80	exeresis + RT + CT	30	36
GBM107	no	F	72	Temporal left	<50	exeresis	0	2
GBM108	no	M	59	Parietal right	50	exeresis	1	4
GBM111	no	F	53	Temporal right	70	exeresis + RT + CT	48	53
GBM112	no	M	54	corpus callosum and lateral ventricles	<50	exeresis	0	0
GBM113	no	M	71	Temporal left	70	exeresis + RT + CT	11	34
GBM114	no	M	65	Occipital left	80	exeresis + RT + CT	10	17
GBM115	no	M	44	Temporal left	70	exeresis + RT + CT	9	31
GBM116	yes	F	52	Tempo-parietal left	60	exeresis + RT	0	4
GBM120	no	F	82	Frontal left	70	exeresis + RT + CT	9	14
GBM139	yes	M	63	Frontal left	80	exeresis + RT + CT	12	16
GBM141	no	M	62	Temporal right	80	exeresis + RT + CT	6	12
GBM142	no	M	72	Tempo-parietal left	70	exeresis + RT + CT	3	5
GBM143	no	F	56	Temporal right	>80	exeresis + RT + CT	24	living
GBM144	no	F	50	Temporal right	60	exeresis + RT + CT	2	11
GBM145	no	F	70	Occipital right	N/A	exeresis + N/A	N/A	12
GBM149	yes	F	58	Frontal left	90	exeresis	1	3
GBM151	yes	M	67	Temporal right	60	exeresis + CT	0	2

*Derivation of res-GSC families after *ex-vivo* treatment

RT: radiotherapy; CT: chemotherapy; PFS: progression-free survival; OS: overall survival N/A: data not available.

Table 2. Genetic alterations in whole GBM cell populations

sample ID	res-GSC family	mutations			CNV	
		gene	consequence	VAF (%)	gene	CN
GBM17	yes	pTERT	c.1-124C>T	11.90		
		TP53	p.Q192*	11.00		
		PTEN	p.T277Nfs*21	12.40		
					MYC	3.00
					EGFR	8.30
GBM93	no	FGFR4	p.K737*	22.01		
		PTEN	p.K6E	20.39		
		RB1	p. N133Yfs*2	23.42		
GBM95	yes	pTERT	c.1-124C>T	9.10		
		PTEN	p.G156V	14.52		
		NF1	pY2285fs*5	9.26		
					CDKN2B	1.17
GBM96	yes	pTERT	c.1-124C>T	4.30		
		PIK3CA	p.H1047L	14.51		
GBM98	no	pTERT	c.1-124C>T	1.47		
		MLH3	p.K3R	49.19		
		MLH3	p.K3R	49.19		
		ERBB2	p.I654V	44.36		
		EGFR	p.S628Y	52.14		
		ERBB2	p.I654V	44.36		
GBM99	yes	pTERT	c.1-146C>T	32.44		
		TP53	p.R175H	70.42		
		RB1	p.Q436*	51.85		
		MSH4	p.F538Y	1.34		
		PTEN	p.H123N	10.34		
					CDKN2A	0.47
					PTEN	0.47
					MYCN	6.93
					EGFR	63.80
GBM105	no	pTERT	c.1-124C>T	11.14		
		EGFR	p.A289V	53.89		
		EGFR	p.S229C	25.30		
		ERBB2	p.T479M	47.18		
					EGFR	11.43
GBM107	no	pTERT	c.1-124C>T	2.51		
GBM108	no	pTERT	c.1-124C>T	7.69		
		POLD2	p.R103W	50.86		
		MLH3	p.S966P	47.41		
GBM111	no	pTERT	c.1-124C>T	16.02		
		EGFR	p.L62R	94.28		
		PMS2	p.V717M	49.42		
		FGFR3	p.S187Y	46.12		
		PMS2	p.S523T	24.72		
		PMS2	p.Y519C	23.24		
		PMS2	p.A520V	22.64		
					EGFR	44.17
					CDKN2A	1.05
					CDKN2B	0.94
GBM112	no				PDGFRA	4.20
GBM113					NF1	1.07
GBM114	no	pTERT	c.1-146C>T	6.83		

		EGFR	p.A289T	75.26		
					CDK4	35.75
					EGFR#	8.22
GBM115	no	pTERT	c.1-124C>T	0.27		
					MYCN	4.76
GBM116	yes	pTERT	c.1-124C>T	13.67		
		TP53	p.V272M	7.60		
		TP53	p.G266R	10.00		
		RB1	p.L569Ffs*3	10.56		
					PDFGRA	5.16
					MDM4	3.78
					MYC	4.03
GBM120	no	pTERT	c.1-124C>T	21.49		
		PIK3CA	p.G451R	22.99		
					CDK4	23.02
					MDM2	17.71
					EGFR	6.95
GBM139	yes	pTERT	c.1-146C>T	25.39		
		PTEN	p.A299T	57.31		
		TP53	p.R175H	39.58		
					PDGFRA	7.96
					CDKN2A	0.65
					CDKN2B	0.95
GBM141	no	pTERT	c.1-124C>T	20.31		
		EGFR	p.A289V	44.35		
		PTEN	p.M270R	15.21		
					EGFR#	31.52
GBM142	no	pTERT	c.1-124C>T	22.34		
		EGFR	p.R222C	9.35		
					EGFR#	12.30
GBM143	no	pTERT	c.1-124C>T	22.34		
		MSH3	p.P681S	51.51		
		MSH2	p.N127S	47.67		
					MDM2	38.05
					CDK4	25.53
GBM144	no	pTERT	c.1-124C>T	3.76		
		ERBB2	p.P8T	46.02		
		EXO5	p.M204V	51.66		
GBM145	no	pTERT	c.1-124C>T	12.55		
		EGFR	p.A289T	75.26		
					CDK4	35.75
					MDM2	34.93
					EGFR	8.22
GBM149	yes	pTERT	c.1-124C>T	18.57		
		TP53	p.R282W	28.74		
					CDKN2A	1.13
					CDKN2B	1.12
GBM151	yes	pTERT	c.1-124C>T	1.64		
		PTEN	p.W274R	5.56		
					CDKN2A	1.34
					MDM4	3.56

Presence of EGFRviii

VAF: variant allele frequency; CNV: copy number variation; CN: copy number.

Res-GSC families include members that display primary and/or secondary resistance to TMZ

In res-GSC families, we investigated the primary and secondary response to TMZ and its relationship with expression of MGMT, the main known driver of TMZ resistance [4].

We verified that the majority of available CTRL-NS (n=9/10) retained the MGMT promoter status detected in the matched parental GBMs, as analyzed either in a FFPE sample used for pathological diagnosis or in a sample of the whole cell population used for res-GSC derivation (Figure 3A). The only exception was GBM144, where MGMT promoter methylation was detected in the CTRL-NS but not in either original tumor sample. In CTRL-NS, MGMT mRNA and protein expression were consistent (i.e., inversely correlated) with MGMT promoter methylation, with the sole exception of GBM149, where the absence of MGMT promoter methylation did not associate with the expected MGMT expression (Figure 3A). This could depend on MGMT translocation under a different (methylated or silenced) promoter [91]. However, we disproved this hypothesis by FISH analysis in CTRL-NS (data not shown). Altogether, we concluded that CTRL-NS reflect MGMT expression observed in the parental tumor, which can be passed on to cultured GSCs and kept during GSC propagation due to the inheritance of the underlying epigenetic trait. In total, we derived 4 CTRL-NS representative of GBM expressing MGMT (MGMT-pos) and 6 CTRL-NS representative of GBMs not expressing MGMTs (MGMT-neg) (Figure 3A and Table 3).

We then evaluated the response of CTRL-NS to TMZ, which should represent the primary response of the corresponding GBMs (Figure 3B). Dosage curves of TMZ were administered every three days for three cycles (as outlined in the res-GSC families generation protocol, Figure 1D), and cell survival was assessed on day 9 after the start of treatment. This end point was chosen because at least two cell divisions are required to observe the effects of TMZ, and all NS met this requirement despite having different proliferative rates. These effects began to be detectable on day 6 for the CTRL-NS with the highest proliferation rate and could be effectively measured in almost all CTRL-NS by day 9, with the exception of GBM112, which exhibited an exceedingly slow proliferative rate. We defined as primary resistant those CTRL-NS that, after a 50 μM TMZ treatment, displayed a cell survival greater than 50% with respect to vehicle-treated controls. As expected, primary resistance to TMZ fully correlated with MGMT expression (even at low levels, as in GBM96 CTRL-NS, Figure 3A), while sensitivity correlated with the opposite (Figure 3B). In addition, the TMZ dosage curve highlighted that (i) the 25 μM dose was as effective as the highest concentration in discriminating between sensitive and resistant CTRL-NS; (ii) the lowest dose of 5 μM (corresponding to the dose detected in patients' CSF during treatment and representing the dose expected to reach the tumor [85]) was effective only in 1/5 MGMT-neg CTRL-NS (GBM144), while the remaining CTRL-NS displayed at least a partial resistance (Figure 3B).

Next, we evaluated the secondary response to TMZ, represented by the response of TMZ-NS. From all MGMT-pos GBMs (4/4), we derived GSC families encompassing the TMZ-NS member (Figure 3C). Not surprisingly, *ex-vivo* TMZ treatment of the MGMT-pos GBM whole cell populations did not affect cell viability, so that TMZ-NS were established (i.e. they reached passage p4) almost concomitantly with CTRL-NS (with a median of increase vs CTRL-NS of 12.5 days). In one case (GBM95), the derivation time of TMZ-NS was longer, possibly because of heterogeneous MGMT expression within the original tumor. All these TMZ-NS expressed MGMT as the parental GBM and displayed a level of TMZ resistance comparable to CTRL-NS (data not shown).

Conversely, we could derive the TMZ-NS member only from 3 out of 6 MGMT-neg GBMs (as deduced by lack of MGMT in CTRL-NS). In these cases, TMZ significantly affected the viability of the starting cell population, and TMZ-NS required a longer latency to be established (i.e., to reach p4) compared to CTRL-NS (with a median latency increase of 67.9 days vs. CTRL-NS). Notably, the MGMT-neg GBM149 family was an exception, as TMZ-NS established slightly before the CTRL-NS; the underlying mechanisms are still under investigations.

All these TMZ-NS derived from MGMT-neg GBMs continued to lack MGMT expression (Figure 3D). However, when assessed for their sensitivity to TMZ, in 2/3 cases (GBM17 and GBM151), TMZ-NS displayed a complete (secondary) resistance (Figure 3E) with respect to their CTRL-NS, after 9 days of treatment (a period allowing the accomplishment of two cell cycles in all NS, despite different proliferative rates, see above). Surprisingly, GBM149 TMZ-NS, although it exhibited features similar to primary resistant NS, such as the relatively short derivation time under TMZ selective pressure, continued to display sensitivity to TMZ, as well as its matched CTRL-NS.

Secondary resistance to TMZ of GBM17 and GBM151 TMZ-NS, was also confirmed by the use of a long-term assay (clonogenic assay), which measured the ability of cells to form growing colonies under treatment (Figure 3F) [92]. These TMZ-NS showed a significantly increased surviving fraction under TMZ treatment at 50 μM compared to CTRL-NS, also observed to a lesser extent at 5 μM in GBM151.

In conclusion, we showed that (i) the MGMT status of the original GBM tissue is mostly retained by GSCs (NS); (ii) in GSCs derived without therapeutic pressure (CTRL-NS), MGMT protein expression correlates with primary resistance to TMZ, while the absence of MGMT expression correlates with sensitivity to TMZ; (iii) in GSCs derived under TMZ therapeutic pressure, MGMT expression correlates with the selection of GSCs (TMZ-NS) that exhibit features similar to their matched controls, while the absence of MGMT expression prevents GSC derivation or leads to the emergence of GSCs with secondary resistance to TMZ, without re-expression of MGMT; in one exception, GSC survival following TMZ treatment was observed without acquisition of secondary resistance.

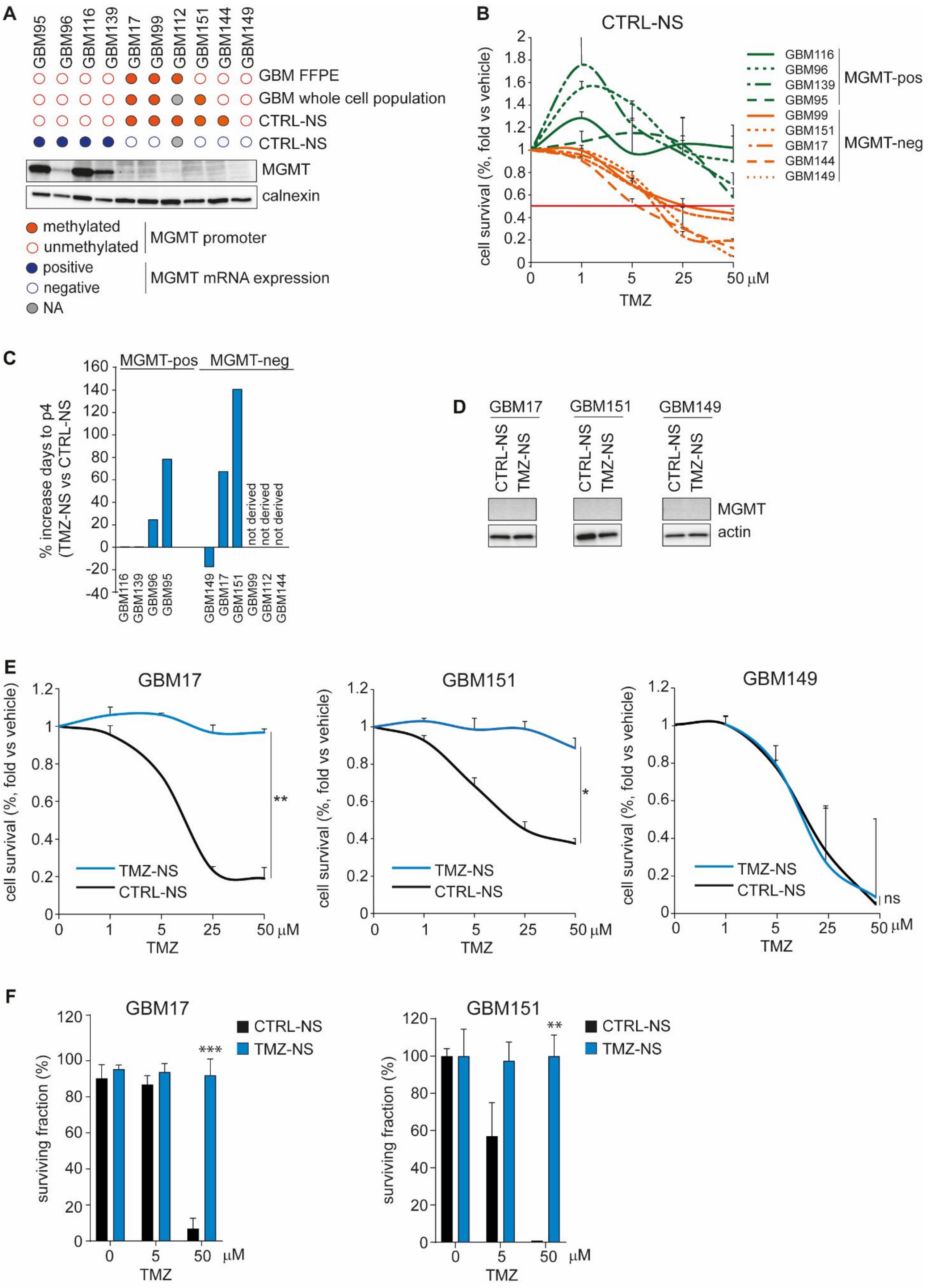
A
GBM95
GBM96
GBM116
GBM139
GBM17
GBM99
GBM112
GBM151
GBM144
GBM149
GBM FFPE
GBM whole cell population
CTRL-NS
CTRL-NS
MGMT
calnexin
methylated
unmethylated
MGMT promoter
positive
negative
NA
MGMT mRNA expression
B
CTRL-NS
cell survival (%, fold vs vehicle)
2
1.8
1.6
1.4
1.2
1
0.8
0.6
0.4
0.2
0
0
1
5
25
50 μM
TMZ
GBM116
GBM96
GBM139
GBM95
MGMT-pos
GBM99
GBM151
GBM17
GBM144
GBM149
MGMT-neg
C
% increase days to p4 (TMZ-NS vs CTRL-NS)
160
140
120
100
80
60
40
20
0
-20
-40
MGMT-pos
MGMT-neg
GBM116
GBM139
GBM96
GBM95
GBM149
GBM17
GBM151
GBM99
GBM112
GBM144
not derived
not derived
not derived
D
GBM17
GBM151
GBM149
CTRL-NS
TMZ-NS
MGMT
actin
E
GBM17
GBM151
GBM149
cell survival (%, fold vs vehicle)
1.2
1
0.8
0.6
0.4
0.2
0
0
1
5
25
50 μM
TMZ
TMZ-NS
CTRL-NS
**
*
ns
F
GBM17
GBM151
surviving fraction (%)
120
100
80
60
40
20
0
0
5
50 μM
TMZ
CTRL-NS
TMZ-NS
***
**

Figure 3. Res-GSC families include members that display primary and/or secondary resistance to TMZ

(A) Evaluation of MGMT status after GSC derivation. MGMT promoter methylation was evaluated by pyrosequencing in patient biopsy FFPE and by bisulfite-ddPCR in whole GBM cell population and CTRL-NS. MGMT gene expression was evaluated in CTRL-NS by Real Time PCR. MGMT protein expression in CTRL-NS was evaluated by western blot. Calnexin: loading control

(B) Cell survival (fold vs. vehicle) of the indicated CTRL-NS, measured 9 days after TMZ administration (1-50 µM). Data are shown as mean ± SEM of at least two independent experiments.

(C) Derivation times (days from aspirate processing to p4) of TMZ-NS (blue bars) in different res-GSC families (columns), measured as percentage increase vs. CTRL-NS. TMZ-NS were grouped according to MGMT expression in MGMT-pos and MGMT-neg TMZ-NS. Passage 4 was chosen as the passage at which cells have just stabilized their clonogenic abilities. Not derived: TMZ-NS not derived in the indicated res-GSC families.

(D) Expression of MGMT in CTRL-NS and TMZ-NS of MGMT-neg families, as evaluated by western blot. Actin: loading control.

(E) Cell survival (fold vs. vehicle) of CTRL-NS and TMZ-NS of the indicated res-GSC families, measured 9 days after TMZ administration (1-50 µM). Data are shown as mean ± SEM of at least two independent experiments. Student's paired t test, $^{*}p<0.05$, $^{**}p<0.01$.

50 µM TMZ response: GBM17 $p= 0.006256$; GBM151 $p= 0.013988$; GBM149 not significant.

(F) Surviving fraction (%) of CTRL-NS and TMZ-NS of GBM17 and GBM151 families, measured by clonogenic assay. Data are shown as mean ± SEM of at least two independent experiments. Student's paired t test, $^{*}p<0.05$, $^{**}p<0.01$ $^{***}p<0.001$.

50 µM TMZ response: GBM17 $p= 0.000173$; GBM151 $p= 0.002529$

Table 3. MGMT promoter methylation in GBMs and res-GSC families

sample ID	GBM				res-GSC family				
	FFPE	whole cell population			CTRL-NS	TMZ-NS	IR-NS	overall family	consistency
		cell %	cell % normalized on pTERT	evaluation normalized on pTERT					
GBM17	met	9.34	84.22	met	97.56	100	98.83	met	**
GBM93	unmet	0.02	N/A	N/A	n.d.	n.d.	n.d.	n.d.	-
GBM95	unmet	0.19	2.09	unmet	0.11	0.05	0	unmet	**
GBM96	unmet	0.27	6.28	unmet	18.58	7.51	n.d.	unmet	**
GBM98	int met	1.22	82.99	met	n.d.	n.d.	n.d.	n.d.	n.d.
GBM99	high met	42.02	129.53	met	99.98	n.d.	99.77	met	**
GBM105	low met	7.9	70.92	met	n.d.	n.d.	n.d.	n.d.	n.d.
GBM107	int met	1.24	49.40	met	n.d.	n.d.	n.d.	n.d.	n.d.
GBM108	high met	2.7	35.11	met	n.d.	n.d.	n.d.	n.d.	n.d.
GBM111	high met	16.9	105.49	met	n.d.	n.d.	n.d.	n.d.	n.d.
GBM112	int met	13.2	N/A	N/A	76.3	n.d.	n.d.	n.d.	n.d.
GBM113	unmet	0	N/A	N/A	n.d.	n.d.	n.d.	n.d.	n.d.
GBM114	unmet	0.17	2.49	unmet	n.d.	n.d.	n.d.	n.d.	n.d.
GBM115	unmet	0.03	11.11	unmet	n.d.	n.d.	n.d.	n.d.	n.d.
GBM116	unmet	0.2	1.46	umet	0	0	0.05	unmet	**
GBM120	unmet	23.6	109.82	met	n.d.	n.d.	n.d.	n.d.	n.d.
GBM139	unmet	0.39	1.51	unmet	0.2	0.27	0.14	unmet	**
GBM141	high met	15.3	75.33	met	n.d.	n.d.	n.d.	n.d.	n.d.
GBM142	unmet	0.35	1.57	unmet	n.d.	n.d.	n.d.	n.d.	n.d.
GBM143	int met	0	N/A	N/A	n.d.	n.d.	n.d.	n.d.	n.d.
GBM144	low met	0.57	15.16	unmet	85.17	n.d.	n.d.	n.d.	n.d.
GBM145	unmet	2.19	17.45	unmet	n.d.	n.d.	n.d.	n.d.	n.d.
GBM149	unmet	0.8	4.31	unmet	3.52	0.13	1.33	unmet	**
GBM151	unmet	0.7	42.68	met	96.05	87.04	96.05	met	*

MGMT methylation in patients' FFPE was evaluated by pyrosequencing according to a clinical score (unmet: 0-10; low: 10-20; int: 20-30; high: >30. Unmet and low are clinically considered unmethylated, int and high as methylated. MGMT methylation in GBM whole cell populations and in res-GSC families were evaluated by ddPCR data as described in Material and Methods. Samples are considered methylated when >30. For GBM suspension, normalization on the percentage of pTERT alterations was done to evaluate tumor cells only.

** consistency of MGMT status among patient biopsy, GBM suspension and res-GSC family members; *consistency of MGMT status between GBM suspension and res-GSC family members.

met: methylated; unmet: not methylated; NA: N/A: not applicable (cases in which pTERT is wild type); n.d: not derived.

Secondary resistance to TMZ in MGMT-neg GSCs is genetically determined

A major cause of secondary resistance to therapeutic treatment is the emergence of a GSC subclone harboring genetic alteration(s), either pre-existing or induced by the treatment itself, that favor subclone survival under therapeutic pressure [4, 93]. Thus, we analyzed the genetic landscape of TMZ-NS derived from MGMT-neg GBMs (GBM17, GBM151, and GBM149), representing subclones able to survive TMZ treatment, and, in the case of GBM17 and GBM151, also displaying secondary resistance. The genetic landscape of TMZ-NS was compared to that of CTRL-NS, which represents GSCs not subjected to therapeutic selection.

By the GBM-target panel, we observed that typical GBM driver genetic alterations such as those affecting the TERT promoter, PTEN and TP53 - detectable in the whole GBM cell suspension - were retained and shared among res-GSC family members (CTRL-NS and TMZ-NS), with VAFs suggesting that NS are monoclonal, at least with respect to these alterations (Figure 4A and Table 4). In contrast, EGFR amplification present in the original GBM17 tumor was lost in GSC family members, likely due to culture conditions [86] (Figure 4A and Table 4).

In addition, in secondary resistant MGMT-neg TMZ-NS we observed the emergence of private genetic alterations that were undetectable by the NGS panel in both the original GBM population and in the CTRL-NS (Figure 4A; Table 2 and Table 4). These alterations, primarily affecting DNA Damage Repair (DDR) mechanisms, include mutations of MSH2 and MSH6 genes predicted to be pathogenic (Cosmic). Notably, MSH2 and MSH6 are key components of the Mismatch Repair (MMR) machinery, whose deficiency has been reported to confer TMZ resistance [4, 93] (Figure 4A and Table 4). This apparent paradox - DNA damage repair deficiency resulting in resistance to a DNA damaging agent - is explained by the fact that MMR is required to recognize base mismatch caused by O6-methylation of guanine induced by TMZ, block DNA replication, and induce apoptosis in cases of repair failure. MMR deficiency leads to inability to undergo apoptosis in response to DNA damage accumulation. Although

MMR deficiency allows the accumulations of genetic alterations and increases mutational burden [4], we did not observe a shift towards a microsatellite instability (MSI) phenotype at the time of res-GSC members establishment (passage 10) (data not shown). However, we cannot rule out the possibility that MSI may appear at later passages, which is currently under investigation.

In the case of GBM149 TMZ-NS, which survived TMZ treatment without acquiring secondary resistance, we did not observe the emergence of any MMR gene alterations. However, we did report other genetic changes, such as the appearance of an additional TP53 mutation (undetectable in the original GBM population or in the CTRL-NS) and the loss of a BRAF mutation detectable in CTRL-NS (Figure 4A and Table 4). The latter is a rare GBM alteration associated with extended survival, so the loss of BRAF after therapeutic selection is consistent with increased aggressiveness and warrants further investigation [94].

Since genetic alterations could either be selected or induced by therapies, we investigated whether *de novo* MMR gene mutations found in TMZ-NS were pre-existing in the parental GBMs or if they were linked to the mutagenic activity of TMZ. Analyses performed by ddPCR, within the detection limit of the methodology, disproved this hypothesis (Figure 4B), suggesting instead that these alterations were acquired as a consequence of TMZ exposure. Although, due to the limited scope of our NGS panel, we were unable to determine whether the overall gene mutations carried the signature typically associated with TMZ mutagenic activity [95], the DNA base changes observed in MMR genes (mostly C>T) are consistent with TMZ activity.

To investigate the functional impact of the detected MMR inactivating mutations on DNA damage repair, we leveraged an *in vitro* assay that quantitatively measures the ability of cells to repair mismatches at basal conditions. This assay, known as fluorescence-based multiplex flow-cytometric host cell reactivation assay (FM-HCR), utilizes a fluorescent reporter gene construct chemically modified to present a mismatch, so that fluorescence can be detected only after repair in MMR-proficient cells (Figure

4C) [96, 97]. In both secondary resistant TMZ-NS harboring MMR gene alterations (GBM17 and GBM151) we observed significantly reduced reporter expression compared to CTRL-NS (Figure 4D), indicating that these genetic alterations associate with MMR deficiency and are likely responsible for the secondary TMZ resistance.

Finally, we also evaluated chromosomic alterations (Figure 4E-F). Interestingly, all three MGMT-neg TMZ-NS displayed slightly simpler ploidy compared to CTRL-NS (Figure 4E), but the number of chromosomal aberrations significantly increased (median increase from 3 to 6), as expected from the genotoxic activity of TMZ (Figure 4F). Chromosomal aberrations were observed not only in the secondary resistant TMZ-NS, likely due to MMR deficiency, but also in TMZ-NS that remained sensitive to TMZ (GBM149). In the latter case, chromosomal instability could be favored by the accumulation of TP53 mutations.

In summary, genetic analysis suggests that, in MGMT-neg TMZ-NS, the acquisition of MMR inactivating mutations could be responsible for the emergence of secondary resistance, as previously reported in patients [36, 98]. This indicates the reliability of our *ex vivo* resistance model and offers a manageable experimental system to further characterize and possibly target these resistance mechanisms.

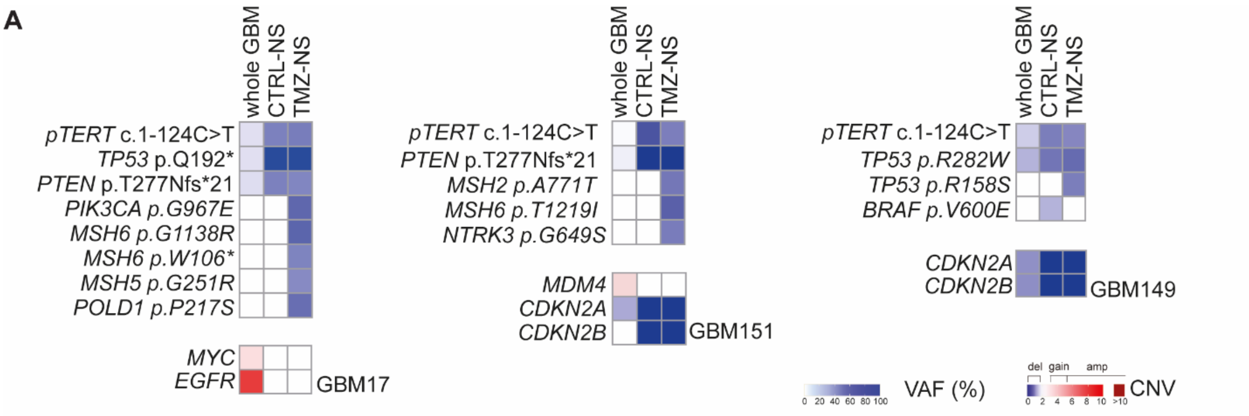

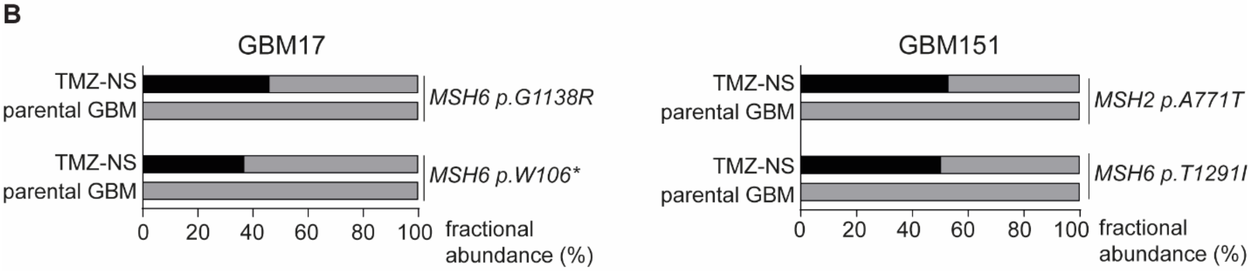

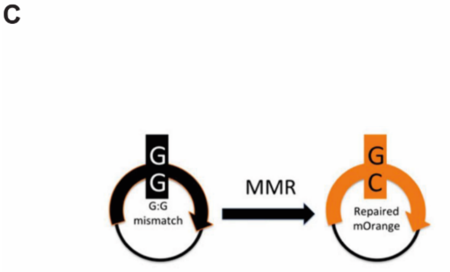

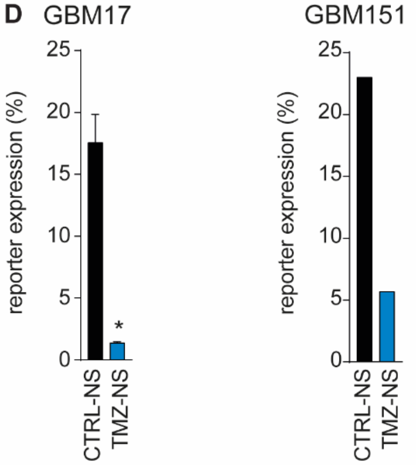

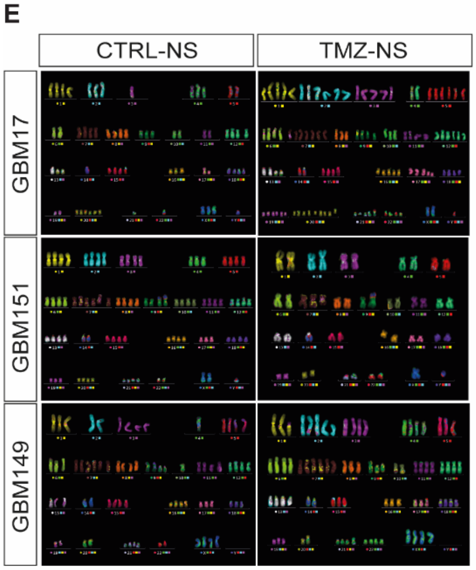

F

res-GSC family	chr. aberrations	
	CTRL-NS	TMZ-NS
GBM17	5	9 (+10)
GBM151	2	5 (+3)
GBM149	3	6 (+7)

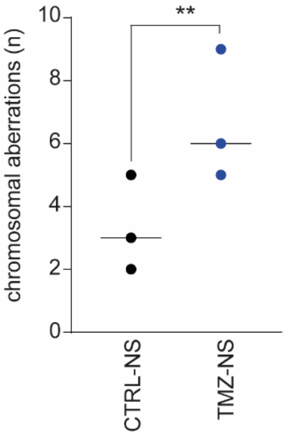

Figure 4. Secondary resistance to TMZ in MGMT-neg GSCs is genetically determined

(A) Pathogenic alterations (mutation variant allele frequency, VAF, and copy number variation, CNV) detected by NGS GBM-target panel, including GBM driver genes and DNA selected damage repair-associated genes) in MGMT-neg res-GSC family members CTRL-NS e TMZ-NS.

(B) Genetic alterations in MMR genes evaluated by droplet digital PCR in GBM17 (left) and GBM151 (right) TMZ-NS and parental GBM. Data are shown as fractional abundance of the mutant (black) and wild type (grey) alleles.

(C) Schematic representation of the fluorescence-based multiplex flow-cytometric host cell reactivation assay (FM-HCR) used to evaluate MMR. Modified from Nagel et al. [96]

(D) Evaluation of MMR capacity measured by FM-HCR in CTRL-NS and TMZ-NS from GBM17 (left) and GBM151 (right) 24 hours from the transfection. Data are represented as z-values and are shown as mean ±SEM of two independent experiments (GBM17) or as single experiment (GBM151). * Student's paired t test, GBM17 TMZ vs. CTRL-NS p= 0.018734

(E) Cell ploidy and chromosomal aberrations of MGMT-neg res-GSC family members CTRL-NS e TMZ-NS evaluated by multicolour fluorescence *in situ* hybridization (M-FISH). Representative images are shown.

F) Evaluation of chromosomal aberration number in MGMT-neg res-GSC family members CTRL-NS e TMZ-NS, measured by M-FISH. Numbers indicate de total number of detected alterations showing a significant increase in TMZ-NS (p=0.009). Numbers in brackets indicate the total number of chromosomal aberrations acquired by TMZ-NS with respect to CTRL-NS. Median of chromosomal aberrations in CTRL-NS and TMZ-NS from the three MGMT-neg res-GSC families is shown in the scatter plot (right panel).**Student's paired t test, p<0.01

Table 4. Genetic alterations in res-GSC families selected by therapies

sample ID	res-GSC family member	mutations			CNV	
		gene	consequence	VAF (%)	gene	CN
GBM17	CTRL-NS	pTERT	c.1-124C>T	46.59		
		TP53	p.Q192*	100.00		
		PTEN	p.T277Nfs*21	46.39		
	TMZ-NS	pTERT	c.1-124C>T	47.62		
		TP53	p.Q192*	100.00		
		PTEN	p.T277Nfs*21	44.89		
		PI3KCA	p.G967E	56.32		
		MSH6	p.G1138R	57.65		
		MSH6	p.W106*	45.65		
		MSH5	p.G251R	43.15		
		POLD1	p.P217S	53.61		
GBM95	CTRL-NS	pTERT	c.1-124C>T	49.15		
		PTEN	p.G156V	100.00		
		NF1	p.Y2285fs*5	100.00		
					CDKN2A	0
					CDKN2B	0
	IR-NS	pTERT	c.1-124C>T	49.56		
		PTEN	p.G156V	100.00		
		NF1	p.Y2285fs*5	99.31		
					CDKN2A	0
					CDKN2B	0
GBM149	CTRL-NS	pTERT	c.1-124C>T	49.39		
		TP53	p.R282W	52.42		
		BRAF	p.V600E	28.98		
					CDKN2A	0
					CDKN2B	0
	TMZ-NS	pTERT	c.1-124C>T	46.10		
		TP53	p.R282W	55.90		
		TP53	p.R158S	49.38		
					CDKN2A	0
					CDKN2B	0
GB151	CTRL-NS	pTERT	c.1-124C>T	66.75		
		PTEN	p.W447R	99.82		
					CDKN2A	0
					CDKN2B	0
	TMZ-NS	pTERT	c.1-124C>T			
		PTEN	p.W447R			
		MSH2	p.A771T			
		MSH6	p.T1219I			
		NTRK3	p.G649S			
					CDKN2A	0
					CDKN2B	0

VAF: variant allele frequency; CNV: copy number variation; CN: copy number.

Res-GSC families include members that display primary and/or secondary resistance to IR

Next, in res-GSC families we investigated the primary and secondary response to ionizing radiation and the mechanisms underlying radioresistance. First, we evaluated the response of CTRL-NS to IR, which should represent the primary response of the corresponding GBMs. To this end, we assessed CTRL-NS cell viability 24 and 48 h after treatment with single (5 Gy) or fractionated (2 Gy x 3 consecutive days) biologically equivalent IR doses, chosen to be representative of patient radiotherapy [3]. As for TMZ resistance, NS were considered primary resistant to IR when cell survival was >50% compared to untreated cells in either single or fractioned IR dose.

We observed that most of CTRL-NS (6/10) were primarily radioresistant, with cell survival values ranging from 65% to 96% in fractioned treatment (Figure 5A), and from 63% to 100% in single treatment, showing good correspondence between the response to both treatments (Figure 5B), consistent with previous findings by our laboratory and others [58, 60]. Three out of ten CTRL-NS displayed a partial sensitivity, with cell survivals around 50%. Interestingly, one CTRL-NS (1/10) displayed complete sensitivity to IR, with a percentage of cell survival rate of around 5% (GBM95, Figure 5A and B).

Next, we evaluated the secondary response to IR, represented by the response of IR-NS. From all primary radioresistant GBMs (6/6), we successfully derived IR-NS members (Figure 5C). Not surprisingly, during *ex-vivo* selection, IR did not significantly affect the viability of the starting GBM cell populations, and IR-NS were established almost simultaneously with CTRL-NS (median percent increase of 14 days). Conversely, radiosensitivity of original GBMs (as measured in the corresponding CTRL-NS) prevented GSC derivation under ex-vivo IR treatment. As a result, we derived the IR-NS member from only 1/4 radiosensitive GBMs (GBM95), with a significantly longer latency compared to CTRL-NS (percent increase of 121.1 days) (Figure 5A-C).

Similar to MGMT-neg TMZ-NS members derived under TMZ treatment, GBM95 IR-NS, emerging after the IR selection protocol, displayed a reduced sensitivity to IR and could be defined as secondary resistant. Indeed, while GBM95 CTRL-NS mostly died in response to fractionated or single IR doses, their matched IR-NS survived significantly more - around 5-fold – for both IR doses tested (Figure 5D). This secondary radioresistance was also confirmed using a long-term clonogenic assay (Figure 5E), where IR-NS displayed a 7.2-fold increase in the surviving fraction compared to CTRL-NS.

In summary we showed that the majority of GSCs representative of treatment-naïve GBMs (CTRL-NS) exhibit a high degree of primary radioresistance. Primary GBM radiosensitivity prevents GSC derivation under IR therapeutic pressure. In cases where GSCs were derived from radiosensitive GBMs, secondary (though still partial) radioresistance can be observed.

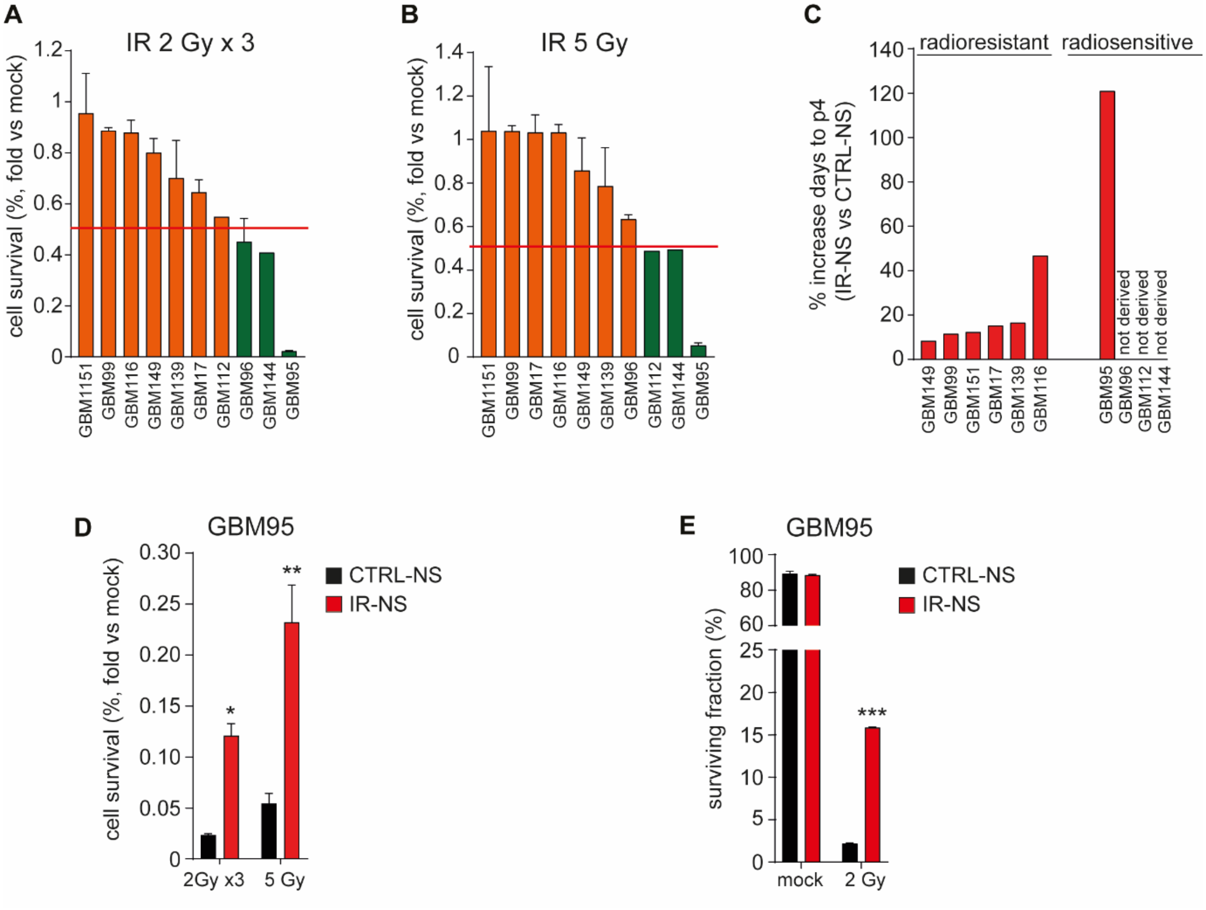

Figure 5. Res-GSC families include members that display primary and/or secondary resistance to IR

(A) Cell survival (fold vs. mock) of the indicated CTRL-NS, measured 48 h from the last dose of irradiation (2 Gy x 3 days). Data are shown as mean ± SEM of at least two independent experiments. mock: no IR.

(B) Cell survival (fold vs. mock) of the indicated CTRL-NS, measured 48 irradiation (5 Gy). Data are shown as mean ± SEM of at least two independent experiments. mock: no IR

(C) Derivation times to p4 of IR-NS (red bars) in different res-GSC families (columns), measures as percentage increase to CTRL-NS. IR-NS were grouped according to the radio-resistance or sensitivity or CTRL-NS (primary resistance/sensitivity). Not derived: IR-NS not derived in the indicated res-GSC families.

(D) Cell survival (fold vs. mock) of GBM95 CTRL and IR-NS, measured at 48 from the last dose of irradiation. Data are shown as mean ± SEM of at least two independent experiments. Student’s paired t test,* p= 0.023822, **p= 0.005872

(E) Surviving fraction (%) of GBM95 CTRL-NS and IR-NS, measured by clonogenic assay. Data are shown as mean ± SEM of a representative experiment.***Student’s paired t test, p <0.000001

Secondary resistance to IR relies on enhanced DDR ability

As with TMZ secondary resistance, we hypothesized that emergence of radioresistance could rely on the acquisition or selection of private genetic alterations that remain obscure. We therefore evaluated the genetic features of the secondary resistant GBM95 IR-NS using the GBM-target panel and M-FISH karyotyping. Both CTRL- and IR-NS retained and shared driver gene alterations already detected in the whole GBM cell suspension, such as an activating mutation of the TERT promoter and inactivating mutations of PTEN and NF1 oncosuppressor genes, all exhibiting VAFs consistent with NS monoclonality. Additionally, both NS displayed complete deletion of CDKN2A-B genes, which had already been detectable as a heterozygous loss in the parental GBM (Figure 6A, Table 2 and Table 4). Interestingly, no private genetic alterations (Figure 6A) or changes in the number of chromosomal aberrations (Figure 6B) were detected in the IR-NS compared to the CTRL-NS. Nevertheless, a more comprehensive whole exome sequencing analysis is ongoing to explore genes not included in the GBM-target panel and to study possible micro-insertions and deletions induced by IR, which were previously reported in GBM tissues [99]. Notably, at the chromosomal level we observed a significant simplification of the karyotype, with IR-NS showing an increased representation of a diploid karyotype (Figure 6C), a phenomenon that has also been reported in literature to occur in GBM recurrences [100]. This could favor a non-catastrophic cell division and the inheritance of the genetic material.

In addition to genetic mechanisms, radioresistance has been linked by us and others to adaptive mechanisms that enhance the efficiency of DNA Damage Response (DDR) activation [58-60, 101]. Therefore, we investigated the expression of DDR key players in GBM95 CTRL- and IR-NS. Under basal conditions, both NS showed comparable levels of Chk2 and RAD51, two proteins involved in the homologous recombination (HR) pathway, which is primarily responsible for repairing double-strand breaks induced by IR in proliferating cells. However, 3 hours after irradiation, IR-NS exhibited an enhanced DDR compared to CTRL-NS, including (i) a stronger increase in Chk2 phosphorylation, compared to CTRL-NS (Figure 6D), and (ii) a sharp increase in RAD51 expression, compared to both IR-NS in basal conditions and CTRL-NS after irradiation. Consistently, at the same time point, phosphorylation of histone H2AX (known as γH2AX), which is essential for marking DNA double-strand breaks for repair, was still present in CTRL-NS but had disappeared in IR-NS, suggesting that the latter had already resolved the damage through its superior DDR activation (Figure 6D).

To analyze the dynamics of DNA damage repair, we evaluated H2AX phosphorylation in a time-course experiment (Figure 6E). Shortly after IR treatment (1 h), around 50% of IR-NS nuclei were positive for γH2AX, while none of the CTRL-NS nuclei analyzed were positive. The situation reversed at later time points, with CTRL-NS nuclei reaching around 80% of positivity, which persisted until the experimental endpoint, whereas IR-NS reduced that percentage to normal levels within approximately 2 h (Figure 6E). These observations suggest that IR-NS could repair the DNA damage more rapidly and effectively than CTRL-NS, likely as result of increased ability to activate mechanisms responsible for DNA detection and assembly of the repair machinery, which will be further investigated.

In summary, we showed that the secondary resistance to IR associated with quicker and more efficient repair of DNA double-strand breaks, likely relying on an adaptive increased ability to activate the DDR. Although apparently not linked to genetic alterations, DDR proficiency of IR resistant GSCs could potentially be fixed (e.g., via epigenetic mechanisms) and become inheritable.

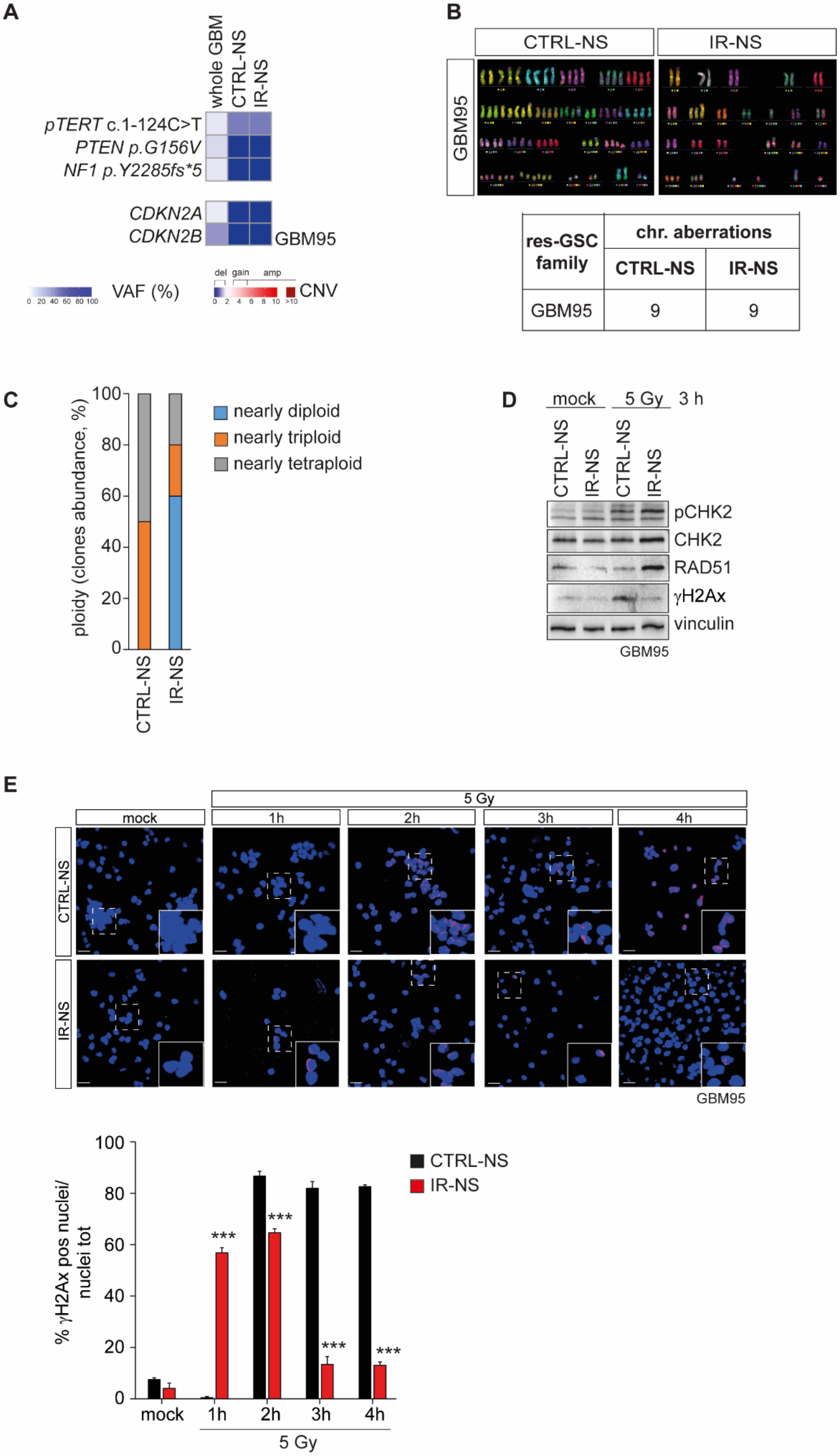

res-GSC family	**chr. aberrations**	
	CTRL-NS	**IR-NS**
GBM95	9	9

Figure 6. Secondary resistance to IR relies on enhanced DDR ability

(A) Pathogenic alterations (mutation variant allele frequency, VAF, and copy number variation, CNV) detected by NGS GBM-target panel, including GBM driver genes and DNA selected damage repair-associated genes) in GBM95 CTRL-NS and IR-NS.

(B) Cell ploidy and chromosomal aberrations of GBM95 CTRL-NS and IR-NS evaluated by multicolour fluorescence in situ hybridization (M-FISH) (top panel). Representative images are shown. Bottom panel: evaluation of the number of chromosomal aberration number in GBM95 CTRL-NS and IR-NS, measured by M-FISH.

(C) Evaluation of ploidy in GBM95 CTRL-NS and IR-NS, as measured by M-FISH.

(D) Expression of indicated DDR players in GBM95 CTRL-NS and IR-NS at basal conditions and at 3 hours post IR. Vinculin: loading control.

(E) Representative images showing the expression of γH2AX in GBM95 CTRL-NS and IR-NS in a time-course experiment (5 Gy IR dose), as measured by immunofluorescence (top). Quantification of nuclei positive for γH2AX expression in each condition (bottom). γH2AX: red dots. Scale bar, 25 μm. Student's paired t test, *** $p<0.000001$

Secondary resistant GSCs display increased stem-like features

Enhanced therapeutic resistance, whether increased or acquired *de novo*, has been associated with increased stem-like features and tumor aggressiveness [34, 83, 102]. To evaluate whether this applies to our models, we set out to measure the clonogenic and tumorigenic abilities of secondary resistant NS.

In both GBM17 TMZ-NS (representative of secondary resistance to TMZ) and GBM95 IR-NS (representative of secondary resistance to IR), we observed increased stem cell frequency (Figure 7A) and clonogenicity (Figure 7B), compared to their matched CTRL-NS. Interestingly, in CTRL-NS, stem-cell frequency was significantly lower in GBM17 compared to GBM95 (1.5 vs 14%). Nevertheless, the increase in stemness was significantly higher in the former than in the latter (4-fold increase in GBM17 vs less than 2-fold in GBM95).

These in vitro assessments were consistent with preliminary *in vivo* measurement of NS tumorigenic potential. Subcutaneous injection of NS into immunocompromised mice showed higher tumorigenicity of GBM95 CTRL-NS (5/5 mice with tumors) compared to GBM17 CTRL-NS (1/5 mice with tumors), consistent with the respective stem cell frequency. Interestingly, while GBM17 CTRL-NS displayed a limited tumor take (1/5 mice), its matched secondary resistant TMZ-NS exhibited a greater take (3/5 mice). As the ability of NS to generate subcutaneous experimental GBMs is known to be limited, it is required to assess NS orthotopically, and this is currently ongoing.

Although still preliminary, these findings suggest that the emergence of secondary resistance either to TMZ or IR is accompanied by increased stem cell frequency and clonogenicity, which may associate with increased tumorigenic potential.

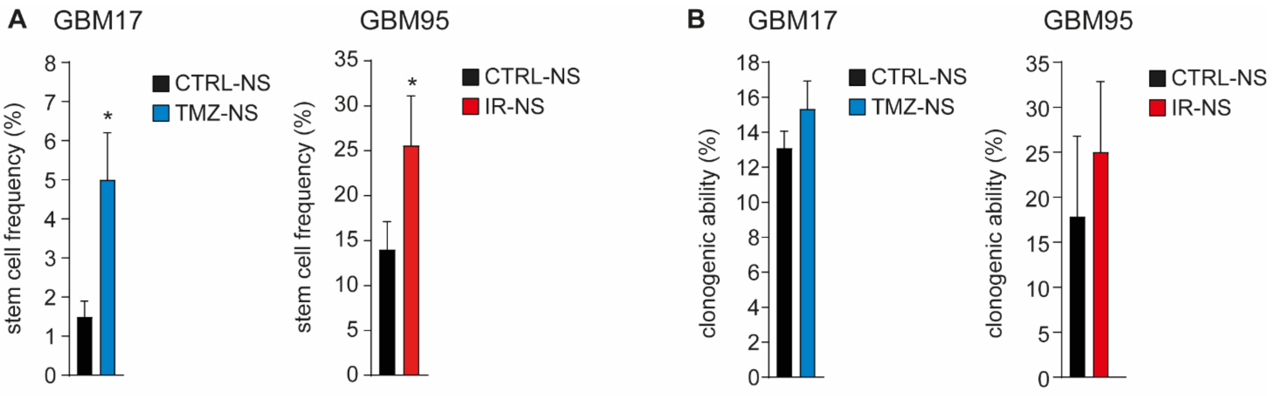

C

res-GSC family	member	tumor take
GBM17	CTRL-NS	1/5
	TMZ-NS	3/5
GBM95	CTRL-NS	5/5
	IR-NS	5/5

Figure 7. Secondary resistant GSCs display increased stem-like features

(A) Stem cell frequency in res-GSC GBM17 (left) and GBM95 (right) CTRL compared with matched family members showing secondary resistance. Limiting dilution assay data are represented as mean ± SEM of at least two independent experiments. *Pairwise chi square test: GBM17 TMZ-NS vs. CTRL-NS p=0.000351; GBM095 IR-NS vs. CTRL-NS p=0.0320

(B) Clonogenic ability in res-GSC GBM17 (left) and GBM95 (right) CTRL compared with matched family members showing secondary resistance. Clonogenic assay data are represented as mean ± SEM of at least two independent experiments.

(C) Evaluation of tumor take in mice after subcutaneous injection of the indicated res-GSC family members.

Secondary resistant GSCs display changes in RTK expression

Therapeutic resistance of GSCs is known to rely on preferential activation of main survival pathways, which could be sustained by increased expression and activation of Receptor Tyrosine Kinases [41, 59, 60] (RTKs). Therefore, in secondary resistant GSCs, we evaluated RTKs that are frequently expressed (and genetically altered) in GBMs [17, 24, 103]. In both TMZ- and IR- secondary resistant NS (GBM17 TMZ-NS and GBM95 IR-NS as representative cases), we observed significant protein overexpression of EGFR and MET, and a milder increase in PDGFRα expression compared with CTRL-NS, as measured by western blot (Figure 8A). In contrast, PDGFRβ was reduced, consistent with its alternative role to EGFR in sustaining overlapping pathways [24]. Regarding the FGF receptor family, which was poorly expressed in both GSC families, we observed a general expression decrease in GBM017 TMZ-NS, while in GBM95 IR-NS, the only FGFR family member expressed (FGFR1) remained unaltered (Figure 8A).

In addition, we analyzed RTK expression by flow cytometry to determine whether the expression changes observed in western blot were due to an increased percentage of RTK-expressing cells or increased RTK expression within positive cells, measured as mean fluorescence intensity (MFI) (Figure 8B-C). In GBM17 GSC family, we observed widespread EGFR and MET expression in CTRL-NS as well as in TMZ-NS, with significantly higher levels of RTK expression (MFI) in the latter, suggesting sustained transcriptional induction in TMZ-NS. In contrast, PDGFRα, PDGFRβ and FGFR2 were expressed in a limited percentage of cells, and changes in such percentages observed in TMZ-NS compared to CTRL-NS, without changes in expression levels (MFI), mirrored variations observed in western blot. This suggests that TMZ treatment may have selected (or counterselected) cell subpopulations expressing these receptors (Fig. 8B-C). In GBM95 GSC family, we observed negligible EGFR expression in both CTRL-NS and IR-NS, consistent with the low levels of this RTK –although increased in IR-NS- measured in western blot (Figure 8 B-C). MET, however, was expressed in 40% of CTRL-NS cells, which increased to 97% in IR-NS, along with a significant rise in expression levels

(MFI) (Figure 8 B-C). This suggests both positive selection of the MET-expressing subpopulation and sustained MET transcriptional induction by radiotherapy, consistent with the MET known role in promoting radioresistance, as shown by our laboratory and others [60, 104, 105]. A similar enrichment in PDGFRα expressing cells was also observed in IR-NS vs. CTRL-NS, also suggesting a possible radioprotective role of this RTK. Remarkably, the features of RTK expression remained stable throughout *in vitro* propagation.

Changes in RTK expression were reflected in the NS proliferative response to their respective growth factors (GF), each supplied individually. Indeed, GBM17 TMZ-NS exhibited an increased proliferative response to EGF or HGF but a decreased response to FGF or PDGF, compared to its matched CTRL-NS (Figure 8D). The response to FGF2 was unexpected: despite the relatively low expression of FGF2 main receptors (FGFR1 and FGFR2), CTRL-NS displayed a striking proliferative response to the factor, while TMZ-NS exhibited a remarkably reduced sensitivity, consistent with the decreased percentage of FGFR2-expressing cells (Figure 8D). The underlying mechanism of this unexpected sensitivity to FGF2 is currently under investigation. GBM95 IR-NS displayed an increased proliferative response to EGF, FGF2 or PDGF but not to HGF, suggesting that, in these cells, MET activity may primarily promote survival rather than proliferation (Figure 8D).

The different proliferative responses to individual growth factors in secondary resistant NS compared to their matched CTRL-NS may help explain the differences in growth rates in the medium used for selection and propagation (including EGF, FGF, PDGF and HGF) (Figure 8E). Specifically, TMZ-NS displays a statistically slower growth rate, possibly due to its reduced sensitivity to FGF2, while IR-NS displays a faster growth rate, compared to their matched CTRL-NS (Figure 8E).

In summary, both TMZ- and IR- secondary resistant GSCs display significant changes in the expression of the main RTKs regulating their proliferation and survival. Notably, both TMZ- and IR-NS displayed increased expression of MET and/or EGFR, two RTKs known to activate signaling mechanisms leading to protection from apoptosis and therapeutic resistance.

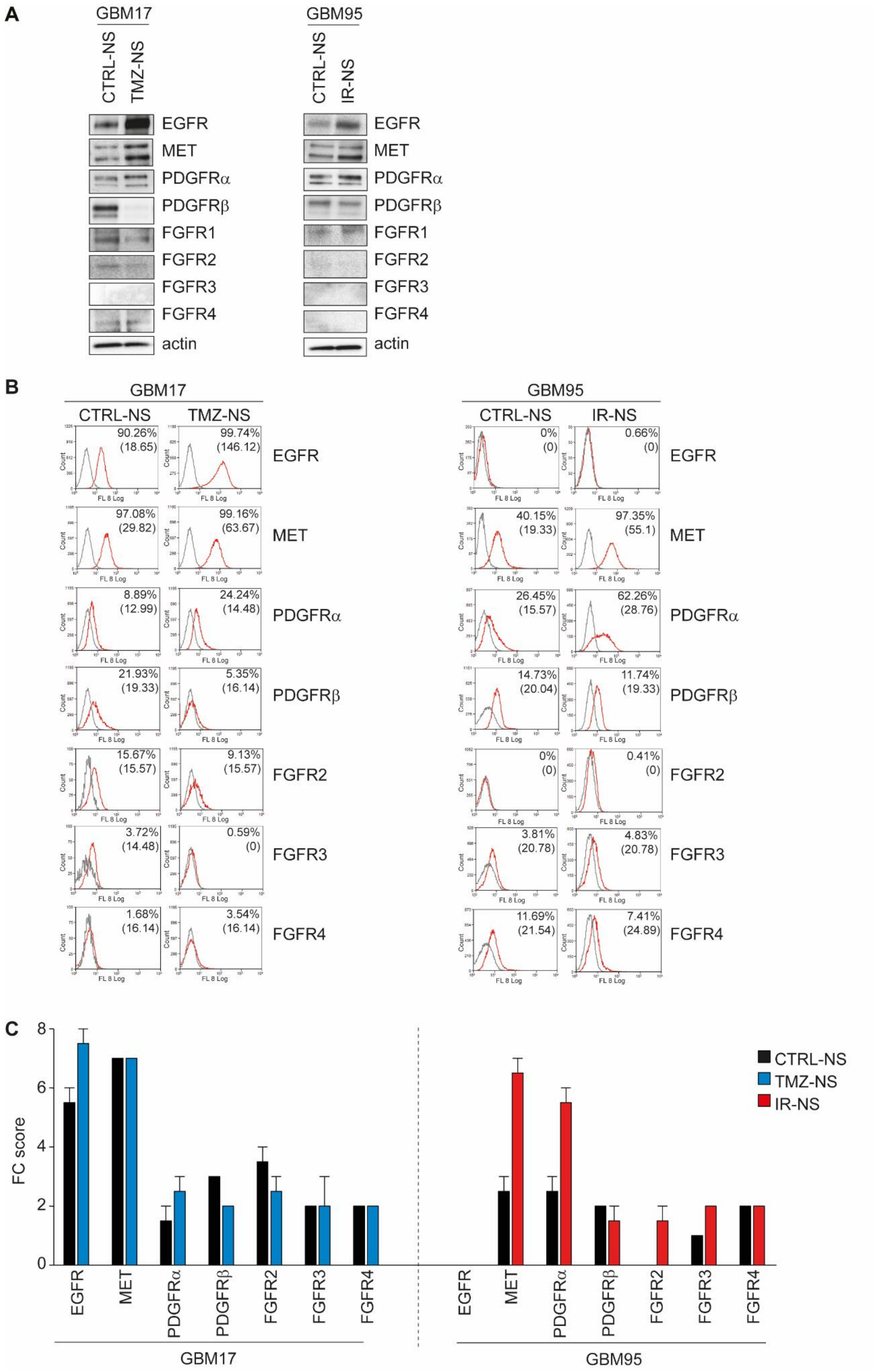
A
GBM17
CTRL-NS
TMZ-NS
GBM95
CTRL-NS
IR-NS
EGFR
MET
PDGFRα
PDGFRβ
FGFR1
FGFR2
FGFR3
FGFR4
actin
B
GBM17
CTRL-NS
TMZ-NS
GBM95
CTRL-NS
IR-NS
90.26% (18.65)
99.74% (146.12)
EGFR
0% (0)
0.66% (0)
97.08% (29.82)
99.16% (63.67)
MET
40.15% (19.33)
97.35% (55.1)
8.89% (12.99)
24.24% (14.48)
PDGFRα
26.45% (15.57)
62.26% (28.76)
21.93% (19.33)
5.35% (16.14)
PDGFRβ
14.73% (20.04)
11.74% (19.33)
15.67% (15.57)
9.13% (15.57)
FGFR2
0% (0)
0.41% (0)
3.72% (14.48)
0.59% (0)
FGFR3
3.81% (20.78)
4.83% (20.78)
1.68% (16.14)
3.54% (16.14)
FGFR4
11.69% (21.54)
7.41% (24.89)
Count
FL 8 Log
C
FC score
0
2
4
6
8
EGFR
MET
PDGFRα
PDGFRβ
FGFR2
FGFR3
FGFR4
GBM17
GBM95
CTRL-NS
TMZ-NS
IR-NS

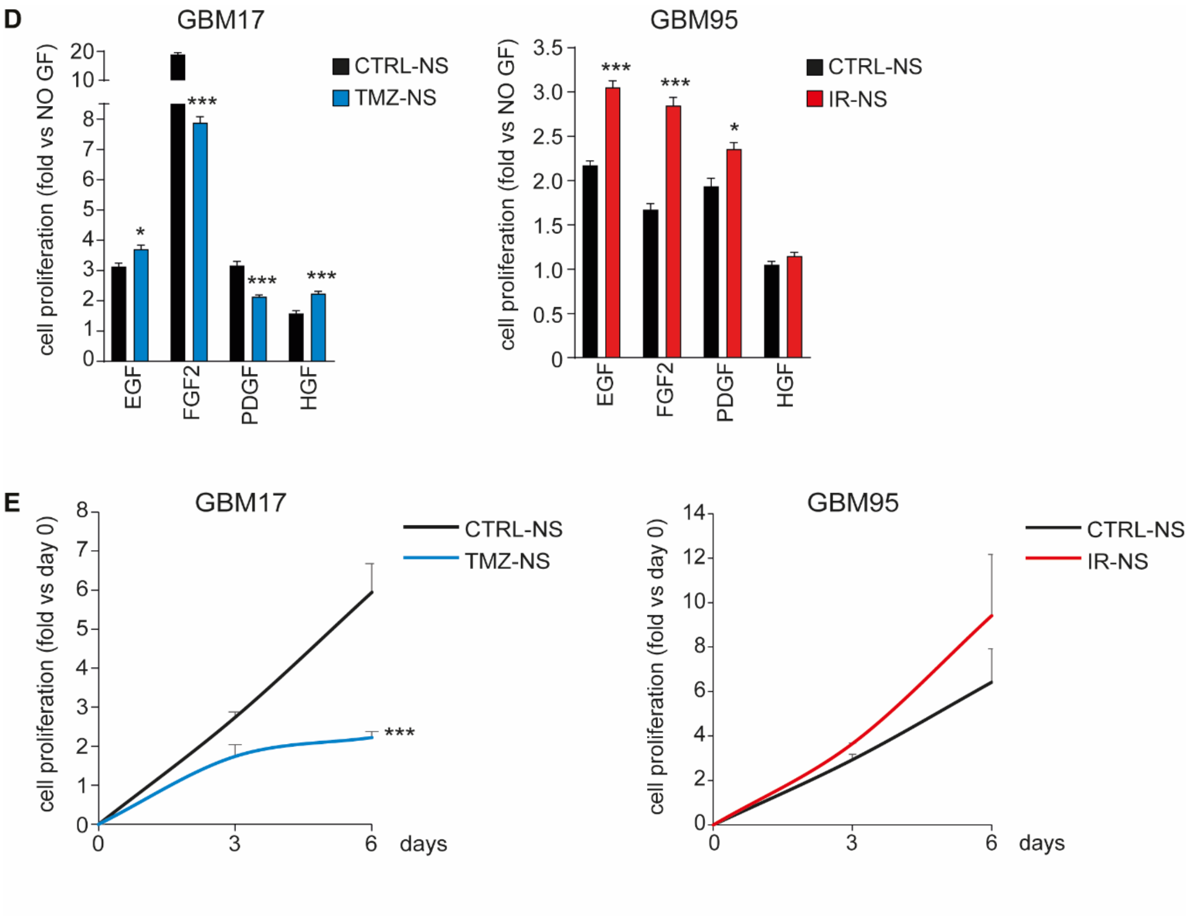

Figure 8. Secondary resistant GSCs display changes in RTK expression

(A) Western blots showing RTKs expression in GBM17 (left) and GBM95 (right) CTRL and matched family members showing secondary resistance. Actin: loading control

(B) Flow cytometry showing RTKs expression GBM17 (left panel) and GBM95 (right panel) CTRL and secondary resistant family members. Percentage of positive cells and mean fluorescent intensity (FI) are reported.

(C) Flow cytometric (FC) score of RTKs expression in GBM17 and GBM95 CTRL and secondary resistant NS.

(D) Cell proliferation of GBM17 (left) and GBM95 (right) CTRL and secondary resistant family members, as measured 6 days after administration of the indicated single GF as indicated. Data are shown as mean ± SEM of a representative experiment. Student's paired t test $*p<0.05$; $**p<0.01$; $***p<0.001$. GBM17, EGF $p=0.025478$; FGF2 $p<0.000001$; PDGF $p=0.000114$; HGF $p=0.00055$. GBM95, EGF $p=0.000006$; FGF2 $p=0.000004$; PDGF $p=0.015068$.

(E) Basal proliferation of GBM17 (left) and GBM95 (right) CTRL and secondary resistant family members, measured in the presence of the standard culture medium (EFPH20) evaluated for 6 days after plating. Data are shown as mean ± SEM of at least two independent experiments. ***Student's paired t test $p= 0.000671$

Therapeutic selection of secondary resistant GSCs is associated with increased refractoriness to apoptosis

Enhanced protection from apoptosis is a hallmark of cancer and a key mechanism of therapeutic resistance [106, 107]. Therefore, we investigated potential increases in anti-apoptotic activity in secondary resistant GSCs.

Key regulators of this pathway belong to the 'BH3 family' of proteins, which include both pro-survival and pro-apoptotic proteins that act at the outer mitochondrial membrane. These proteins contain at least one BCL2-homology (BH) domain, and their balance determines whether apoptosis is restrained or triggered through the release of cytochrome C from the mitochondrial outer membrane [108, 109]. Pro-apoptotic proteins that contain only the BH3 domain are referred to as "BH3-only" and include "sensitizers", which can bind and inhibit pro-survival proteins (such as BCL-2 and its homologs), and "activators", which can also bind and activate pro-apoptotic, pore-forming BAX and BAK proteins. The latter are directly responsible for mitochondrial outer membrane permeabilization (MOMP), a critical step in irreversibly committing the cell to apoptosis.

We could experimentally measure cell propensity to unleash apoptosis, also defined as "apoptotic priming", using a functional assay called "BH3 profiling" [110]. In this assay, cells are supplied with a BIM-BH3 synthetic peptide that mimics the activity of the BIM BH3-only activator. The amount of BIM peptide required to induce cytochrome C release directly reflects cell priming or propensity to apoptosis. Using the BH3 profiling assay, we observed that both secondary resistant TMZ- and IR-NS required significantly more BIM-BH3 peptide to achieve the same level of cell death as CTRL-NS, indicating that secondary resistant NS were significantly more resistant to apoptosis than CTRL-NS (Fig. 9A). Interestingly, the concentrations of the BIM-BH3 peptide required to induce cytochrome C release >50% were significantly different between the two GSC families, with GBM17 requiring a concentration range from 5 to 40 μM, while GBM95 required only 0.05 to 5 μM. This evidence suggested that GBM17 family was inherently more refractory, or less primed, to apoptosis compared to GBM95.

Considering that the increased resistance to BIM-BH3 peptide-induced apoptosis exhibited by secondary resistant NS could be due to decreased expression of pro-apoptotic proteins, we assessed the expression of a comprehensive panel of BH3 family members. This included pro-apoptotic pore-forming proteins (BAX and BAK), BH3-only activators (BIM, BID, PUMA, and BIK) and BH3-only sensitizers (BAD, NOXA and HRK), which were evaluated by qPCR (Figure 9B) and western blot analysis (Figure 9C). Consistent with glioma data from the Human Protein Atlas (proteinatlas.org), CTRL-NS did not express BIK mRNA, and BAX mRNA levels were higher than BAK mRNA (encoded by the BAK1 gene) (Figure 9B). Overall, we did not observe significant differences in mRNA expression of BH3 family members between secondary resistant NS and their matched CTRL-NS, except for NOXA (codified by PMAIP1 gene), which showed a more than 3-fold increase in GBM17 TMZ-NS compared to CTRL-NS. However, this NOXA modulation was not observable at protein level (Figure 9C). Conversely, at protein level, we observed downregulation of pore-forming proteins (BAX in GBM17 TMZ-NS, BAK in GBM95 IR-NS) and a strong reduction in BIM expression in both secondary resistant NS, while the levels of other BH3 proteins were unchanged, consistent with their mRNA.

Since BIM is post-transcriptionally regulated via phosphorylation by ERK, which leads to its ubiquitination and degradation, and ERK is powerfully activated by EGFR, we speculated that BIM downregulation might be caused by EGFR overexpression (described above) and activation by its ligand EGF, in secondary resistant NS. Indeed, EGFR upregulation was inversely correlated with BIM expression in both secondary resistant NS compared to their matched controls (Fig. 9D).

To test this hypothesis, we evaluated BIM expression in NS cultured in their propagation medium and in the presence of the EGFR inhibitor lapatinib, in a time-course experiment. We observed that EGFR inhibition restored BIM expression, reaching its peak 24 hours after the treatment began (Fig. 9E).

Additionally, EGFR inhibition restored BIM expression in GBM17 TMZ-NS to the same level as in its matched CTRL-NS, but complete BIM restoration was not observed in GBM95 IR-NS. In the same experiment, we noted that EGFR inhibition effectively modulated ERK phosphorylation (with an initial upregulation due to rebound effect) but could not reduce it at the same level as in CTRL-NS, likely due to increased activity of RTKs impacting this pathway, as discussed above. However, despite restoring BIM levels, EGFR inhibition alone was insufficient to induce apoptosis, as shown in cell viability experiments (Figure 9F), suggesting that a more complex imbalance of BH3 proteins supports apoptotic resistance of secondary resistant GSCs.

In summary, secondary resistant GSCs displayed increased refractoriness to apoptosis compared to treatment-naïve GSCs, which was associated with downregulation of BH3 family proteins that promote apoptosis, such as pore-forming BAX and BAK and BH3-only activator BIM. Expression of the latter could be restored by EGFR inhibition, but this was insufficient to decrease cell survival.

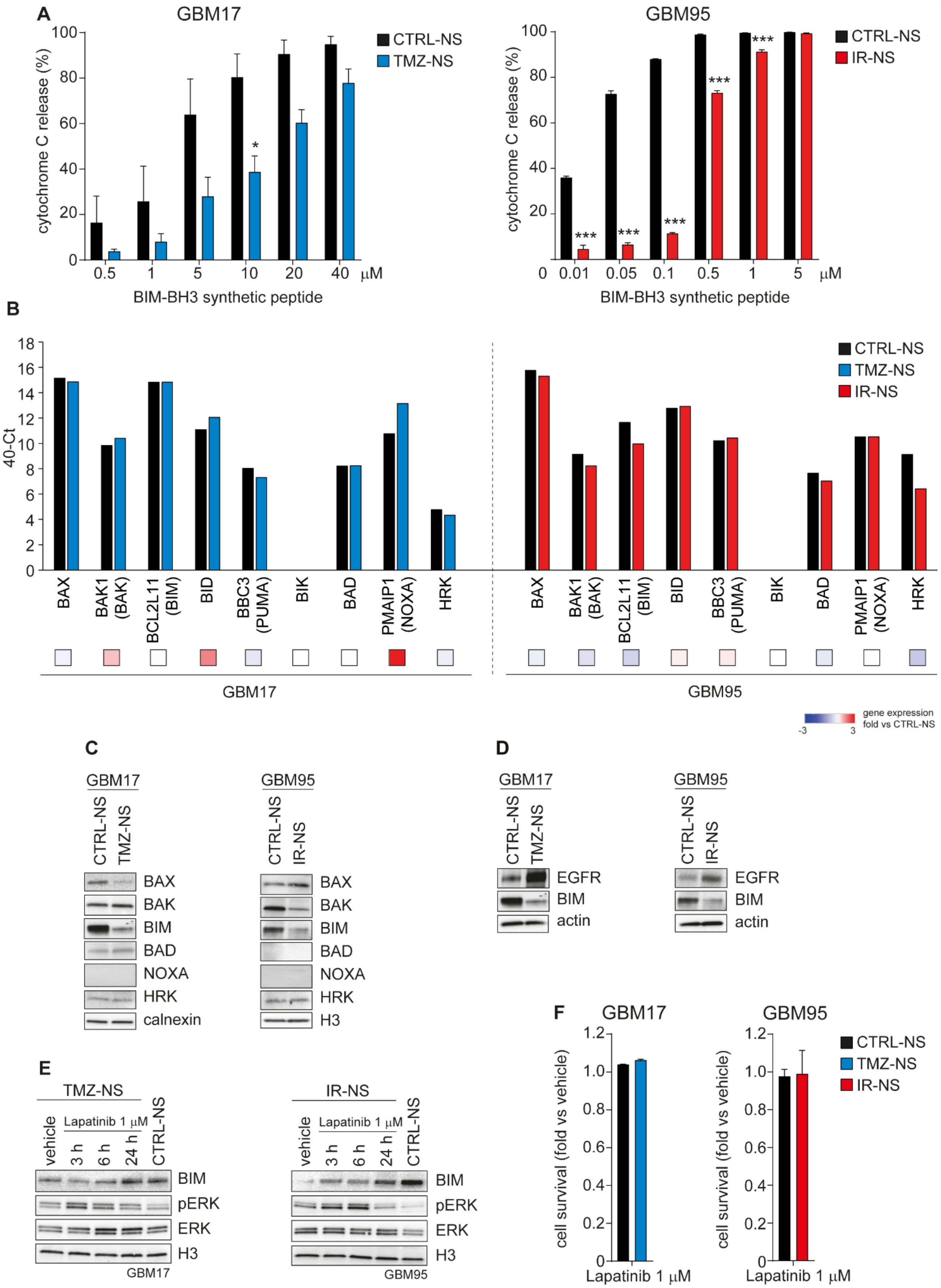
A
GBM17
cytochrome C release (%)
100
80
60
40
20
0
0.5
1
5
10
20
40
μM
*
CTRL-NS
TMZ-NS
BIM-BH3 synthetic peptide
GBM95
0
0.01
0.05
0.1
0.5
1
5
μM
***
CTRL-NS
IR-NS
BIM-BH3 synthetic peptide
B
40-Ct
18
16
14
12
10
8
6
4
2
0
BAX
BAK1 (BAK)
BCL2L11 (BIM)
BID
BBC3 (PUMA)
BIK
BAD
PMAIP1 (NOXA)
HRK
GBM17
GBM95
CTRL-NS
TMZ-NS
IR-NS
-3
3
gene expression fold vs CTRL-NS
C
GBM17
CTRL-NS
TMZ-NS
BAX
BAK
BIM
BAD
NOXA
HRK
calnexin
GBM95
CTRL-NS
IR-NS
BAX
BAK
BIM
BAD
NOXA
HRK
H3
D
GBM17
CTRL-NS
TMZ-NS
EGFR
BIM
actin
GBM95
CTRL-NS
IR-NS
EGFR
BIM
actin
E
TMZ-NS
vehicle
Lapatinib 1 μM
3 h
6 h
24 h
CTRL-NS
BIM
pERK
ERK
H3
GBM17
IR-NS
vehicle
Lapatinib 1 μM
3 h
6 h
24 h
CTRL-NS
BIM
pERK
ERK
H3
GBM95
F
GBM17
cell survival (fold vs vehicle)
1.2
1.0
0.8
0.6
0.4
0.2
0
Lapatinib 1 μM
GBM95
Lapatinib 1 μM
CTRL-NS
TMZ-NS
IR-NS

Figure 9. Therapeutic selection of secondary resistant GSCs is associated with increased refractoriness to apoptosis

(A) BH3 profiling measured as cytochrome C release after exposure to different doses of BIM-synthetic peptide in GBM17 (left) and GBM95 (right) CTRL and matched family members showing secondary resistance. Data are shown as mean ± SEM of at least two independent experiments. Student's paired t test $^*p<0.05$, $^{***}p<0.001$. For GBM17 ANOVA $p<0.05$ (10 μM $p=0.018844$). For GBM95 0.01-0.5 μM $p<0.000001$; 1 μM $p= 0.000008$

(B) Gene expression of pro-apoptotic genes as measured by Real Time PCR in GBM17 and GBM95 CTRL and secondary resistant family members shown as 40-dCT (bars), or 2^(-ddCt) (squares) of secondary resistant vs. CTRL-NS. Brackets: protein name if different from official gene name.

(C) Western blots showing the expression of pro-apoptotic proteins in GBM17 (left) and GBM95 (right) CTRL and secondary resistant family members. Calnexin and H3: loading controls.

(D) Western blots showing the EGFR overexpression and BIM downregulation in in GBM17 (left) and GBM95 (right) CTRL and secondary resistant family members. Actin: loading control.

(E) Western blots showing BIM protein modulation in a time-course experiment with after Lapatinib administration in GBM17 TMZ-NS (left) and GBM95 IR-NS (right). pERK and ERK expressions are also shown. Protein expression in CTRL-NS at basal level is shown. H3: loading control.

(F) Cell survival of GBM17 (left) and GBM95 (right) CTRL and secondary resistant family members 48 hours after Lapatinib administration. Data are shown as mean ± SEM of at least two independent experiments.

Secondary resistant GSCs are sensitive to BH3 mimetics

Refractoriness to apoptosis induction can be explained not only by a deficiency in pro-apoptotic BH3 proteins but also by an excess of pro-survival BH3 proteins. In addition to the BH3 domain, these pro-survival proteins contain all BH domains (BH1-BH4) and can impair apoptosis by binding and sequestering monomeric pore-forming BAK and BAX proteins, as well as BH3-only activators or sensitizers [108].

Therefore, we evaluated the expression of pro-survival BH3 proteins in secondary resistant NS (Figure 10A and 10B). We observed overall low expression of BCL-2 and higher expression of BCL-xL and MCL1 mRNA (encoded by BCL2L1 and MCL1 gene, respectively), with no differences between secondary resistant NS and their matched CTRL-NS (Figure 10A). The prominent expression of BCL-xL and MCL1 over BCL-2 was consistent with glioma data from the Huma Protein Atlas (proteinatlas.org) and previous publications [111]. At the protein level, we detected a modest increase in BCL-xL expression and a slight reduction in MCL1 expression in secondary resistant NS compared to CTRL-NS (Figure 10B), while BCL-2 expression was barely detectable.

Next, we assessed the activity of drugs known as BH3 mimetics, designed to inhibit pro-survival BH3 proteins (namely BCL-2, BCL-xL, and MCL1) by mimicking pro-apoptotic BH3-only proteins, which have shown promising preclinical effects in tumors [108, 112-115]. The BH3 mimetics included ABT-199 (venatoclax), which is quite specific for BCL-2, ABT-263 (navitoclax), which inhibits both BCL-2 and BCL-xL, and other two compounds specific for BCL-xL or MCL1, named, respectively, A-1331852 and S63845 (Figure 10C). When these compounds were supplied at concentrations consistent with those reported in literature [111, 116], we observed significant inhibition of cell survival only with compounds that targeted BCL-xL, either specifically (A-1331852) or together with BCL-2 (ABT-263 or navitoclax). This inhibition of cell survival was more pronounced in GBM95, affecting both CTRL-NS and IR-NS, whereas in GBM17, the BCL-xL-specific compound (A-1331852) was significantly effective only in

TMZ-NS. A-1331852 is particularly interesting because it can cross the blood brain barrier (BBB) [117] and did not cause toxicity in normal human astrocytes (NHA) (Figure 10E) or human neural stem cells (hNS) [111]. Moderate toxicity was observed in human microglia (HMC3) (Figure 10E) and mouse brain slices, which are representative of the overall brain composition [111]. In contrast, ABT-263 can not cross the BBB and, despite its mild toxicity on NHA and microglia (Figure 10E), it has demonstrated systemic toxicity [118].

We then asked whether NS sensitivity to A-1331852 was due to BCL-xL sequestering the vast majority of BIM, thus preventing it from triggering apoptosis. Immunoprecipitation experiments showed that BCL-xL bound the total amount of BIM protein in both secondary resistant cells and most of this protein in the CTRL-NS (Figure 10F). These findings help explain why NS are sensitive to BCL-xL inhibition, and why secondary resistant NS are less primed for apoptosis than CTRL-NS.

Finally, given that EGFR inhibition increases BIM levels (Figure 9E) and the prominent interaction between BIM and BCL-xL (Figure 10F), we decided to combine lapatinib with A-1331852 to assess whether the effective dose of the BCL-xL inhibitor could be reduced. Preliminary dose-response experiments showed that: i) A-1331852 was still effective (cell survival <50% compared to controls) at a concentration 10-fold lower than conventionally used (0.1 µM vs. 1 µM), and ii) lapatinib modestly, although statistically significantly enhanced the inhibitory effect of A-1331852 on cell survival (Figure 10G).

In conclusion, we provided evidence that the emergence of secondary resistance to TMZ and IR, driven by genetic alterations or epigenetic adaptive mechanisms still under investigation, is associated with increased resistance to apoptosis. This may result from an unbalanced ratio between BH3 pro-apoptotic and pro-survival proteins, favoring the latter. In this complex scenario, the anti-apoptotic BCL-XL and the pro-apoptotic activator BIM, which is modulated at protein levels by RTK signaling, appear to play a prominent role (Figure 10H). BH3 mimetics targeting BCL-xL and possibly strategies to restore BIM levels (Figure 10I), should be further evaluated to overcome apoptosis refractoriness in GSCs resistant to conventional therapies.

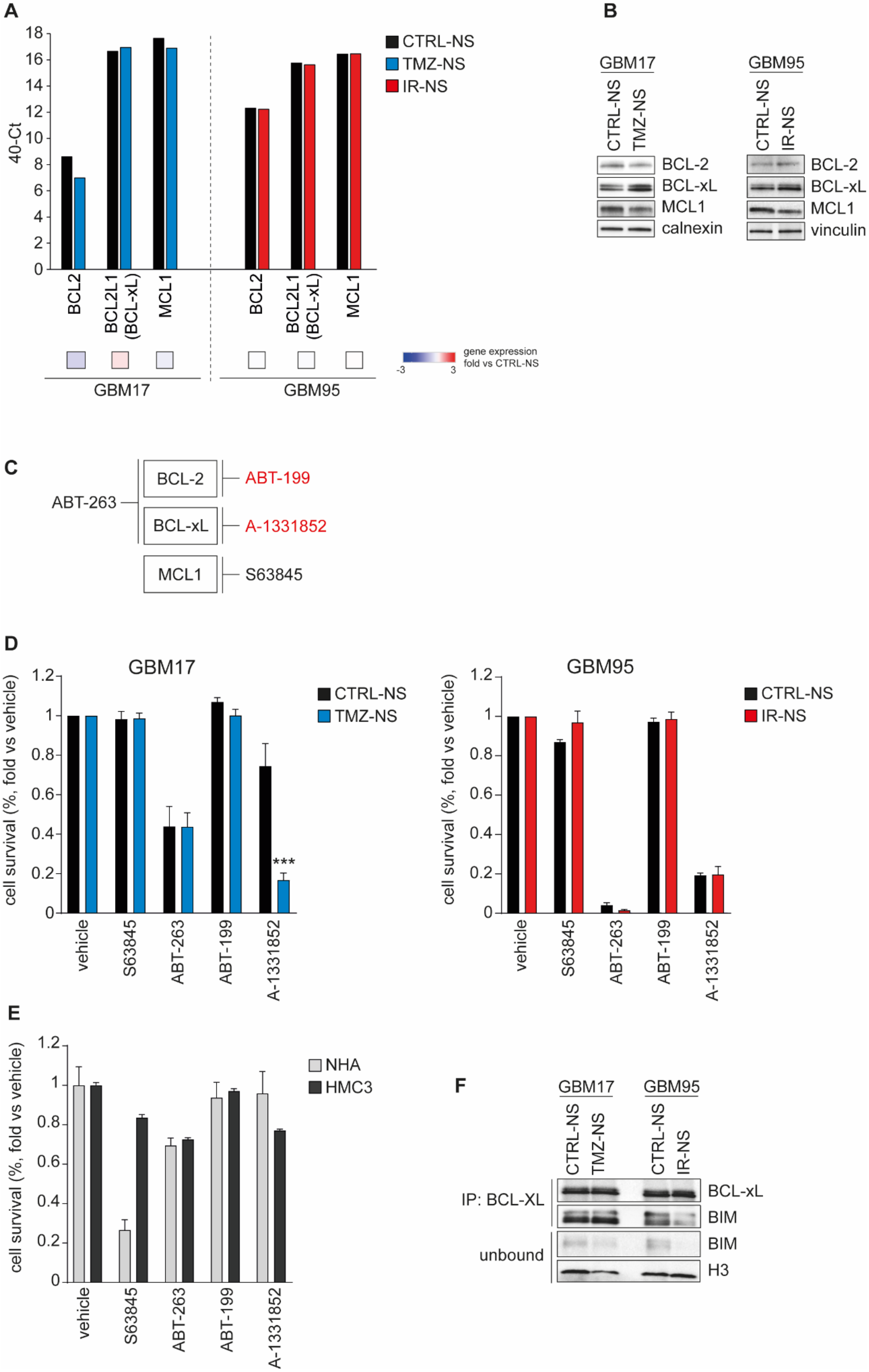
A
18
16
14
12
10
8
6
4
2
0
40-Ct
CTRL-NS
TMZ-NS
IR-NS
BCL2
BCL2L1 (BCL-xL)
MCL1
BCL2
BCL2L1 (BCL-xL)
MCL1
gene expression fold vs CTRL-NS
-3
3
GBM17
GBM95
B
GBM17
CTRL-NS
TMZ-NS
BCL-2
BCL-xL
MCL1
calnexin
GBM95
CTRL-NS
IR-NS
BCL-2
BCL-xL
MCL1
vinculin
C
ABT-263
BCL-2
BCL-xL
MCL1
ABT-199
A-1331852
S63845
D
GBM17
cell survival (%, fold vs vehicle)
1.2
1
0.8
0.6
0.4
0.2
0
CTRL-NS
TMZ-NS
***
vehicle
S63845
ABT-263
ABT-199
A-1331852
GBM95
cell survival (%, fold vs vehicle)
1.2
1
0.8
0.6
0.4
0.2
0
CTRL-NS
IR-NS
vehicle
S63845
ABT-263
ABT-199
A-1331852
E
cell survival (%, fold vs vehicle)
1.2
1
0.8
0.6
0.4
0.2
0
NHA
HMC3
vehicle
S63845
ABT-263
ABT-199
A-1331852
F
GBM17
GBM95
CTRL-NS
TMZ-NS
CTRL-NS
IR-NS
IP: BCL-XL
unbound
BCL-xL
BIM
BIM
H3

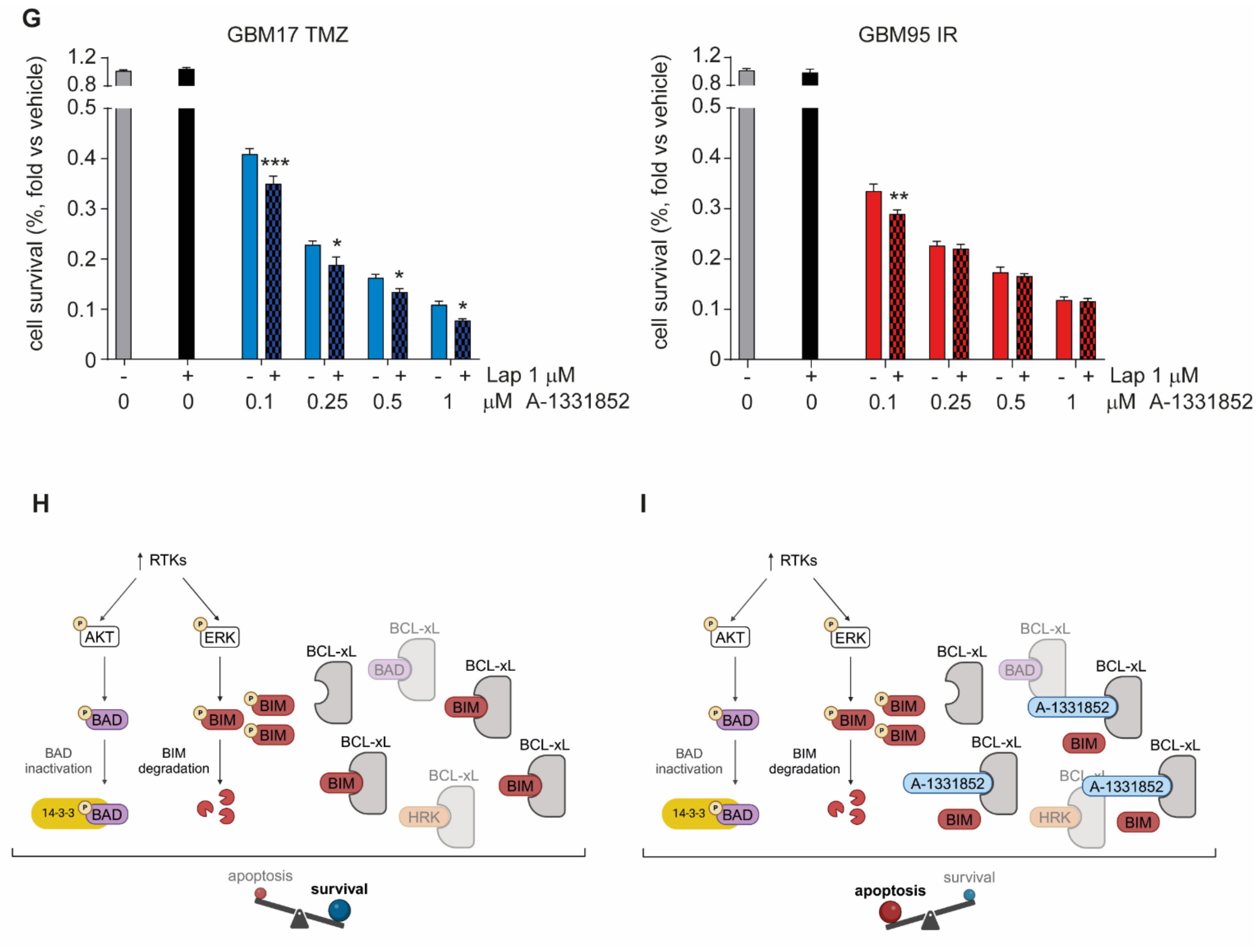

Figure 10. Secondary resistant GSCs are sensitive to BH3 mimetics

(A) Gene expression of pro-survival genes measures by Real Time PCR in GBM17 and GBM95 CTRL and secondary resistant family members shown as 40-dCT (bars), or 2^(-ddCt) (squares) of secondary resistant vs. CTRL-NS. Brackets: protein name if different from official gene name.

(B) Western blots showing the expression of pro-survival proteins in GBM17 (left) and GBM95 (right) CTRL and secondary resistant family members. Calnexin and vinculin: loading controls.

(C) Schematic representation of the panel of the molecular targets of BH3 mimetics chosen to be tested. Red: molecules demonstrated to be able to cross blood brain barrier.

(D) Cell survival of GBM17 (left) and GBM95 (right) CTRL and secondary resistant family members 48 hours after administration of indicated BH3 mimetics. Data are shown as mean ± SEM of at least two independent experiments. ***Student's paired t test p= 0.000004

(E) Cell survival of NHA and HMC3 after treatment with indicated BH3 mimetics, measured 48 hours after administration of indicated BH3 mimetics. Data are shown as mean ± SEM of a representative experiment.

(F) Evaluation of BIM protein bound with BCL-xL, measured by immunoprecipitation in GBM17 and GBM95 CTRL and secondary resistant family members. H3: loading control for unbound.

(G) Cell survival of GBM17 TMZ (left) and GBM95 IR (right), measured 48 hours after administration of increasing doses of lapatinib in combination with A-1331852 or not. Data are shown as mean ± SEM of a representative experiment. Student's paired t test *$p<0.05$; **$p<0.01$; ***$p<0.001$. GBM17 TMZ (Lapatinib vs combo): 0.1 μM $p= 0.000311$; 0.25 μM $p= 0.014743$; 0.5 μM $p= 0.046305$; 1 μM $p= 0.046305$. GBM95 IR (Lapatinib vs combo) 0.1 μM $p= 0.001420$.

(H) Schematic representation of the mechanisms of regulation of BIM by EGFR pathway and BCL-xL interaction, showing its pro-survival effect. Created with BioRender.com

(I) Schematic representation of the changes in BCL-xL interactions after A-1331852 treatment, and its pro apoptotic effect. Created with BioRender.com

DISCUSSION

Over the past decade, an increasing number of studies have addressed the critical issue of therapeutic resistance and recurrence in glioblastoma (GBM). Unfortunately, despite these efforts, little progress has been made in translating promising new drugs or repurposed therapies from preclinical research into improved clinical outcomes for GBM patients [119, 120]. This limited success is partly due to the lack of preclinical models that can be experimentally manipulated and that accurately represent both intra- and inter-tumoral heterogeneity at the GSC level. To address this gap, we developed an innovative *ex vivo* derivation protocol to generate resistant GSC (res-GSC) families that ideally represent matched GSCs from both de novo and recurrent GBMs. This model of GBM recurrence is robust because:

i) The use of a surgical aspirator (conventional or ultrasonic) enables collection of the entire GBM tumor population, preserving intratumoral heterogeneity [74, 121].

ii) Cells are cultured in a medium enriched with growth factors (EGF, FGF2, PDGF and HGF) reflective of the brain and tumor microenvironment. These factors concur to support the stem phenotype and to preserve heterogeneity, as their receptors are known to be expressed in a mutually exclusive manner in GBM cells [66, 74, 122]; this represent a crucial improvement over current GSC models, typically cultured in a medium containing EGF and FGF2 only.

iii) Treatment is administered shortly after GBM processing, before culture selection can reduce the original cell heterogeneity, and at a stage where cells remain as single elements (rather than forming aggregates or neurospheres), allowing for uniform treatment exposure and penetration. This timing represents a key innovation, as previous studies primarily relied on established cultures of cells (both primary and cell lines) where genetic and phenotypic landscapes had already been selected and stabilized by the culture conditions.

iv) Therapeutic treatment is administered using clinically relevant doses of temozolomide (TMZ) or ionizing radiation (IR) [3, 60, 85], effectively simulating patient treatment conditions.

Notably, we administered TMZ and IR in two parallel settings to dissect the distinct, or potentially shared, mechanisms driving chemo- and radioresistance. Interestingly, across our cohort of res-GSC families, we did not derive any res-GSC families without the control, untreated neurospheres (CTRL-NS), which challenges the hypothesis that therapeutic selection could improve GSC derivation efficiency.

The tumor cohort from which we derived the res-GSC families, although still limited in number, appears representative of GBM intertumoral heterogeneity. This cohort displayed genetic alteration frequencies consistent with those found in the TCGA dataset [17]. The presence of EGFR and TP53 alterations in the original GBMs were confirmed to respectively hinder or promote GSC derivation in vitro, regardless of therapeutic pressure, consistent with our earlier work on GSC isolation under different growth factor conditions [74]. EGFR amplification, typically extrachromosomal, is known to hinder neurosphere proliferation and, if retained, usually undergoes a reduction in copy number [74, 86, 122]. However, EGFR amplification - likely due to the plasticity of non-mendelian inheritance of extrachromosomal material - can remain restrained and undetectable in culture but become evident after in vivo neurosphere transplantation [123]. Conversely, we found a significant enrichment in PTEN loss-of function alterations (biallelic inactivation) among the GBMs that yielded res-GSC families compared to those that did not. This finding aligns with PTEN role in cell survival and therapeutic resistance [87-90], suggesting that PTEN loss may serve as a biomarker of resistance to conventional treatment.

Our cohort, though small, is also representative of the MGMT status of GBM patients, who display MGMT promoter methylation in about 50% of cases [6]. MGMT promoter methylation is widely accepted in the clinic as a surrogate marker for MGMT expression. However, as promoter methylation and protein expression do not always fully align, the optimal method to determine MGMT status in patients remains debated [6, 91]. In our cohort, MGMT promoter methylation in GBMs and their matched res-GSC family members fully correlates, suggesting the epigenetic inheritance of MGMT status during neurosphere derivation. Importantly, MGMT promoter methylation correlated well with a lack of MGMT protein expression, and *vice versa*, in GSCs.

Consistent with the established role of MGMT expression in promoting TMZ resistance [4, 93], we demonstrated that res-GSC families expressing MGMT protein exhibited primary resistance to TMZ, as seen in CTRL-NS, which reflects the primary resistance of the untreated original GBM population. This primary resistance was evident at the clinically relevant concentration of 50 μM [85]. In contrast, MGMT-negative CTRL-NS were sensitive to this TMZ dose. Interestingly, most of these MGMT-negative NS were partially resistant to 5 μM, the average concentration of TMZ found in patient CSF, which may represent the actual concentration reached in the CNS [85]. This finding supports the possibility that growth factor-enriched culture media may provide a protective role against TMZ, as previously suggested [93]. Therefore, *in vitro* studies conducted in conventional media might underestimate the critical role of growth factors in modulating the response to TMZ *in vivo*. Further investigation into the role of growth factors in supporting cell survival after TMZ (and IR) treatment is required.

As expected, the absence of MGMT expression hindered GSC derivation in the presence of TMZ, resulting in the derivation of TMZ-NS in only half of MGMT-negative cases, and with longer latency periods compared to NS derived without therapeutic pressure. Notably, in 2 out of 3 cases (GBM17 and GBM151), these TMZ-NS exhibited secondary resistance to TMZ while continuing to lack MGMT expression. This led us to investigate alternative mechanisms of TMZ resistance, possibly related to genetic alterations in DNA repair mechanisms.

Indeed, secondary resistant TMZ-NS showed unique inactivating mutations in mismatch repair (MMR) genes, whose role in TMZ resistance is well established [4, 33, 93]. These alterations appeared to result directly from the mutagenic activity of TMZ rather than being selected from the original GBM cell population, as high-sensitivity detection techniques (ddPCR) failed to identify MMR mutations in the original GBM, and the mutation type (C>T) corresponded to that induced by TMZ. Further WES analysis will be needed to determine whether these secondary resistant GSCs exhibit the overall signature of TMZ mutagenic activity [95]. Importantly, the MMR mutations found in TMZ-NS had a functional impact, leading to a significant reduction, up to the complete abrogation, of MMR activity in secondary resistant TMZ-NS.

Regarding the driver gene mutations, TMZ-NS with secondary resistance largely retained those detected in the original GBM, consistent with observations in recurrent GBM tissues [36, 37, 82] and the notion that the major genetic drivers are generally shared by the entire GBM cell population at diagnosis, rather than confined to subclones [37].

Notably, the acquisition of MMR deficiency, with possible ensuing microsatellite instability (MSI), could offer opportunities for therapeutic intervention, since the MSI phenotype has been shown to confer sensitivity to WRN helicase inhibitors, as demonstrated in colorectal cancer [124]. Moreover, novel drugs that effectively target MGMT-neg GBM cells regardless of MMR status are currently in the pre-clinical stage [125]. Unfortunately, the generation of neoantigens associated with MMR deficiency, which enhances sensitivity to immunotherapy in several tumor types, holds limited promise for GBM due to the poor penetration of adaptive immunity into CNS [10]

MMR abrogation might not be the only genetic mechanism of TMZ resistance. Interestingly, a recent study has shown that secondary TMZ-resistant cells that remain MGMT-neg and MMR-proficient display increased activity of the homologous recombination (HR) and the microhomology-mediated end-joining (MMEJ) pathways, suggesting specific dependencies in these cells that warrant further investigation [126]. Derivation of additional GSC families will be needed to expand the number of models available to investigate such mechanism of TMZ resistance.

From MGMT-neg GBMs, we also derived a TMZ-NS (GBM149) that, despite rapid establishment upon selective pressure, did not acquire secondary resistance, i.e. it remained highly sensitive to TMZ treatment and, consistently, MGMT-negative, and devoid of MMR mutations. To explain these features, the hypothesis that a subgroup of GBM drug-tolerant persister cells may exhibit a plastic and transient MGMT expression during selective TMZ treatment is currently under investigation. In addition, it would be worthwhile to explore the involvement of BRAF mutation (present in the original GBM and counterselected by TMZ treatment), which is known to correlate with better prognosis in GBM [94]. Moreover, since patients with BRAF mutations are amenable to targeted therapy with BRAF and MEK inhibitors [127], the findings concerning increased sensitivity to standard treatments and concomitant loss of BRAF mutations could have implications for the appropriate sequence of treatment administration.

All MGMT-neg TMZ-NS, including the one that did not display secondary resistance, displayed a significant increase in chromosomal aberrations, likely due to the TMZ genotoxic effects. These chromosomal aberrations, consistent with findings in recurrent GBM tissues [36], could lead to the generation of clinically relevant fusion transcripts such as FGFR3-TACCs3 [128, 129] or PTPRZ-MET [130]. The presence of these and other fusion transcripts is currently under investigation.

Consistent with the inherent radioresistance of GSCs, reported to associate with a constitutive activation of the DNA damage response (DDR) [58, 60, 131], more than half of our res-GSC families displayed primary radioresistance. In one family (GBM95), we observed the emergence of a secondary radioresistant IR-NS. The latter detected DNA damage from IR exposure more efficiently than its matched CTRL-NS, as indicated by stronger upregulation of RAD51 protein and by a faster detection and resolution of γH2AX (i.e. phospho-H2AX) foci. Remarkably, no new specific genetic alterations were identified in this IR-NS, compared to its matched CTRL-NS and the original GBM, suggesting that the observed secondary radioresistance may rely on adaptive mechanisms. Additionally, in IR-NS we observed a reduction in ploidy, a phenomenon also reported in recurrent tumors such as esophageal adenocarcinomas [132], which reflects karyotype adaptation to the therapeutic selective pressure.

RAD51 plays an important role in the HR pathway, and its overexpression in secondary resistant IR-NS is consistent with the observation that RAD51 mRNA expression is significantly upregulated in GBM recurrences compared to primary tumors, as observed in the TCGA dataset [133]. This suggests that recurrences may increase baseline RAD51 transcription, leading to further transcriptional induction and/or increased protein translation upon subsequent IR exposure.

The formation of γH2AX foci is a marker of DNA double strand breaks, which disappears soon after the damage is repaired. Immediately following double-strand break formation, the H2AX histone is phosphorylated by serine-threonine kinases such as ATM, ATR and DNA-PK, and contributes to ATM localization and activation at the DNA damage site, supporting a positive-feedback loop [134] that enhances RAD51 recruitment to single-strand DNA, a key step for HR activation. Previous evidence linking RTK signaling, particularly MET signaling, to ATM activation and increased RAD51 expression [60] encourages further investigation into the role of RTKs in the acquisition of adaptive secondary radioresistance, as well as exploration of RTK inhibition to prevent or counteract established secondary radioresistance. Overall, our models provide an opportunity to functionally assess inhibitors targeting the HR proficiency associated with secondary radioresistance, among which ATM inhibitors [126, 135].

With the emergence of secondary resistance to both TMZ and IR, we observed an increase in stem-like features both *in vitro* and *in vivo,* consistent with reports in GBM recurrences [34, 83, 102]. We also found a significant increase in the expression of RTKs, particularly MET/HGFR and EGFR, known to promote cell survival and therapeutic resistance, for instance, by activating ATM, as discussed above [41, 122, 136].

The role of MET in radioresistance has been extensively investigated by our group and others [60, 137, 138] and its overexpression in recurrences has been documented in our previous studies [60] and the

TCGA cohort (source: GlioVis). MET expression is also significantly associated with the GBM mesenchymal phenotype [16, 139], toward which recurrences are reported to shift, influenced by immune microenvironment signaling [33, 78, 80, 140]. Although we could not confirm a shift toward a mesenchymal profile associated with resistance onset in res-GSC families, possibly due to the absence of the microenvironment, the increased expression of receptors like MET in secondary resistant GSCs may indicate an inherent propensity to trigger mesenchymal programs under appropriate microenvironmental conditions.

Regarding EGFR, while it has been implicated in both chemo- and radio-resistance [59, 141], its involvement in recurrences remains debated, with reports showing both increased [142] and decreased [82] EGFR pathway activity. However, in our models of secondary resistance, we observed that EGFR may play a significant role in supporting an anti-apoptotic phenotype, as detailed below.

In addition to RTKs expression, another hallmark of therapeutic resistance is the evasion of apoptosis [136], which occurs when the balance between prosurvival and proapoptotic BH3 family (also known as BCL-2 family) proteins is tipped in favor of prosurvival [108, 115]. This balance determines the so-called apoptotic priming, i.e., the tendency of cells to initiate apoptosis in response to given amounts of apoptotic stimuli, as measured by an assay known as ‘BH3 profiling’. Consistent with the apoptotic refractoriness of adult brain [143], our res-GSC families were poorly primed for apoptosis, with secondary resistant NS even less primed for apoptosis than their matched CTRL-NS, suggesting that an imbalance of BH3 family proteins in favor or survival could be involved in secondary resistance.

In secondary resistant NS, we observed a downregulation of the proapoptotic protein BIM, associated with increased EGFR expression. Consistent with the established role of EGFR in promoting BIM degradation [116, 144], EGFR inhibition in secondary resistant NS restored BIM expression, though without significantly reducing cell survival.

By targeting the prosurvival BH3 proteins with a panel of drugs known as BH3 mimetics [112-115], we found that secondary resistant NS were sensitive to ABT-263 (or navitoclax) and A-1331852, which are, respectively, a pan-BCL-2 inhibitor (targeting multiple prosurvival BH3 proteins) and a specific BCL-xL inhibitor. The observation that BCL-xL sequesters all BIM protein in resistant NS helps explaining why these cells rely on BCL-xL activity to survive. Sensitivity to BCL-xL inhibitors has previously been linked to the expression of the proapoptotic protein NOXA [145, 146]. Accordingly, we observed sensitivity to BCL-xL inhibitors in all NS expressing NOXA, including not only the secondary resistant GBM17 TMZ-NS and GBM95 IR-NS, but also the GBM95 CTRL-NS.

Since A-1331852 can cross the blood brain barrier [117] and has shown negligible toxicity in major brain cell types, as evidenced by our study and others [111], it appears a promising drug for further preclinical assessment.

Given the association between EGFR and the apoptotic pathway, we tested whether combining lapatinib and A-1331852 could produce a synergistic effect in secondary resistant cells, as suggested by the literature [147]. However, we observed only a mild additive effect. This result could be explained by the fact that the BIM increase achieved by EGFR inhibition was still efficiently buffered by residual free BCL-xL. Since other RTKs could contribute to a BH3 proteins unbalance toward pro-survival, particularly by inducing BIM degradation through the MAP kinase pathway, MEK inhibitors (such as trametinib) or a broad-specificity tyrosine kinase inhibitor such as regorafenib [148]) could be evaluated to intercept multiple RTK activity and synergize with BH3 mimetics.

In summary, we developed an *ex-vivo* protocol that enables the selection of GSC cultures reliably representing matched primary and recurrent GBMs. These models can be manipulated to investigate and target primary and secondary mechanisms of therapeutic resistance, such as MMR deficiency or the imbalance of BH3 proteins, possibly linked to RTK increased activity. In its current form, this model has certain limitations, such as the lack of a tumor microenvironment, which may provide essential crosstalks for therapeutic adaptation. These limitations could be at least in part circumvented by upgrading the neurosphere model with a more complex 3D microenvironment, including glial, neural and immune components in an organ-on-chip setting, or by co-culturing into brain slices [149, 150]. Lastly, it would be pivotal to validate key findings of this work in the resistant GSCs emerged after treatment, by comparing the pairs of GSCs from matched primary and recurrent tumors that have been derived in the past by our team [34] and other collaborators, and which are currently under selection.

MATERIALS AND METHODS

Neurosphere (NS) derivation

Res-GSC family members were derived from primary GBMs provided by the A.O.U. Città della Salute e della Scienza di Torino, according to the ethical requirements of the institutional committee on human experimentation. Informed consent was obtained from all individual participants included in the study. Res-GSC family members were derived starting from primary GBMs, surgically removed by using ultrasonic or conventional aspirator, and processed to single cell suspension according to a previously published protocol [75]. Briefly, aspirator's content was collected in 50 mL conical tubes, centrifuged RT 10 min at 270 g, and red blood cells were lysed by treatment with ACK for 15 min. The pellet was incubated with collagenase type 1 (Thermo Fisher) at 37°C for 20 min, mechanically dissociated by up and down pipetting with a sterile 18G needle in a 1 mL syringe and subjected to sequential 100 mm and 70 mm filtrations. Cellular suspension (containing cancer cells, normal endothelial and peritumoral cells, and blood white cells) was equally distributed in three 75 cm^2 flasks in Dulbecco's modified Eagle's medium/F-12 (Thermo Fisher) with the addition of 2 mM glutamine (Sigma), antibiotic and mycotic solution (1:100, Sigma), B-27 plus (1:50, Thermo Fisher), human recombinant epidermal growth factor (EGF), basic fibroblast growth factor (FGF2), hepatocyte growth factor (HGF) and platelet-derived growth factor (PDGFB) at 20 ng/ml each (Peprotech). After a short period in culture allowing cell recovery, one flask was treated with temozolomide (TMZ, Sigma) at 50 μM every three days for three times, another flask was irradiated at 2 Gy dose for five consecutive days by using a 200-kV X-ray blood irradiator (Gilardoni, Lecco, Italy), operating RT, with a 1 Gy/ minute dose rate; the third flask remained untreated. Flasks were maintained in normoxic condition (20% O2, 5% CO2) at 37°C. A simplified scheme of derivation procedure is provided in Figure 1D. Part of the same cellular suspension was collected for DNA and RNA analysis. Cell cultures were monitored daily (and cell culture media were refreshed) until NS appearance. Newly formed NSs were propagated at clonal density in derivation medium, were considered stabilized after around 10 passages, and were used as described below.

For genetic comparison with the GBM genetic landscape, the TCGA cohort data obtained from GlioVis was used [133].

Conventional cell lines

Human cell lines representative of normal astrocytes (NHA, Lonza Bioscience) and microglia (HMC3, ATCC) used for evaluation of drug toxicity were kept in culture according to manufacturer's instructions.

Mice and experimental tumors

Animal studies were performed according to ethical regulations and protocols approved by the Italian Ministry of Health (Authorization N. 223/2015-PR). Mice (4–5-week-old female NOD-SCID mice, Charles River Laboratories) were housed at a maximum of 6 per cage with a 12 h light/dark cycle at 22°C and were monitored at a minimum of twice weekly for general performance status. Subcutaneous injection of 2×10^5 cells in a total volume of 200 µL v/v with matrigel was performed on 5 mice for group. Mice were monitored and sacrificed at the appearance of evident suffering signs. Tumor take was established at the appearance of a palpable tumor mass.

Nucleic acid extraction

Genomic DNA (gDNA) was extracted from whole GBM cell suspensions and NS cultures using the ReliaPrep™ gDNA Tissue Miniprep System (Promega) according to manufacturer's protocol. Total RNA was extracted from NS using Maxwell® RSC miRNA tissue kit (Promega) according to manufacturer's instructions. Concentrations and purity of nucleic acid were assessed spectrophotometrically using A260/A280 absorbance ratios with Nanodrop ND1000 (Thermo Fisher). When appropriate, nucleic acid concentration was also evaluated using the proper Qubit assay (Thermo Fisher).

Gene copy number evaluation

Gene copy number (CN) analysis was assessed by real-time PCR, using TaqMan Universal PCR Master MIX and the ABI PRISM 7900HT sequence detection system (Thermo Fisher). Primers and probes for TaqMan CN assays are reported in the Methods Table. Relative gene CN data were calculated by normalizing against two (?) endogenous controls (RNaseP or APOA1 and GREB1). Normal diploid human gDNA (from PBMCs) was used as calibrator to obtain the ΔΔCt. The CN of each gene was calculated with the formula $2\times2^{-\Delta\Delta Ct}$. To discriminate between real EGFR amplification and chr7 polysomy, the calculated CN was normalized vs. CN of an usually not amplified reference gene mapped on chr7 (HGF).

Genes alterations were defined as follow:

- EGFR amplification was defined when CN was > 3 + HGF CN;
- other genes, amplification was defined when CN was > 5;
- CN gain was defined for CN among 3 and 5;
- heterozygous deletion was defined when CN is < 1.5;
- homozygous deletion was defined when CN < 1 in tumor tissues, while corresponded to the absence of target gene PCR product in the presence of control gene PCR product in growing cells.

Droplet digital PCR (ddPCR)

To detect MSH2 and MSH6 VAF, ddPCR was performed using probe–based assays with ddPCR Supermix for Probes (no dUTP) (Biorad), according to manufacturer's instructions.

TERT analysis was performed according to Corless et al.[151]. Droplets were generated using AutoDG Droplet Digital PCR System (Biorad) and analyzed on a QX200 Droplet Digital PCR System using QX Manager Software Standard Edition, Version 1.2 (Biorad). ddPCR assays are reported in the Methods Table.

NGS target panel analysis

After evaluation of DNA integrity by electrophoresis using 1% agarose gel, library preparation was performed starting from 400 ng of DNA, firstly fragmented by using the M220 Focused-ultrasonicator (Covaris), followed by a clean-up step with an optimized ratio volume of AMPure XP beads (Beckman Coulter). Subsequent end-repair step and dA-tailing reaction of blunt-ended DNA fragments was performed by means of NxSeq AmpFREE Low DNA Library Kit (Lucigen) with small adjustments to increase the efficiency of the reactions. Adaptor ligation step has been performed with the same Lucigen's kit, by using xGen Stubby Adapter (IDT) as adaptors. After clean-up step with AMPureXP beads (Beckman Coulter), samples have been amplified (KAPA HiFi HotStart ReadyMix PCR Kit, Roche) concomitantly introducing unique sample barcodes (xGen Stubby Adapter-UDI Primers, IDT). Before target enrichment, QC of post-PCR libraries were checked by means of Qubit dsDNA BR Assay kit (Thermo Fisher Scientific) and of 2100 Bioanalyzer with a High-Sensitivity DNA assay kit (Agilent Technologies). The target of interest for GBM-custom panel design has been defined starting from the identification of genes relevant for tumorigenesis, evolution and emergence of drug resistance in GBM, thus including all coding regions of 75 genes, which are enlisted in Table 5. In detail, the GBM-custom panel covers 232,760 bases with 2,570 designed probes (CUSTOM IDT xGen Custom Hyb Panel-Accel, IDT). Equal amounts of post-PCR libraries (750 ng) were pooled, for a maximum of 8 samples per pool, and subjected to the GBM-panel target enrichment with xGen Hybridization and Wash Kit (IDT plus xGen Universal Blockers - TS Mix (IDT) following manufacturer instruction, except for the choice to perform over-night hybridization to increase the on-target capture. A further amplification of the libraries has been performed with KAPA HiFi HotStart ReadyMix PCR Kit (Roche) and xGen Library Amplification Primer Mix (IDT), thus reaching the needed number of final libraries. Final libraries were quantified by means of Qubit dsDNA HS Assay Kit (Thermo Fisher) and their fragment distribution evaluated using High-Sensitivity DNA assay kit (Agilent Technologies). Equal molar amounts of DNA libraries were pooled and, based on the total number of samples ready to be analyzed, sequenced using Illumina MiSeq or NextSeq500 sequencer (Illumina). Data analysis was performed using a bioinformatic pipeline previously described [152, 153]. A metanormal was built from fastQ files obtained by 10 PBMC samples sequenced using the same laboratory procedures. Alignments from metanormal and whole GBM cell population samples were compared to identify mutations/indels in tumor and metanormal sample. Somatic alterations were present only in tumor while germline ones were common to both samples. NGS artifacts were further filtered following the methods previously described [153, 154]. Then only variants with 5% significance level obtained with a Fisher’s exact test, supported by a minimum of 4 mutated reads in regions with 53 minimum depth and with allele frequency >2.5% were considered. Indels were called using Pindel tool in both alignments and only somatic indels with fractional abundance >10% were reported. Gene CN variations analysis was performed in the matched samples (Tumor vs. Metanormal) for each patient as previously reported [153, 154].

Table 5. Genes included in GBM-target panel

GBM-target panel				
ACVR1	ERBB2	MDM2	NOTCH1	POLD3
AKT1	ERBB3	MDM4	NTRK1	POLD4
AKT2	ERBB4	MET	NTRK2	POLE
AKT3	EXO1	MGMT	NTRK3	POLG
ATRX	EXO5	MLH1	PCNA	PTEN
BRAF	FGFR1	MLH3	PDGFRA	RB1
CDK4	FGFR2	MSH2	PIK3CA	RFC1
CDK6	FGFR3	MSH3	PIK3CB	RFC2
CDKN2A	FGFR4	MSH4	PIK3R1	RFC3
CDKN2B	FUBP1	MSH5	PIK3R3	RFC4
CIC	H3F3A	MSH6	PIK3R4	RFC5
DAXX	HIST1H3B	MYC	PMS1	SMARCA4
DNMT3A	IDH1	MYCN	PMS2	SMARCB1
EBF3	IDH2	NF1	POLD1	TERT
EGFR	IRS1	NF2	POLD2	TP53

EGFRvIII analysis

mRNA from whole GBM cell populations have been analyzed for the expression of EGFRvIII splice variant. mRNA was retro-transcribed using high-capacity cDNA reverse transcription kit (Thermo Fisher) following manufacturer’s instruction. Three primer pairs were designed: 1 specific for wild type EGFR, to be used as reaction control, and the other two for EGFR-vIII (see Methods Table) to be used in three independent PCR reactions. PCR conditions were as follow: initial denaturation 93°C for 3’; 40 cycles 93°C for 15’’, 60°C for 30’’, 72°C for 30’’; final extension 72°C for 3’. PCR products were evaluated on a 2% agarose gel.

MGMT promoter methylation analysis

The evaluation of MGMT promoter methylation in tumor biopsies (formalin-fixed paraffin-embedded samples, FFPE) was performed by pyrosequencing assay. Approximately 200-500 ng total DNA was subjected to bisulfite conversion and pyrosequencing analysis using the MGMT plus kit (Diatech Pharmacogenetics, Italy) and the PyroMark Q96 ID system (Qiagen, Valencia, CA, USA). The pyrosequencing assay was performed as described earlier [155]. The primers used for amplification of bisulphite-treated DNA were forward: 5′-gGGATAGTTGGGATAGTT-3′ (the first g avoids formation of hairpin loops) and reverse: 5′-biotin-ATTTGGTGAGTGTTTGGG-3′ giving a 99-bp amplicon at genomic position 131 155 467–131 155 565. The PCR analysis was performed in duplicate in 25 µl reaction volume, containing 300 pmol each forward and reverse primer, 2 µl 10 × buffer, 160 µM dNTPs, 0.5 U HotStar Taq polymerase (Qiagen) and 1–2 µl bisulfite-treated DNA. The PCR conditions were as follows: 95°C-15 min; 40 cycles of 94°C-30 s, 50°C-45 s, 72°C-30 s; 72°C-10 min (Dyad, GRI, Braintree, UK). To confirm the correct product before pyrosequencing, 3 µl of PCR products were analyzed on a 2% agarose gel, the remaining 22 µl was subjected to pyrosequencing on a PSQ96MA System (Biotage, Uppsala, Sweden) using the primer 5′-GGATATGTTGGGATAGT-3′and PyroGold reagents (Biotage). The Pyro Q-CpG software 1.0.9 (Biotage) was used to analyze data.

Pyrosequencing yields data for 10 CpG sites within the MGMT promoter. For data analysis, the percentage methylation obtained for each CpG was averaged across the 10 CpGs in duplicate PCR reactions (average methylation per sample). For comparisons with clinical data, glioblastomas were considered methylated if they had at least one sample with average methylation ⩾9% (⩾mean±2 s.d. for non-neoplastic brain) in more than one independent bisulphite modification. Unmethylated cases had average methylation <9% in all samples. The average methylation per case was calculated by averaging the average methylation per sample for methylated samples for that case. Methylation-specific PCR assays were carried out as described by Hegi et al.[156]. According to Dunn et al.[157], GBMs were considered methylated (high met) if they had an average methylation >30% or unmethylated (unmet) if >9% Average methylation ranging between 10% and 19% was considered as low and between 20% and 29% as intermediate (int met). Unmet and low are clinically considered unmethylated, int and high as methylated.

The evaluation of MGMT promoter methylation in whole GBM cell suspensions and established NS was performed using ddPCR after DNA treatment with bisulfite. For our analysis, bisulfite conversion was done following the EZ DNA Methylation Gold kit (Zymo Research) protocol. To discriminate methylated cytosines from non-methylated ones, sodium bisulfite (HSO3-) from CT Conversion Reagent was added to the DNA samples. Following incubation at high temperatures, unmethylated cytosines will be converted into sulfonated cytosines and sulfonated uracils through the deamination process. The last step involves the definitive transformation of cytosines into uracil. DNA samples were finally eluted from the columns with the Elution Buffer. All the unmethylated cytosines will be converted with bisulfite, while methylated cytosines are susceptible to conversion due to the presence of the CH3 methyl group at carbon 5 level. To perform droplet digital PCR, a mix of DNA, primers and probes in a final volume of 20 µL was prepared. Then, DNA samples and oil are loaded into the wells of the droplet generator. Vacuum ensures that both samples and oil pass through the microfluidic circuits to form a constant dispersion of droplets of the same size. In each well, the 20 µL mixture of sample and reagents is divided into highly uniform compartments. Once transferred to a 96-well PCR plate, amplification is performed in a conventional thermal cycler. Next, the plate is introduced into a reader, where droplets are drawn from the wells and pass through a two-color detector. Depending on the amplitude of the fluorescence they emit, the droplets are classified as positive or negative using the following binary threshold: 1=positive, 0= negative. For ddPCR reaction 5-10µ of DNA template was added to 10 µL of ddPCR Supermix for Probes (Bio-Rad) and 5 µL of the primer and probe mix (the fluorophores used are FAM and HEX). Sample and mix were then added to a cartridge together with 60 µl of oil necessary for droplet generation (Auto-DG, Bio-Rad). These, once formed, were then transferred to a 96-well plate and then subjected to the temperature-dependent amplification reaction using the thermal cycler. Finally, to evaluate the fluorescence emitted, the droplets were analyzed with the QX200 Droplet Reader (Bio-Rad). Samples were considered methylated if the value of methylation was >30%. For whole GBM cell populations, normalization on the percentage of pTERT alterations was done to evaluate tumor cells only.

Chromosome G banding

Cell synchronization was carried out by Synchroset (Euroclone) according to manufacturer's instructions, followed by cell block with KaryoMAX™ Colcemid™ Solution (Life Technologies) ((10 µl/ml) for 1 h. Chromosome harvesting was carried out according to standard procedures. Briefly, cells were incubated in hypotonic solution (KCl 0,075 M) for 10 min and eventually in methanol-glacial acetic acid (3:1). Cell suspensions were dropped on slides and dried using specific conditions for optimal chromosome spreading. G banding was achieved by incubating slides in 2×SSC at 65 °C for 2 min and then stained with Wright's solution for 2 min (all reagents were from Sigma-Aldrich).

Acquisition of metaphases was performed using an Olympus BX61 microscope (Olympus Corporation) and the analysis was carried out by CytoVision software 7.2 (Leica Biosystems). A mid-range resolution of 300 bands was achieved. The anomalies were reported according to the International System for Human Cytogenetic Nomenclature, 2020.

Chromosome M-FISH

Chromosome analysis by Multicolor-Fluorescence In Situ Hybridization (M-FISH) was performed on cells lines through a commercial mixture containing 24 chromosome-specific painting probes labeled with different fluorochromes (24×Cyte kit MetaSystems) (MetaSystems Probes GmbH). Probes and metaphase chromosomes denaturation and hybridization were performed according to manufacturer's instructions: slides were incubated at 70 °C in saline solution (2× SSC), denatured in 0.07N NaOH, dehydrated in an ethanol series and air-dried. Probe denaturation was carried out by incubating probe cocktail at 75°C (±1°C) for 5min, 2 minutes on ice and at 37°C (±1°C) for 30 min.

10 µl of the denaturated probe cocktail were put onto slides and hybridization for 24h at 37 °C followed. Subsequently, slides were washed with post-hybridization buffers and counterstained with 10 µl of DAPI/antifade (MetaSystems Probes GmbH). The Metafer System and the Metasytems ISIS software (Carl Zeiss) were used for signal detection and metaphase analysis. At least ten metaphases of each culture exhibiting the same chromosomal anomalies were studied for each cell line.

Quantitative real-time PCR (qPCR)

Purified mRNAs were reverse transcribed starting from 150 or 250 ng of total RNA and using High-Capacity cDNA Reverse Transcription Kit (Thermo Fisher). Real-time PCR for evaluation of gene mRNA expression was performed using primer and probe sets (Thermo Fisher) listed in the Methods Table, with TaqMan Universal PCR Master Mix and an ABI PRISM 7900HT sequence detection system (Thermo Fisher). Expression levels were normalized against endogenous controls (GAPDH or β2 microglobulin). When appropriate, control cells were used as calibrators. Expression levels were reported as 40-Ct or as fold vs. control cells and are the results of a representative experiment in triplicate.

γH2AX immunofluorescent assay

NS were mechanically dissociated at single cell level and 10^5 cells were seeded in 6-well plate. 6 days after seeding, cells were irradiated with a single 5 Gy dose and were fixed 1, 2, 3 and 4 hours after with PAF 4% for 20 min. Fixed cells were washed with milliQ water, resuspended in 100 µL of water and seeded on poly-lysinated slides. Cells were then washed with PBS 3× for 5 min, permeabilized with HEPES-Triton for 5 min, washed with PBS for 5 min and saturated with PBS-BSA 5% for 1 h. Primary antibody γH2AX (see Methods table), diluted 1:200 in PBS-BSA 0.5%, was incubated for 2 h RT. Appropriate AlexaFluor conjugated secondary antibody was used (Thermo Fisher, 1:1000 in PBA-BSA 0.5%) for 1 h RT. DAPI was added for 30 sec. Images were captured using LASV4.2 software on a LEICA SPEII confocal microscope. The percentage of γH2AX positive cells has been measured by counting positive cells/nuclei (DAPI pos) in at least 10 HMFs.

Western blotting

NS proteins were extracted with boiling Laemli Buffer or RIPA buffer. Total amount of proteins obtained was quantified using the BCA System (Pierce). Up to 15 ug of proteins were loaded on a 4-15/4-20% pre-casted polyacrylamide gel (Biorad) and transferred on nitrocellulose. Primary antibodies used were MGMT, pCHK2, CHK2, RAD51, γH2AX, EGFR, MET, PDGFRα, PDGFRβ, FGFR1, FGFR2, FGRF4, FGFR4, BAX, BAK, BIM, BAD, NOXA, HRK, BCL-2, BCL-xL, MCL1, pERK and ERK (see Methods Table for details). Antibodies were visualized with appropriate horseradish peroxidase-conjugated secondary antibodies (Jackson Lab) and enhanced chemiluminescence system (Promega). Blot images were captured using the ChemiDoc TouchTM Imaging System (Biorad) with Image Lab software (Biorad). H3, β-actin, vinculin and calnexin were used as protein loading control where indicated.

Immunoprecipitation

Proteins were extracted with cold EB buffer in the presence of protease inhibitors (Thermo Fisher) and quantified using the BCA System (Pierce). Immunoprecipitation was performed by incubating 500 µg of protein extracts with the anti-BCL-XL primary antibody on Protein A magnetic beads (GE Healthcare) for 1.5 hour at RT. Immunoprecipitated and unbounded proteins were loaded on a 4-20% pre-casted polyacrylamide gel (Biorad) and transferred on nitrocellulose. Primary antibodies used were BIM and BCL-XL (see Methods Table for details).

Flow-cytometric analyses

All cases were extensively characterized for immunophenotype by multiparametric flow cytometry. From growing NS, single cell suspension was obtained by mechanical disaggregation, immediately counted and evaluated for cell viability in Biorad TC20 automated cell counter, in order to verify that viability was more than 70% and that total number of viable cells was greater than 1.5×10^6. Death cells were excluded from analysis using DAPI (Roche) staining. Cells were then washed with PBS/BSA 1% and resuspended in the same solution at 2×10^5 cells/100 □L. 100 □L of samples were directly added to a monoclonal antibody mixture, incubated 20 minutes RT, washed twice with PBS/BSA 1%, resuspended in 300 µL of PBS/DAPI 0.2X and immediately acquired. The immunophenotypic sample acquisitions were performed by a CyAn ADP (Beckman Coulter) equipped with 3 solid state lasers (488 nm, 405 nm and 642 nm) and 8 colors. Analyses were performed by Summit 4.3 software (Beckman Coulter). The antibodies used for immunophenotype characterization were detailed in the Methods Table.

FC score was calculated as the sum of the percentage of positive cells and the mean fluorescent intensity (MFI), according to Table 6.

Table 6. FC score based on % of positive cells and MFI

% of positive cells	score	Mean Fluorescence Intensity (MFI)	score
0-5	0	0	0
6-20	1	<25	1
21-40	2	<100	2
41-60	3	<250	3
61-80	4	<500	4
81-100	5	>500	5

BH3 profiling assay

The BH3 profiling assay was performed according to the protocol described by Lethai et.al. [110] and optimized for NS cultures. Briefly, NS were mechanically dissociated, washed with PBS for 5 min and stained with near-IR LIVE/DEAD^{TM} Fixable Dead Cell Stain Kit (Thermo Fisher) for 30 min to distinguish live versus dead cells. Cells were then suspended in MEB buffer [110] to the final concentration of 2×10^6 cells/mL and 50 µL of cell suspension were added to each well of a 96-well plate (Corning). BIM-BH3 peptide (New England Peptide) at twice its final concentration in MEB plus 0.002% digitonin were pre-added to each well (50 µL/well). The plate was incubated at 25°C for 60 min in the INCU-Line incubator (VWR International) followed by the addition of 33 mL PAF 4% in PBS for 10 min RT. Fixation was ended by the addition of 33 µL of buffer N2 (Ryan, 2016) for at least 5 min. Cytochrome c staining was performed by adding 20 µL of a 1:40 dilution of anti-cytochrome C antibody (BioLegend) in BD Perm/Wash Buffer O/N at 4°C. DMSO was used as a control for complete cytochrome C retention, while alamethicin (25 µmol/L), which induces BAX/BAK-independent MOMP, was used as control for full cytochrome C release. During FACS analysis, gate on cells exposed to DMSO provided the percentage of cytochrome C positive cells, and 100 minus this value defined the percentage of cytochrome c release. Analysis was performed on a Cytoflex LX (Beckman Coulter). Data were collected and processed using CytExpert 2.4 software (Beckman Coulter). Data were reported as mean ± SEM of at least two independent experiments.

Cell viability assays

Approximately 10^3 cells per well were plated in a 96-well plate 24 hours before starting the treatment, and viability was measured by CellTiter-Glo Luminescent Cell Viability Assay (Promega) using a GloMax 96 Microplate Luminometer (Promega) as detailed below.

To evaluate TMZ doses able to discriminate between sensitive and resistant cells, TMZ doses were increased up to 500 µM and cell viability was measured 0, 3, 6, 9, 12, 15, and 18 days after the beginning of the treatment. To evaluate IR doses able to discriminate between sensitive and resistant cells, cells were irradiated with a dose of 2 Gy administered up to for five consecutive days and cells viability was measured 48 hours after the last dose. Data are reported as mean ± SEM of a single representative experiment in six replicates. Images of a representative MGMT-neg GBM population treated with TMZ at 50 µM, and of a representative radiosensitive GBM population treated ex-vivo with IR 2 Gy for 5 consecutive days were captured using LASV4.2 software on a contrast-phase microscope and are representative of at least three different images.

To evaluate cell response to chemotherapy, cells were treated at day 0, 3 and 6 with TMZ (Sigma), with doses ranging from 1 to 50 µM, and cell viability was measured 0, 3, 6 and 9 days after the beginning of the treatment. Cell viability at day 9 was shown. To evaluate cell response to IR, cells were irradiated with a dose of 2 Gy administered for three consecutive days or with a single dose of 5 Gy. Cell viability was measured 24 and 48 hours after the last treatment. In both cases, data are reported as mean ± SEM of at least two independent experiments in six replicates.

To evaluate response to Lapatinib and BH3 mimetics, alone and in combination, cells were treated at day 0 with the indicated drug and cell viability was measured 48 hours after the beginning of the treatment. Data are reported as mean ± SEM of at least two independent experiments in six replicates, but the combination experiment, where data from representative experiment were shown.

Clonogenic assay

Clonogenic assay was performed as described earlier [92]. Cells were seeded at the concentration of 25 cells per well (60 well in total) in 96-well plates in the culture medium. To evaluate cell response to chemotherapy, TMZ stimuli at 5 and 50 μM were administered once 24 hours after seeding. To evaluate cell response to IR, cells were irradiated with a dose of 2 Gy administered once (2 Gy) or for three consecutive days (2 Gy × 3) or with a single dose of 5 Gy. NS generated in all conditions were counted when vehicle/mock-treated cells displayed formed NS. Residual clonogenic potential after treatment (i.e. surviving fraction) was calculated normalizing the number of NS in each condition with the number of NS in vehicle/mock-treated wells and considering the plating efficiency. Data are reported as mean ± SEM of at least two independent experiments.

Limiting dilution assay

Cells were seeded at the concentration of 100, 50, 25, 10, 5 and 1 cell per well (10 replicates for each condition) in 96-well plates in the culture medium. Wells containing NS were counted and data were analyzed with ELDA software (http://bioinf.wehi.edu.au/software/elda/). For p1 passage, NS were collected and dissociated, and derived cells were seeded at the same concentrations described above. Data reported have been obtained from passage p0 for GBM17 and p1 for GBM95.

Cell proliferation assay

Cell proliferation was measured by CellTiter-Glo Luminescent Cell Viability Assay (Promega) using a GloMax 96 Microplate Luminometer (Promega) at day 0 (ctrl), and at the indicated time points after treatment. To evaluate basal proliferative rate, 10^3 dissociated cells per well were seeded in a 96-well plate at day -1 in the culture media and cell viability was measured at day 0, 3 and 6. Data were reported as mean ± SEM of at least two independent experiments (n =6). To evaluate the responsiveness to single GF and the ability to growth in the absence of exogenous stimuli, 10^3 dissociated cells per well were seeded in a 96-well plate at day -1 in a medium devoid of any GF; on day 0 cells were stimulated with the indicated GF. Data were reported as mean ± SEM of at least two independent experiments (n =6) in case of the proliferation in absence of GF, and were reported as mean ± SEM of a representative experiment (n=6) in case of proliferation in response to single GFs.

Fluorescence-based multiplex flow-cytometric host cell reactivation assay (FM-HCR)

Plasmids for MMR activity evaluation through FM-HCR [96] ((pmax BFP and pmax mOrange control plasmids, and pmax mOrange G:G plasmid, which give a FC signal only in cells MMR proficient) were kindly provided by Professor Zachary D. Nagel (Harvard T.H. Chan School of Public Health). Experiments were carried out using 12 well plates. For each condition, detailed in Table 7, 2 wells with 1.25×10^5 cells were plated in 1 mL of complete medium without antibiotic antimitotic solution, implemented with 5% of fetal bovine serum (Gibco). 24 h after plating, cells were transfected using, for each well, 100 µL of Opti-Mem containing: 25 ng of plasmid(s) DNA (see Table 7 for the experimental scheme), 850 ng of carrier DNA (sheared ssDNA) and 4 µL of TransIT-X2 Dynamic Delivery System (mirus bio).

24 h post-transfection, cells were harvested, washed in PBS 1X, and each sample was resuspended in 250µL of a solution containing LIVE/DEAD Fixable Near-IR Dead Cell (ThermoFisher) diluted 1:1000 in PBS/BSA 1%. Cells were incubated for 30 min RT in the dark on a seesaw rocker. After washing in PBS 1X to remove excess dye, samples were resuspended in 200 µL of PBS 1X and immediately analyzed by FC. Sample acquisition was performed using a CytoFLEX LX (Beckman Coulter) equipped with 5 solid-state lasers (375 nm, 405 nm, 488 nm, 561 nm, 638 nm). Analyses were performed using CytExpert software (Beckman Coulter).

MMR efficiency (Z, percentage of reporter expression) was calculated as follow:

$$X= \frac{mOrange\ G{:}G\ normalized\ count\ x\ mean\ mOrange\ G{:}G\ intensity}{BFP\ normalized\ count\ x\ Mean\ BFP\ intensity}$$

$$Y= \frac{\text{mOrange normalized count x mean mOrange intensity}}{\text{BFP normalized count x Mean BFP intensity}}$$

$$Z= \frac{X}{Y} \times 100$$

Table 7. Conditions for FM-HCR array

Tube n.	Plasmid 1	Plasmid 2	Function
1	-	-	Negative control
2	pmax BFP	-	Instrument setting
3	pmax mOrange	-	Instrument setting
4	pmax BFP	pmax mOrangeG:G	TEST tube
5	pmax BFP	pmax mOrange	Reference tube

Statistical analysis

Data are expressed as mean ± SEM, unless otherwise specified. $p < 0.05$ was considered statistically significant.

The followings statistical tests were performed:

i) Student’ t test, to evaluate significant differences between the averages of two groups

ii) ANOVA, to evaluate significant differences among more than two groups

iii) Fisher’s exact test, to evaluate correlations between two groups and two features

iv) Log-rank Mantel-Cox test, to evaluate significant differences between the overall survival (OS) and progression-free survival (PFS) between two groups

v) Pairwise tests provided by ELDA software (http://bioinf.wehi.edu.au/software/elda/), to evaluate significant differences in LDA among groups.

METHODS TABLE

REAGENT or RESOURCE	SOURCE	IDENTIFIER
Antibodies		
anti-MGMT antibodies	Cell Signaling Technology	cat#2739 (WB 1:500)
anti-EGFR (D38B1) antibodies	Cell Signaling Technology	cat#4267 (WB 1:1000)
anti-MET DL21 antibodies	Prat et al. [158]	N/A (WB 1:1500)
anti-PDFGFRα (D1E1E) antibodies	Cell Signaling Technology	cat#3174(WB 1:1000)
anti-PDGFRβ(C82A3) antibodies	Cell Signaling Technology	cat#4564(WB 1:1000)
anti-FGFR1 antibodies	Cell Signaling Technology	cat#3472(WB 1:1000)
anti-FGFR2 (D4H9) antibodies	Cell Signaling Technology	cat#11835(WB 1:1000)
anti-FGFR3 (2H10B4)	Novusbio	cat#NBP2-52468 (WB 1:500)
anti-FGFR4	Cell Signaling Technology	cat#2894(WB 1:1000)
anti-BAX antibodies	Cell Signaling Technology	cat#2772(WB 1:1000)
anti-BAK (D4E4) antibodies	Cell Signaling Technology	cat#12105(WB 1:1000)
anti-BIM (C34C5) antibodies	Cell Signaling Technology	cat#2933(WB 1:1000)
anti-BAD (D24A9) antibodies	Cell Signaling Technology	cat#9239(WB 1:1000)
anti-NOXA (clone 114C307.1) antibodies	Enzo Life Science	cat#ALX-804-408 (WB 1:500)
anti-HRK antibodies	Sigma-Aldrich	cat#PRS3771 (WB 1:1000)
anti-BCL-2(D55G8) antibodies	Cell Signaling Technology	cat#4223(WB 1:1000)
anti-BCL-xL (54H6) antibodies	Cell Signaling Technology	cat#2933(WB 1:1000, IP 1:100)
anti-MCL1 (D35A5) antibodies	Cell Signaling Technology	cat#5453(WB 1:1000)
anti-ERK1,2 antibodies	Cell Signaling Technology	cat#9102(WB 1:1000)
anti-phospho-Erk1,2 (Thr202/Tyr204) (D13.14.4E) antibodies	Cell Signaling Technology	cat#4370(WB 1:1000)
anti-RAD51 (D4B10) antibodies	Cell Signaling Technology	cat#8875(WB 1:1000)
anti-Phospho-Histone H2A.X (Ser139) (20E3) antibodies	Cell Signaling Technology	cat#9718(WB 1:1000, IF 1:200)
anti-Phospho-Chk2 (Thr68) antibodies	Cell Signaling Technology	cat#2661(WB 1:1000)
anti-CHK2 antibodies	Cell Signaling Technology	cat#3440(WB 1:1000)
anti-β-Actin (D6A8) antibodies	Cell Signaling Technology	cat#8457(WB 1:1000)
anti-Vinculin antibodies	Sigma-Aldrich	cat#V9131 (WB 1:200)
anti-H3 (clone 6.6.2) antibodies	Millipore	cat# 05-499(WB 1:45000)
anti-Calnexin (C5C9) antibodies	Cell Signaling Technology	cat#2679(WB 1:1000)
Alexa Fluor® 488 anti-Cytochrome c (clone 6H2.B4) antibodies	BioLegend	cat#612308(FC 1:40)
Alexa Fluor® 488 anti-human EGFR Antibody	BioLegend	cat#352908(FC 1:20)
anti-HGFR/c-MET PE-Cy7 antibodies	BioTechne	cat#MAB3582(FC 1:100)
anti-PDFGFRα (clone 16A1) PE antibodies	BioLegend	cat#323506(FC 1:20)
anti-PDGFRβ (clone 18A2) APC antibodies	BioLegend	cat#323608(FC 1:20)

anti-FGFR2 APC antibodies	BioTechne	cat#FAB684A(FC 1:20)
anti-FGFR3 FITC/APC antibodies	BioTechne	cat#FAB6852A(FC 1:20)
anti-FGFR4 PE/APC antibodies	BioTechne	cat#FAB766A(FC 1:20)
Oligonucleotides		
CN probe: CDKN2A	Thermo Fisher	cat#Hs03714372_cn
CN probe: CDKN2B	Thermo Fisher	cat#Hs02900430_cn
CN probe: PTEN	Thermo Fisher	cat#Hs02599450_cn
CN probe: EGFR	Thermo Fisher	cat#Hs.PT.58.27649789.g
CN probe: PDGFRA	Thermo Fisher	cat#Hs05935655_cn
CN probe: MET	Thermo Fisher	cat#Hs04993403_cn
CN probe: HGF	Thermo Fisher	cat#Hs02789622_cn
CN probe: MYC	Thermo Fisher	cat#Hs00834648_cn
CN probe: MYCN	Thermo Fisher	cat#Hs02029019_cn
CN probe: CDK4	Thermo Fisher	cat#Hs00923687_cn
CN probe: PIK3CA	Thermo Fisher	cat#Hs00923687_cn
CN probe :MDM2	IDT	5'-CCTGTCTATCCTTTCCTGTGTTC-3'
		5'-GGGATGTGGGAGAGTTTGTTAT-3'
		5'-/56FAM/TTGCATGGT/ZEN/GGAAAGGTTTGTGGG/3IABkFQ/-3'
CN probe: RNAseP	Thermo Fisher	cat#4403328
CN probe: GREB	Thermo Fisher	cat#Hs01738470_cn
CN probe: APOA1	IDT	cat#Hs.PT.56A.40574746.g
ddPCR probe: TERT C228T_113	Bio-Rad	cat#dHsaEXD72405942
ddPCR probe: TERT C250T_113	Bio-Rad	cat#dHsaEXD46675715
ddPCR probe:MSH6 p.G1138R	Bio-Rad	cat#dHsaMDS936080621
ddPCR probe:MSH6 p.W106	Bio-Rad	cat# dHsaMDS524274355
ddPCR probe:MSH5 p.G251R	Bio-Rad	cat#dHsaMDS111253038
ddPCR probe:MSH2 p.A771T	Bio-Rad	cat#dHsaMDS959063564
ddPCR probe:MSH6 p.T1219I	Bio-Rad	cat# dHsaMDS362358516
EGFR-wt FW	Sigma-Aldrich	CCAGTATTGATCGGGAGAGC
EGFR-wt REV	Sigma-Aldrich	CCAAGGACCACCTCACAGTT
EGFR-vIII.1 FW	Sigma-Aldrich	GGCTCTGGAGGAAAAGAAAGGTAAT
EGFR-vIII.1 REV	Sigma-Aldrich	TCCTCCATCTCATAGCTGTCG
EGFR-vIII.2 FW	Sigma-Aldrich	GAGCTCTTCGGGGAGCAG
EGFR-vIII.2 REV	Sigma-Aldrich	GTGATCTGTCACCACATAATTACCTTTCT
gene expression probe:MGMT	Thermo Fisher	cat#:Hs01037698_m1
gene expression probe:PMAIP1	Thermo Fisher	cat#:Hs00560402_m1
gene expression probe:BCL2L11	Thermo Fisher	cat#:Hs00708019_s1
gene expression probe:BAX	Thermo Fisher	cat#:Hs00180269_m1
gene expression probe:BCL2	Thermo Fisher	cat#:Hs00608023_m1
gene expression probe:BBC3	Thermo Fisher	cat#:Hs00248075_m1
gene expression probe:BCL2L1	Thermo Fisher	cat#:Hs00236329_m1
gene expression probe:BAK1	Thermo Fisher	cat#:Hs00832876_g1
gene expression probe:BAD	Thermo Fisher	cat#:Hs00188930_m1
gene expression probe:BIK	Thermo Fisher	cat#:Hs00154189_m1
gene expression probe:HRK	Thermo Fisher	cat#:Hs02621354_s1
gene expression probe:BID	Thermo Fisher	cat#:Hs01026792_m1
gene expression probe:MCL1	Thermo Fisher	cat#:Hs01050896_m1
gene expression probe:beta-2 microglobulin	Thermo Fisher	cat#:Hs00984230_m1

gene expression probe:GAPDH	Thermo Fisher	cat#:Hs99999905_m1
Solftware and algorithms		
cBioPortal site for Cancer Genomics		http://www.cbioportal.org/
The Human Protein Atlas		http://www.proteinatlas.org
Gliovis data portal		http://gliovis.bioinfo.cnio.es/
GraphPad Prism 8.3.0	GraphPad software	www.graphpad.com
COSMIC	Sanger Institute	http://cancer.sanger.ac.uk/cosmic
MutationTaster2021		https://www.genecascade.org/
AlphaMissense		http://alphamissense.hegelab.org
Summit 4.3	software Beckman Coulter	PN998403C
CytExpert 2.6	software Beckman Coulter	
ELDA: Extreme Limiting Dilution Analysis		http://bioinf.wehi.edu.au/software/elda/
Image Lab	software Bio-Rad	cat#17006130
ImageJ	NIH	https://ImageJ.nih.gov

BIBLIOGRAPHY

1. Louis, D.N., et al., *The 2021 WHO Classification of Tumors of the Central Nervous System: a summary.* Neuro Oncol, 2021. **23**(8): p. 1231-1251.
2. Weller, M., et al., *Glioma.* Nat Rev Dis Primers, 2024. **10**(1): p. 33.
3. Stupp, R., et al., *Radiotherapy plus concomitant and adjuvant temozolomide for glioblastoma.* N Engl J Med, 2005. **352**(10): p. 987-96.
4. Fu, D., J.A. Calvo, and L.D. Samson, *Balancing repair and tolerance of DNA damage caused by alkylating agents.* Nat Rev Cancer, 2012. **12**(2): p. 104-20.
5. Weller, M., et al., *MGMT promoter methylation in malignant gliomas: ready for personalized medicine?* Nat Rev Neurol, 2010. **6**(1): p. 39-51.
6. Butler, M., et al., *MGMT Status as a Clinical Biomarker in Glioblastoma.* Trends Cancer, 2020. **6**(5): p. 380-391.
7. Stupp, R., et al., *Effects of radiotherapy with concomitant and adjuvant temozolomide versus radiotherapy alone on survival in glioblastoma in a randomised phase III study: 5-year analysis of the EORTC-NCIC trial.* Lancet Oncol, 2009. **10**(5): p. 459-66.
8. Ostrom, Q.T., et al., *CBTRUS Statistical Report: Primary Brain and Other Central Nervous System Tumors Diagnosed in the United States in 2016-2020.* Neuro Oncol, 2023. **25**(12 Suppl 2): p. iv1-iv99.
9. Lim, M., et al., *Current state of immunotherapy for glioblastoma.* Nat Rev Clin Oncol, 2018. **15**(7): p. 422-442.
10. Arrieta, V.A., et al., *Immune checkpoint blockade in glioblastoma: from tumor heterogeneity to personalized treatment.* J Clin Invest, 2023. **133**(2).
11. Le Rhun, E., et al., *Molecular targeted therapy of glioblastoma.* Cancer Treat Rev, 2019. **80**: p. 101896.
12. Cruz Da Silva, E., et al., *A Systematic Review of Glioblastoma-Targeted Therapies in Phases II, III, IV Clinical Trials.* Cancers (Basel), 2021. **13**(8).
13. Oprita, A., et al., *Updated Insights on EGFR Signaling Pathways in Glioma.* Int J Mol Sci, 2021. **22**(2).
14. Fougner, V., et al., *Implementing targeted therapies in the treatment of glioblastoma: Previous shortcomings, future promises, and a multimodal strategy recommendation.* Neurooncol Adv, 2022. **4**(1): p. vdac157.
15. Capper, D., et al., *EANO guideline on rational molecular testing of gliomas, glioneuronal, and neuronal tumors in adults for targeted therapy selection.* Neuro Oncol, 2023. **25**(5): p. 813-826.
16. Verhaak, R.G., et al., *Integrated genomic analysis identifies clinically relevant subtypes of glioblastoma characterized by abnormalities in PDGFRA, IDH1, EGFR, and NF1.* Cancer Cell, 2010. **17**(1): p. 98-110.
17. Brennan, C.W., et al., *The somatic genomic landscape of glioblastoma.* Cell, 2013. **155**(2): p. 462-77.
18. Sturm, D., et al., *Hotspot mutations in H3F3A and IDH1 define distinct epigenetic and biological subgroups of glioblastoma.* Cancer Cell, 2012. **22**(4): p. 425-37.
19. Ceccarelli, M., et al., *Molecular Profiling Reveals Biologically Discrete Subsets and Pathways of Progression in Diffuse Glioma.* Cell, 2016. **164**(3): p. 550-563.
20. Capper, D., et al., *DNA methylation-based classification of central nervous system tumours.* Nature, 2018. **555**(7697): p. 469-474.
21. Wang, Q., et al., *Tumor Evolution of Glioma-Intrinsic Gene Expression Subtypes Associates with Immunological Changes in the Microenvironment.* Cancer Cell, 2017. **32**(1): p. 42-56.e6.
22. Sottoriva, A., et al., *Intratumor heterogeneity in human glioblastoma reflects cancer evolutionary dynamics.* Proc Natl Acad.Sci.U.S.A, 2013. **110**(10): p. 4009-4014.
23. Snuderl, M., et al., *Mosaic amplification of multiple receptor tyrosine kinase genes in glioblastoma.* Cancer Cell, 2011. **20**(6): p. 810-7.
24. Szerlip, N.J., et al., *Intratumoral heterogeneity of receptor tyrosine kinases EGFR and PDGFRA amplification in glioblastoma defines subpopulations with distinct growth factor response.* Proc Natl Acad Sci U S A, 2012. **109**(8): p. 3041-6.

25. Patel, A.P., et al., *Single-cell RNA-seq highlights intratumoral heterogeneity in primary glioblastoma.* Science, 2014. **344**(6190): p. 1396-401.
26. Neftel, C., et al., *An Integrative Model of Cellular States, Plasticity, and Genetics for Glioblastoma.* Cell, 2019. **178**(4): p. 835-849.e21.
27. Garofano, L., et al., *Pathway-based classification of glioblastoma uncovers a mitochondrial subtype with therapeutic vulnerabilities.* Nat Cancer, 2021. **2**(2): p. 141-156.
28. Meyer, M., et al., *Single cell-derived clonal analysis of human glioblastoma links functional and genomic heterogeneity.* Proc Natl Acad Sci U S A, 2015. **112**(3): p. 851-6.
29. Parker, N.R., et al., *Intratumoral heterogeneity identified at the epigenetic, genetic and transcriptional level in glioblastoma.* Sci Rep, 2016. **6**: p. 22477.
30. Reinartz, R., et al., *Functional Subclone Profiling for Prediction of Treatment-Induced Intratumor Population Shifts and Discovery of Rational Drug Combinations in Human Glioblastoma.* Clin Cancer Res, 2017. **23**(2): p. 562-574.
31. Qazi, M.A., et al., *Intratumoral heterogeneity: pathways to treatment resistance and relapse in human glioblastoma.* Ann Oncol, 2017. **28**(7): p. 1448-1456.
32. Kim, J., et al., *Spatiotemporal Evolution of the Primary Glioblastoma Genome.* Cancer Cell, 2015. **28**(3): p. 318-28.
33. Wang, J., et al., *Clonal evolution of glioblastoma under therapy.* Nat Genet, 2016. **48**(7): p. 768-76.
34. Orzan, F., et al., *Genetic Evolution of Glioblastoma Stem-Like Cells From Primary to Recurrent Tumor.* Stem Cells, 2017. **35**(11): p. 2218-2228.
35. Osuka, S. and E.G. Van Meir, *Overcoming therapeutic resistance in glioblastoma: the way forward.* J Clin Invest, 2017. **127**(2): p. 415-426.
36. Barthel, F.P., et al., *Longitudinal molecular trajectories of diffuse glioma in adults.* Nature, 2019. **576**(7785): p. 112-120.
37. Körber, V., et al., *Evolutionary Trajectories of IDHWT Glioblastomas Reveal a Common Path of Early Tumorigenesis Instigated Years ahead of Initial Diagnosis.* Cancer Cell, 2019. **35**(4): p. 692-704.e12.
38. Touat, M., et al., *Mechanisms and therapeutic implications of hypermutation in gliomas.* Nature, 2020. **580**(7804): p. 517-523.
39. Marusyk, A., M. Janiszewska, and K. Polyak, *Intratumor Heterogeneity: The Rosetta Stone of Therapy Resistance.* Cancer Cell, 2020. **37**(4): p. 471-484.
40. Lathia, J.D., et al., *Cancer stem cells in glioblastoma.* Genes Dev, 2015. **29**(12): p. 1203-17.
41. Gimple, R.C., et al., *Glioblastoma stem cells: lessons from the tumor hierarchy in a lethal cancer.* Genes Dev, 2019. **33**(11-12): p. 591-609.
42. Singh, S.K., et al., *Identification of a cancer stem cell in human brain tumors.* Cancer Res, 2003. **63**(18): p. 5821-8.
43. Galli, R., et al., *Isolation and characterization of tumorigenic, stem-like neural precursors from human glioblastoma.* Cancer Res, 2004. **64**(19): p. 7011-21.
44. Alcantara Llaguno, S., et al., *Malignant astrocytomas originate from neural stem/progenitor cells in a somatic tumor suppressor mouse model.* Cancer Cell, 2009. **15**(1): p. 45-56.
45. Lee, J.H., et al., *Human glioblastoma arises from subventricular zone cells with low-level driver mutations.* Nature, 2018. **560**(7717): p. 243-247.
46. Alcantara Llaguno, S.R., et al., *Adult Lineage-Restricted CNS Progenitors Specify Distinct Glioblastoma Subtypes.* Cancer Cell, 2015. **28**(4): p. 429-440.
47. Uhrbom, L., et al., *Ink4a-Arf loss cooperates with KRas activation in astrocytes and neural progenitors to generate glioblastomas of various morphologies depending on activated Akt.* Cancer Res, 2002. **62**(19): p. 5551-8.
48. Ozawa, T., et al., *Most human non-GCIMP glioblastoma subtypes evolve from a common proneural-like precursor glioma.* Cancer Cell, 2014. **26**(2): p. 288-300.

49. Liu, C., et al., *Mosaic analysis with double markers reveals tumor cell of origin in glioma.* Cell, 2011. **146**(2): p. 209-21.
50. Friedmann-Morvinski, D., et al., *Dedifferentiation of neurons and astrocytes by oncogenes can induce gliomas in mice.* Science, 2012. **338**(6110): p. 1080-4.
51. Sloan, A.R., et al., *Cancer stem cell hypothesis 2.0 in glioblastoma: Where are we now and where are we going?* Neuro Oncol, 2024. **26**(5): p. 785-795.
52. Lee, J., et al., *Tumor stem cells derived from glioblastomas cultured in bFGF and EGF more closely mirror the phenotype and genotype of primary tumors than do serum-cultured cell lines.* Cancer Cell, 2006. **9**(5): p. 391-403.
53. Vescovi, A.L., R. Galli, and B.A. Reynolds, *Brain tumour stem cells.* Nat Rev Cancer, 2006. **6**(6): p. 425-36.
54. Singh, S.K., et al., *Identification of human brain tumour initiating cells.* Nature, 2004. **432**(7015): p. 396-401.
55. Son, M.J., et al., *SSEA-1 is an enrichment marker for tumor-initiating cells in human glioblastoma.* Cell Stem Cell, 2009. **4**(5): p. 440-52.
56. Anido, J., et al., *TGF-beta Receptor Inhibitors Target the CD44(high)/Id1(high) Glioma-Initiating Cell Population in Human Glioblastoma.* Cancer Cell, 2010. **18**(6): p. 655-668.
57. Lathia, J.D., et al., *Integrin alpha 6 regulates glioblastoma stem cells.* Cell Stem Cell, 2010. **6**(5): p. 421-32.
58. Bao, S., et al., *Glioma stem cells promote radioresistance by preferential activation of the DNA damage response.* Nature, 2006. **444**(7120): p. 756-760.
59. Squatrito, M. and E.C. Holland, *DNA damage response and growth factor signaling pathways in gliomagenesis and therapeutic resistance.* Cancer Res, 2011. **71**(18): p. 5945-5949.
60. De Bacco, F., et al., *MET inhibition overcomes radiation resistance of glioblastoma stem-like cells.* EMBO Mol Med, 2016. **8**(5): p. 550-68.
61. Chen, J., et al., *A restricted cell population propagates glioblastoma growth after chemotherapy.* Nature, 2012. **488**(7412): p. 522-6.
62. Suvà, M.L. and I. Tirosh, *The Glioma Stem Cell Model in the Era of Single-Cell Genomics.* Cancer Cell, 2020. **37**(5): p. 630-636.
63. Wang, L., et al., *The Phenotypes of Proliferating Glioblastoma Cells Reside on a Single Axis of Variation.* Cancer Discov, 2019. **9**(12): p. 1708-1719.
64. Richards, L.M., et al., *Gradient of Developmental and Injury Response transcriptional states defines functional vulnerabilities underpinning glioblastoma heterogeneity.* Nat Cancer, 2021. **2**(2): p. 157-173.
65. Couturier, C.P., et al., *Single-cell RNA-seq reveals that glioblastoma recapitulates a normal neurodevelopmental hierarchy.* Nat Commun, 2020. **11**(1): p. 3406.
66. Prager, B.C., et al., *Glioblastoma Stem Cells: Driving Resilience through Chaos.* Trends Cancer, 2020. **6**(3): p. 223-235.
67. Yabo, Y.A., S.P. Niclou, and A. Golebiewska, *Cancer cell heterogeneity and plasticity: A paradigm shift in glioblastoma.* Neuro Oncol, 2022. **24**(5): p. 669-682.
68. Pu, Y., et al., *Drug-tolerant persister cells in cancer: the cutting edges and future directions.* Nat Rev Clin Oncol, 2023. **20**(11): p. 799-813.
69. Nicholson, J.G. and H.A. Fine, *Diffuse Glioma Heterogeneity and Its Therapeutic Implications.* Cancer Discov, 2021. **11**(3): p. 575-590.
70. Aldape, K., et al., *Challenges to curing primary brain tumours.* Nat Rev Clin Oncol, 2019. **16**(8): p. 509-520.
71. Lenting, K., et al., *Glioma: experimental models and reality.* Acta Neuropathol, 2017. **133**(2): p. 263-282.
72. Boccaccio, C. and P.M. Comoglio, *The MET oncogene in glioblastoma stem cells: implications as a diagnostic marker and a therapeutic target.* Cancer Res, 2013. **73**(11): p. 3193-9.

73. Piccirillo, S.G., et al., *Distinct pools of cancer stem-like cells coexist within human glioblastomas and display different tumorigenicity and independent genomic evolution.* Oncogene, 2009. **28**(15): p. 1807-1811.
74. De Bacco, F., et al., *Coexisting cancer stem cells with heterogeneous gene amplifications, transcriptional profiles, and malignancy are isolated from single glioblastomas.* Cell Rep, 2023. **42**(8): p. 112816.
75. De Bacco, F., et al., *Protocol for in vitro establishment of heterogeneous stem-like cultures derived from whole human glioblastoma tumors.* STAR Protoc, 2023. **4**(4): p. 102705.
76. Kim, H., et al., *Whole-genome and multisector exome sequencing of primary and post-treatment glioblastoma reveals patterns of tumor evolution.* Genome Res, 2015. **25**(3): p. 316-27.
77. Consortium, G., *Glioma through the looking GLASS: molecular evolution of diffuse gliomas and the Glioma Longitudinal Analysis Consortium.* Neuro Oncol, 2018. **20**(7): p. 873-884.
78. Varn, F.S., et al., *Glioma progression is shaped by genetic evolution and microenvironment interactions.* Cell, 2022. **185**(12): p. 2184-2199.e16.
79. Hoogstrate, Y., et al., *Transcriptome analysis reveals tumor microenvironment changes in glioblastoma.* Cancer Cell, 2023. **41**(4): p. 678-692.e7.
80. Wang, L., et al., *A single-cell atlas of glioblastoma evolution under therapy reveals cell-intrinsic and cell-extrinsic therapeutic targets.* Nat Cancer, 2022. **3**(12): p. 1534-1552.
81. Mathur, R., et al., *Glioblastoma evolution and heterogeneity from a 3D whole-tumor perspective.* Cell, 2024. **187**(2): p. 446-463.e16.
82. Kim, K.H., et al., *Integrated proteogenomic characterization of glioblastoma evolution.* Cancer Cell, 2024. **42**(3): p. 358-377.e8.
83. Liu, J., et al., *Multi-scale signaling and tumor evolution in high-grade gliomas.* Cancer Cell, 2024. **42**(7): p. 1217-1238.e19.
84. Qazi, M.A., et al., *A novel stem cell culture model of recurrent glioblastoma.* J Neurooncol, 2016. **126**(1): p. 57-67.
85. Ostermann, S., et al., *Plasma and cerebrospinal fluid population pharmacokinetics of temozolomide in malignant glioma patients.* Clin Cancer Res, 2004. **10**(11): p. 3728-36.
86. Schulte, A., et al., *Glioblastoma stem-like cell lines with either maintenance or loss of high-level EGFR amplification, generated via modulation of ligand concentration.* Clin Cancer Res, 2012. **18**: p. 1901-1913.
87. Li, H. and B.B. Yang, *Stress response of glioblastoma cells mediated by miR-17-5p targeting PTEN and the passenger strand miR-17-3p targeting MDM2.* Oncotarget, 2012. **3**(12): p. 1653-68.
88. Jaraíz-Rodríguez, M., et al., *A Short Region of Connexin43 Reduces Human Glioma Stem Cell Migration, Invasion, and Survival through Src, PTEN, and FAK.* Stem Cell Reports, 2017. **9**(2): p. 451-463.
89. Luongo, F., et al., *PTEN Tumor-Suppressor: The Dam of Stemness in Cancer.* Cancers (Basel), 2019. **11**(8).
90. Vidotto, T., et al., *Emerging role of PTEN loss in evasion of the immune response to tumours.* Br J Cancer, 2020. **122**(12): p. 1732-1743.
91. Oldrini, B., et al., *MGMT genomic rearrangements contribute to chemotherapy resistance in gliomas.* Nat Commun, 2020. **11**(1): p. 3883.
92. Franken, N.A., et al., *Clonogenic assay of cells in vitro.* Nat Protoc, 2006. **1**(5): p. 2315-9.
93. Woo, P.Y.M., et al., *A multifaceted review of temozolomide resistance mechanisms in glioblastoma beyond O-6-methylguanine-DNA methyltransferase*. 2019: Glioma.
94. McNulty, S.N., et al., *BRAF mutations may identify a clinically distinct subset of glioblastoma.* Sci Rep, 2021. **11**(1): p. 19999.
95. Alexandrov, L.B., et al., *The repertoire of mutational signatures in human cancer.* Nature, 2020. **578**(7793): p. 94-101.
96. Nagel, Z.D., et al., *Multiplexed DNA repair assays for multiple lesions and multiple doses via transcription inhibition and transcriptional mutagenesis.* Proc Natl Acad Sci U S A, 2014. **111**(18): p. E1823-32.
97. Piett, C.G., et al., *Large-scale preparation of fluorescence multiplex host cell reactivation (FM-HCR) reporters.* Nat Protoc, 2021. **16**(9): p. 4265-4298.

98. Indraccolo, S., et al., *Genetic, Epigenetic, and Immunologic Profiling of MMR-Deficient Relapsed Glioblastoma.* Clin Cancer Res, 2019. **25**(6): p. 1828-1837.

99. Kocakavuk, E., et al., *Radiotherapy is associated with a deletion signature that contributes to poor outcomes in patients with cancer.* Nat Genet, 2021. **53**(7): p. 1088-1096.

100. Spiegl-Kreinecker, S., et al., *Dynamics of chemosensitivity and chromosomal instability in recurrent glioblastoma.* Br J Cancer, 2007. **96**(6): p. 960-9.

101. Ahmed, S.U., et al., *Selective Inhibition of Parallel DNA Damage Response Pathways Optimizes Radiosensitization of Glioblastoma Stem-like Cells.* Cancer Res, 2015. **75**(20): p. 4416-28.

102. Lee, G., et al., *Dedifferentiation of Glioma Cells to Glioma Stem-like Cells By Therapeutic Stress-induced HIF Signaling in the Recurrent GBM Model.* Mol Cancer Ther, 2016. **15**(12): p. 3064-3076.

103. Ozawa, T., et al., *PDGFRA gene rearrangements are frequent genetic events in PDGFRA-amplified glioblastomas.* Genes Dev, 2010. **24**(19): p. 2205-18.

104. De Bacco, F., et al., *Induction of MET by ionizing radiation and its role in radioresistance and invasive growth of cancer.* J Natl Cancer Inst, 2011. **103**(8): p. 645-61.

105. Welsh, J.W., et al., *The c-Met receptor tyrosine kinase inhibitor MP470 radiosensitizes glioblastoma cells.* Radiat Oncol, 2009. **4**: p. 69.

106. Hanahan, D. and R.A. Weinberg, *The hallmarks of cancer.* Cell, 2000. **100**(1): p. 57-70.

107. Hanahan, D. and R.A. Weinberg, *Hallmarks of cancer: the next generation.* Cell, 2011. **144**(5): p. 646-74.

108. Singh, R., A. Letai, and K. Sarosiek, *Regulation of apoptosis in health and disease: the balancing act of BCL-2 family proteins.* Nat Rev Mol Cell Biol, 2019. **20**(3): p. 175-193.

109. Bock, F.J. and S.W.G. Tait, *Mitochondria as multifaceted regulators of cell death.* Nat Rev Mol Cell Biol, 2020. **21**(2): p. 85-100.

110. Ryan, J., et al., *iBH3: simple, fixable BH3 profiling to determine apoptotic priming in primary tissue by flow cytometry.* Biol Chem, 2016. **397**(7): p. 671-8.

111. Koessinger, A.L., et al., *Increased apoptotic sensitivity of glioblastoma enables therapeutic targeting by BH3-mimetics.* Cell Death Differ, 2022. **29**(10): p. 2089-2104.

112. Merino, D., et al., *BH3-Mimetic Drugs: Blazing the Trail for New Cancer Medicines.* Cancer Cell, 2018. **34**(6): p. 879-891.

113. Carneiro, B.A. and W.S. El-Deiry, *Targeting apoptosis in cancer therapy.* Nat Rev Clin Oncol, 2020. **17**(7): p. 395-417.

114. Montero, J. and R. Haq, *Adapted to Survive: Targeting Cancer Cells with BH3 Mimetics.* Cancer Discov, 2022. **12**(5): p. 1217-1232.

115. Diepstraten, S.T., et al., *The manipulation of apoptosis for cancer therapy using BH3-mimetic drugs.* Nat Rev Cancer, 2022. **22**(1): p. 45-64.

116. Leto, S.M., et al., *Synthetic Lethal Interaction with BCL-XL Blockade Deepens Response to Cetuximab in Patient-Derived Models of Metastatic Colorectal Cancer.* Clin Cancer Res, 2023. **29**(6): p. 1102-1113.

117. Moujalled, D., et al., *BH3 mimetic drugs cooperate with Temozolomide, JQ1 and inducers of ferroptosis in killing glioblastoma multiforme cells.* Cell Death Differ, 2022. **29**(7): p. 1335-1348.

118. Roberts, A.W., et al., *Substantial susceptibility of chronic lymphocytic leukemia to BCL2 inhibition: results of a phase I study of navitoclax in patients with relapsed or refractory disease.* J Clin Oncol, 2012. **30**(5): p. 488-96.

119. Stupp, R., R.V. Lukas, and M.E. Hegi, *Improving survival in molecularly selected glioblastoma.* Lancet, 2019. **393**(10172): p. 615-617.

120. Singh, K., et al., *Correcting the drug development paradigm for glioblastoma requires serial tissue sampling.* Nat Med, 2023. **29**(10): p. 2402-2405.

121. Behnan, J., et al., *Ultrasonic Surgical Aspirate is a Reliable Source For Culturing Glioblastoma Stem Cells.* Sci Rep, 2016. **6**: p. 32788.

122. De Bacco, F., et al., *The MET oncogene is a functional marker of a glioblastoma stem cell subtype.* Cancer Res, 2012. **72**(17): p. 4537-50.

123. Mazzoleni, S., et al., *Epidermal growth factor receptor expression identifies functionally and molecularly distinct tumor-initiating cells in human glioblastoma multiforme and is required for gliomagenesis.* Cancer Res, 2010. **70**(19): p. 7500-7513.
124. Behan, F.M., et al., *Prioritization of cancer therapeutic targets using CRISPR-Cas9 screens.* Nature, 2019. **568**(7753): p. 511-516.
125. Lin, K., et al., *Mechanism-based design of agents that selectively target drug-resistant glioma.* Science, 2022. **377**(6605): p. 502-511.
126. Laverty, D.J., et al., *ATM inhibition exploits checkpoint defects and ATM-dependent double strand break repair in TP53-mutant glioblastoma.* Nat Commun, 2024. **15**(1): p. 5294.
127. Wen, P.Y., et al., *Dabrafenib plus trametinib in patients with BRAF.* Lancet Oncol, 2022. **23**(1): p. 53-64.
128. Ferguson, S.D., et al., *Targetable Gene Fusions Associate With the IDH Wild-Type Astrocytic Lineage in Adult Gliomas.* J Neuropathol Exp Neurol, 2018. **77**(6): p. 437-442.
129. Gött, H. and E. Uhl, *FGFR3-TACCs3 Fusions and Their Clinical Relevance in Human Glioblastoma.* Int J Mol Sci, 2022. **23**(15).
130. Project, I.C.G.C.P.T., *Recurrent MET fusion genes represent a drug target in pediatric glioblastoma.* Nat Med, 2016. **22**(11): p. 1314-1320.
131. Ahmed, S.U., et al., *Selective Inhibition of Parallel DNA Damage Response Pathways Optimizes Radiosensitization of Glioblastoma Stem-like Cells.* Cancer Res, 2015.
132. van der Sluis, K., et al., *Karyotype Evolution in Response to Chemoradiotherapy and Upon Recurrence of Esophageal Adenocarcinomas*. 2024: bioRxiv.
133. Bowman, R.L., et al., *GlioVis data portal for visualization and analysis of brain tumor expression datasets.* Neuro Oncol, 2017. **19**(1): p. 139-141.
134. Bonner, W.M., et al., *GammaH2AX and cancer.* Nat Rev Cancer, 2008. **8**(12): p. 957-67.
135. Carruthers, R., et al., *Abrogation of radioresistance in glioblastoma stem-like cells by inhibition of ATM kinase.* Mol Oncol, 2015. **9**(1): p. 192-203.
136. Tufail, M., et al., *Hallmarks of cancer resistance.* iScience, 2024. **27**(6): p. 109979.
137. Li, Y., et al., *c-Met signaling induces a reprogramming network and supports the glioblastoma stem-like phenotype.* Proc Natl Acad Sci U S A, 2011. **108**(24): p. 9951-6.
138. Comoglio, P.M., L. Trusolino, and C. Boccaccio, *Known and novel roles of the MET oncogene in cancer: a coherent approach to targeted therapy.* Nat Rev Cancer, 2018. **18**(6): p. 341-358.
139. Behnan, J., G. Finocchiaro, and G. Hanna, *The landscape of the mesenchymal signature in brain tumours.* Brain, 2019. **142**(4): p. 847-866.
140. Hoogstrate, Y., et al., *Transcriptome analysis reveals tumor microenvironment changes in glioblastoma.* Cancer Cell, 2023.
141. Munoz, J.L., et al., *Temozolomide resistance in glioblastoma cells occurs partly through epidermal growth factor receptor-mediated induction of connexin 43.* Cell Death Dis, 2014. **5**(3): p. e1145.
142. Dhawan, A., et al., *EGFR Pathway Expression Persists in Recurrent Glioblastoma Independent of Amplification Status.* Cancers (Basel), 2023. **15**(3).
143. Sarosiek, K.A., et al., *Developmental Regulation of Mitochondrial Apoptosis by c-Myc Governs Age- and Tissue-Specific Sensitivity to Cancer Therapeutics.* Cancer Cell, 2017. **31**(1): p. 142-156.
144. Deng, J., et al., *Proapoptotic BH3-only BCL-2 family protein BIM connects death signaling from epidermal growth factor receptor inhibition to the mitochondrion.* Cancer Res, 2007. **67**(24): p. 11867-75.
145. Vera, M.B., et al., *Noxa and Mcl-1 expression influence the sensitivity to BH3-mimetics that target Bcl-xL in patient-derived glioma stem cells.* Sci Rep, 2022. **12**(1): p. 17729.
146. Nguyen, T.T., et al., *OGDH and Bcl-xL loss causes synthetic lethality in glioblastoma.* JCI Insight, 2024. **9**(8).
147. Houweling, M., et al., *Screening of predicted synergistic multi-target therapies in glioblastoma identifies new treatment strategies.* Neurooncol Adv, 2023. **5**(1): p. vdad073.

148. Lombardi, G., et al., *Regorafenib compared with lomustine in patients with relapsed glioblastoma (REGOMA): a multicentre, open-label, randomised, controlled, phase 2 trial.* Lancet Oncol, 2019. **20**(1): p. 110-119.
149. Li, Y., et al., *Models for evaluating glioblastoma invasion along white matter tracts.* Trends Biotechnol, 2024. **42**(3): p. 293-309.
150. Marques-Torrejon, M.A., E. Gangoso, and S.M. Pollard, *Modelling glioblastoma tumour-host cell interactions using adult brain organotypic slice co-culture.* Dis Model Mech, 2018. **11**(2).
151. Corless, B.C., et al., *Development of Novel Mutation-Specific Droplet Digital PCR Assays Detecting TERT Promoter Mutations in Tumor and Plasma Samples.* J Mol Diagn, 2019. **21**(2): p. 274-285.
152. Corti, G., et al., *A Genomic Analysis Workflow for Colorectal Cancer Precision Oncology.* Clin Colorectal Cancer, 2019. **18**(2): p. 91-101.e3.
153. Crisafulli, G., et al., *Whole exome sequencing analysis of urine trans-renal tumour DNA in metastatic colorectal cancer patients.* ESMO Open, 2019. **4**(6).
154. Crisafulli, G., et al., *Temozolomide Treatment Alters Mismatch Repair and Boosts Mutational Burden in Tumor and Blood of Colorectal Cancer Patients.* Cancer Discov, 2022. **12**(7): p. 1656-1675.
155. Shaw, R.J., et al., *Promoter methylation of P16, RARbeta, E-cadherin, cyclin A1 and cytoglobin in oral cancer: quantitative evaluation using pyrosequencing.* Br J Cancer, 2006. **94**(4): p. 561-8.
156. Hegi, M.E., et al., *MGMT gene silencing and benefit from temozolomide in glioblastoma.* N.Engl.J Med., 2005. **352**(10): p. 997-1003.
157. Dunn, J., et al., *Extent of MGMT promoter methylation correlates with outcome in glioblastomas given temozolomide and radiotherapy.* Br J Cancer, 2009. **101**(1): p. 124-31.
158. Prat, M., et al., *Agonistic monoclonal antibodies against the Met receptor dissect the biological responses to HGF.* J Cell Sci, 1998. **111 (Pt 2)**: p. 237-47.

PREVIOUS PUBLICATIONS

-De Bacco F., Orzan F., Casanova E., **Prelli M.**, Boccaccio C. *Protocol for in vitro establishment of heterogeneous stem-like cultures derived from whole human glioblastoma tumors*. STAR Protoc. 2023 Dec 15;4(4):102705. doi: 10.1016/j.xpro.2023.102705. Epub 2023 Nov 15. PMID: 37971942; PMCID: PMC10684815.

-De Bacco F., Orzan F., Crisafulli G., **Prelli M.**, Isella C., Casanova E., Albano R., Reato G., Erriquez J., D'Ambrosio A., Panero M., Dall'Aglio C., Casorzo L., Cominelli M., Pagani F., Melcarne A., Zeppa P., Altieri R., Morra I., Cassoni P., Garbossa D., Cassisa A., Bartolini A., Pellegatta S., Comoglio PM, Finocchiaro G., Poliani PL, Boccaccio C. *Coexisting cancer stem cells with heterogeneous gene amplifications, transcriptional profiles, and malignancy are isolated from single glioblastomas*. Cell Rep. 2023 Aug 29;42(8):112816. doi: 10.1016/j.celrep.2023.112816. Epub 2023 Jul 27. PMID: 37505981.

-Pergolizzi B., Panuzzo C., Ali MS, Lo Iacono M., Levra Levron C., Ponzone L., **Prelli M.**, Cilloni D., Calautti E., Bozzaro S., Bracco E. *Two conserved glycine residues in mammalian and Dictyostelium Rictor are required for mTORC2 activity and integrity.* J Cell Sci. 2019 Nov 14;132(22):jcs236505. doi: 10.1242/jcs.236505. PMID: 31653780.

ACKNOLEDGMENTS

It is said that a doctorate is a journey you take alone. I think that this is true, but also that it is not. This PhD has been a long journey in which I have been accompanied, some for a short time and some for the whole way, by many people to whom I am deeply grateful.

I would like to thank my supervisor and PI, Professor Carla Boccaccio, for guiding me through this PhD journey with her strong and valuable experience.

A special thanks to Francesca De Bacco, who has been my guide throughout this journey and has taught me not only how to achieve scientific success, but above all the importance of galactic errors. She knows.

Thanks to Francesca, Elena and Gigliola for sharing not only their knowledge but also their passion for what they do.

Thanks to Noemi and Salvo, my lab mates forever.

Thanks to my family, my parents and my sister Giulia, for always supporting me and putting up with my path, even if they didn't always understand it.

Thanks to Francesco for keeping me grounded.

Thanks to all the friends and colleagues who shared this journey with me.

And thank you for staying until the end.